

UNCLASSIFIED

AD NUMBER
AD913820
NEW LIMITATION CHANGE
TO Approved for public release, distribution unlimited
FROM Distribution authorized to U.S. Gov't. agencies only; Test and Evaluation; 11 SEP 1973. Other requests shall be referred to Advanced Ballistic Missile Defense Agency, Huntsville Office, Attn: RDMH-O, Huntsville, AL 35807.
AUTHORITY
ABMDA D/A ltr, 30 Jan 1974

THIS PAGE IS UNCLASSIFIED



aerodyne research, inc.

ARI-RN-20 V.1

AD 913820

**ROCKET PLUME RADIATION DUE TO INTERACTIONS
WITH THE ATMOSPHERE**

Volume I: Far Field Plume Radiance Model

**ABMDA Plume Interference Program
Final Technical Report**

by

**T.J. Rieger, H.R. Baum, C.E. Kolb
K.S. Tait, A.E. Germeles**

July 1973

Prepared for

CALSPAN Corporation

Subcontract No. S-72-14

(Prime Contract No. DAHC60-69-C-0035 Mod. No. P00011)

**Distribution limited to U.S. Gov't agencies only; Test and Evaluation:
11 Sept 73. Other requests for this document must be referred to
Advanced Ballistic Missile Defense Agency, Huntsville Office, RDMH-0.**

ROCKET PLUME RADIATION DUE TO INTERACTIONS
WITH THE ATMOSPHERE

Volume I

Far Field Plume Radiance Model

ABMDA Plume Interference Program

Final Technical Report

by

T.J. Rieger, H.R. Baum, C.E. Kolb
K.S. Tait, A.E. Germeles

AERODYNE RESEARCH, INC.
Burlington, Massachusetts 01803

July 1973

Prepared for the CALSPAN CORP.
Subcontract No. S-72-14
(Prime Contract No. DAHC60-69-C-0035 Mod. No. P00011)

ROCKET PLUME RADIATION DUE TO INTERACTIONS
WITH THE ATMOSPHERE

Volume I

Far Field Plume Radiance Model

Volume II

Interpretation of the POCO Data Taken During
Bus Deployment Maneuvers

Volume III

Plume Radiance Predictions for Athena H Second
and Third Stage Boosters

ABSTRACT

Calculations are presented that are elements of a model to predict the IR radiation emitted by high-altitude rocket plumes, because of the interaction of the plume gases with the ambient atmosphere. A model of plume radiance is presented, appropriate to high altitudes where the average time between plume and atmospheric species collisions is greater than the radiative lifetimes of the relevant excited molecular states. The three parts of the calculation – flow field density, molecular collisional excitation, and molecular nonequilibrium radiation – are identified and discussed.

The penetration of a hypersonic low-density atmosphere into the exhaust plume of a steadily firing rocket motor is studied by use of the kinetic theory of gases. The flow field is modeled mathematically by employing the Hill-Draper description of the exhaust jet and the BGK collision integral to reduce the problem to an analytically interpretable and computationally tractable form. The distribution function of the ambient gas is bimodal, with the unscattered fraction of the molecules peaked about the uniform freestream velocity, and the scattered gas carried along with the macroscopic exhaust gas velocity.

Classical rotational excitation probabilities for the collisions of HF, HCl, and OH with three atomic species have been calculated in three dimensions by use of a Monte Carlo procedure. Results are presented for the rotational excitation of both rigid diatomic rotors and those coupled via a classical harmonic oscillator. Hard-sphere intermolecular potentials are employed to obtain results applicable to high-energy (~ 1 eV) collisions. The results of these two methods of calculation indicate that for the center-of-mass collisional energy range of 1 to 10 eV, which dominates the problem of interest, activation of the vibrational modes is quite inefficient.

Once excited to high rotational states, these diatomic molecules can radiate at infrared wavelengths. The power radiated into a frequency band via pure rotational radiation by a diatomic molecule with a permanent electric dipole moment has been calculated both quantum mechanically and classically. The results define the region of validity for the classical approximation. It is concluded that for the range of parameters of interest to the plume interference problem the classical approximation is adequate. In order to be concrete, the results of the theory are applied to the particular case of rotational emission from the hydrogen fluoride molecule.

Volume I

TABLE OF CONTENTS

<u>Section</u>		<u>Page</u>
	ABSTRACT	iii
1	INTRODUCTION	I-1
2	PLUME RADIANCE FORMULATION	I-5
3	ATMOSPHERIC PENETRATION OF EXHAUST PLUMES UNDER RARIFIED FLOW CONDITIONS	I-11
	3.1 Introduction	I-11
	3.2 Mathematical Formulation	I-12
	3.3 The Hypersonic Limit	I-20
	3.4 The Asymptotic Solution	I-28
	3.5 The Numerical Computation Procedure	I-39
	3.6 Numerical Results	I-41
4	CLASSICAL CALCULATIONS OF ROTATIONAL AND VIBRATIONAL EXCITATION IN ENERGETIC ATOM-DIATOMIC HYDRIDE COLLISIONS	I-55
	4.1 Introduction	I-55
	4.2 Interaction Potentials	I-56
	4.3 Collision Mechanics	I-57
	4.4 Kinematics and Probability Model	I-65
	4.5 Calculation of Rotational and Vibrational Energy Distributions	I-66
	4.6 An Approximate Distribution for the Vibrational Model	I-80
	4.7 Differential Energy Transfer Cross Sections	I-86
	4.8 Discussion	I-87
5	PURE ROTATIONAL EMISSION FROM DIATOMIC MOLECULES IN THE QUANTUM AND CLASSICAL LIMITS	I-93
	5.1 Introduction	I-93
	5.2 Quantum Mechanical Formulation	I-94
	5.3 Classical Formulation	I-99
	5.4 Results	I-103
	REFERENCES	I-111

Volume I

LIST OF ILLUSTRATIONS

<u>Figure</u>	<u>Page</u>
3.1 Coordinate System Geometry. Nozzle Exit at Origin	I-15
3.2 Characteristic Ray Geometry	I-17
3.3 Schematic of Nonlocal Interaction	I-29
3.4 Ambient Penetration of Exhaust Plume	I-43
3.5 Radial Density Distribution for Aligned Plume	I-44
3.6 Radial Density Distribution for Aligned Plume	I-45
3.7 Angular Density Distribution for Aligned Plume	I-50
3.8 Angular Density Distribution for Non-Aligned Plume Windward Side . .	I-51
3.9 Angular Density Distribution for Non-Aligned Plume Leeward Side . . .	I-52
4.1 Coordinate Systems Used to Describe Collision	I-58
4.2 - Normalized probability distributions for the inelastic excitation 4.10 of the diatomic hydrides OH, HF, and HCl in collisions with He, O, and Ar. Solid histogram represents E_V^V/E_{CM} , and dashed- dotted histogram, E_R^V/E_{CM} , for the harmonic oscillator-atom collisions. Dashed histogram represents E_R^I/E_{CM} for rigid- rotor-atom collisions. Specific sets of collision partners are indicated for each figure	I-69
4.11 Definition of the angles θ'_K and θ'_T	I-81
4.12 Regions of integration in the y_1, y_2 plane	I-83
4.13 Comparison between approximate and empirical distributions for O + HF within the vibrational model. Dashed histogram repre- sents E_V^V/E_{CM} , and dotted histogram, E_V^I/E_{CM} , and smooth curves represent approximate solutions for these distributions	I-85
5.1 Radiated power as a function of time for the molecule HF with initial rotational quantum number $\ell_O = 10$, and for a band pass including contributions from the 6th through the 4th level	I-104
5.2 Radiated power as a function of time for the molecule HF with initial rotational quantum number $\ell_O = 15$, and for a band pass including con- tributions from the 10th through the 5th level	I-105
5.3 Radiated power as a function of time for the molecule HF with initial rotational quantum number $\ell_O = 30$, and for a band pass including con- tributions from the 25th through the 10th level	I-106
5.4 Radiated power as a function of time for the molecule HF with initial rotational quantum number $\ell_O = 20$, and for a band pass including con- tributions from the 20th through the 10th level	I-107

FAR FIELD PLUME RADIANCE MODEL

1. INTRODUCTION

Plume interference can be roughly defined as the degradation of the signal-to-noise ratio of a sensor due to the radiation emitted by the exhaust plume of a rocket engine either aboard the same vehicle as the sensor or aboard some other, nearby vehicle. If the engine is aboard the same vehicle as the sensor, the situation is one of self-interference; if it is aboard a nearby vehicle, it is one of mutual interference. The emphasis of the work reported here is on self-interference, although much, if not all, of it is applicable to mutual interference as well.

In the summer of 1971, a panel with Dr. Hans Wolfhard of IDA as chairman performed a preliminary study of the plume interference problem.⁽¹⁾ In particular, this panel divided plume interference into two basic parts: the near-field radiation and the far-field radiation. The near-field was defined as the radiation originating from IR-active molecular species emerging from the rocket nozzle in an excited state. The far-field was defined as the radiation from plume species excited into IR-active states because of collisions with atmospheric species. Thus, the division of the problem is based on the molecular excitation mechanism.

On the basis of their initial examination of the plume interference problem, the Wolfhard panel recommended that it be studied in more detail. The first efforts to study the problem undertaken by ABMDA were directed towards the specific case of the proposed HIT interceptor system.^(2,3)

This report deals with the far-field plume interference problem, and is the Final Technical Report of the far-field modeling efforts performed at Aerodyne Research, Inc. during the ABMDA Plume Interference Program. The work done is a natural extension of far-field plume radiance calculations made earlier under the HIT Plume Interference Program.⁽⁴⁾

The calculations performed to predict the far-field plume radiance of the HIT vehicle were for a small, short-pulsed solid propellant engine fired in the upper atmosphere, typically above 200 km. The molecular radiating mode identified as the dominant source of radiation in the far field was pure rotation of water. The details of the various calculations are discussed in the HIT Program Final Technical Report,⁽⁴⁾ as well as in separate publications.^(5,6,7)

These HIT program calculations were performed over a relatively short period of time in order to calculate the signal-to-noise ratio degradation as a function of time after engine shutdown, and the results of the calculations were used as system design limits and criteria. The work reported below, and performed under the Plume Interference Program, was done under different circumstances, however. The aim of the far-field modeling under this later program was to broaden the predictive capability of the initial modeling efforts by considering different aerodynamic regimes, and by including IR-active molecular modes other than the water rotation considered for HIT. To achieve this end a number of calculations were undertaken. (In addition, data analyses and plume radiance predictions were carried into execution, and are reported under separate cover in Volumes II and III).

Section 3 of this report discusses a calculation of the penetration of a hypersonic low-density atmosphere into the exhaust plume of a steadily firing rocket motor using the kinetic theory of gases. Section 4 concerns the far-field molecular excitation process; classical rotational excitation probabilities for collisions of HF, HCl, and OH with three atomic species have been calculated in three dimensions. Section 5 concerns the nonequilibrium radiation from the excited molecular states; the power radiated into a frequency band via pure rotational radiation by a diatomic molecule with a permanent electric dipole moment has been calculated both quantum mechanically and classically. The calculations presented in these three sections, along with the overall plume radiance formulation discussed in Section 2, are the far-field plume radiance model elements performed during this program.

Before proceeding to the details, it is perhaps worthwhile to outline the present status and extent of the far-field models. Thus far, there are basically two aerodynamic interaction configurations which can be modeled. The first configuration is the decay

The calculations performed to predict the far-field plume radiance of the HIT vehicle were for a small, short-pulsed solid propellant engine fired in the upper atmosphere, typically above 200 km. The molecular radiating mode identified as the dominant source of radiation in the far field was pure rotation of water. The details of the various calculations are discussed in the HIT Program Final Technical Report,⁽⁴⁾ as well as in separate publications.^(5, 6, 7)

These HIT program calculations were performed over a relatively short period of time in order to calculate the signal-to-noise ratio degradation as a function of time after engine shutdown, and the results of the calculations were used as system design limits and criteria. The work reported below, and performed under the Plume Interference Program, was done under different circumstances, however. The aim of the far-field modeling under this later program was to broaden the predictive capability of the initial modeling efforts by considering different aerodynamic regimes, and by including IR-active molecular modes other than the water rotation considered for HIT. To achieve this end a number of calculations were undertaken. (In addition, data analyses and plume radiance predictions were carried into execution, and are reported under separate cover in Volumes II and III).

Section 3 of this report discusses a calculation of the penetration of a hypersonic low-density atmosphere into the exhaust plume of a steadily firing rocket motor using the kinetic theory of gases. Section 4 concerns the far-field molecular excitation process; classical rotational excitation probabilities for collisions of HF, HCl, and OH with three atomic species have been calculated in three dimensions. Section 5 concerns the nonequilibrium radiation from the excited molecular states; the power radiated into a frequency band via pure rotational radiation by a diatomic molecule with a permanent electric dipole moment has been calculated both quantum mechanically and classically. The calculations presented in these three sections, along with the overall plume radiance formulation discussed in Section 2, are the far-field plume radiance model elements performed during this program.

Before proceeding to the details, it is perhaps worthwhile to outline the present status and extent of the far-field models. Thus far, there are basically two aerodynamic interaction configurations which can be modeled. The first configuration is the decay

of short-pulsed engine plumes operating at high altitudes. The engines aboard the proposed HIT vehicle are of such a type. The second is the interaction region between the relatively dense core of a continuously firing engine and the high-altitude atmosphere. In each case, the engine size appropriate to the model has up to several thousand pounds thrust at altitudes of 400 to 500 km.

In each of these two aerodynamic regimes, a number of IR-active plume species have been included in the overall radiation model. The high collision-energy excitation of, and the subsequent nonequilibrium radiation from the pure rotational motion of H_2O and the diatomic hydride molecules HF, HCl and OH have so far been considered. Concentration has been centered on these pure rotational emitters, since rotational radiation forms a quasicontinuous spectral background across the wavelength regions of interest in the plume interference problem, and thus, cannot be eliminated by judicious wavelength filtering.

While considering the scope of the present far-field plume radiance models, it is worth noting that all the calculations mentioned have begun from basic principles. There is very little, if any, data presently available shedding light on the far-field problem. Thus, the modeler bears a heavy burden, and it behooves him to base his models as firmly as possible on accepted physical principles.

Best Available Copy

2. PLUME RADIANCE FORMULATION

The overall objective of the far-field modeling efforts is to be able to calculate plume radiance for a variety of interceptor configurations. In order to handle this objective, the overall radiance problem has been broken down into several parts, as was mentioned in the introduction. This section will more clearly define this division into parts, and, in particular, will describe the overall radiance formulation necessary to combine these parts.

Generally speaking, the sequence of events leading to far-field radiation from a rocket exhaust plume is as follows. The rocket engine burns for some time, Δt , and an expanding mass of gas is emitted from the nozzle. As this gas flows away from the nozzle, the plume molecular species begin to collide with atmospheric species. During these collisions, plume species are excited into IR active states, and they consequently begin to radiate. As they continue to travel away from the rocket nozzle, the plume species continue to undergo collisions that can excite them (or possibly deexcite them if they have not had time to radiate away the excitation energy imparted in a previous collision). In addition, these collisions bring the plume molecules into equilibrium with the ambient atmosphere, so that, asymptotically, in time, the plume becomes a cloud of gas at rest with respect to the atmosphere and diffuses away. Therefore, the three individual parts of the far-field radiance problem are the calculations of the plume and atmosphere gas densities, the excitation rate of relevant modes of plume species, and the power radiated by these excited modes. The plume radiance model, then combines these separate calculations to calculate plume radiance.

The overall radiance model to be used here is similar to the one evolved earlier for the specific case of the HIT intercept vehicle.⁽⁸⁾ The following discussion parallels the discussion of that model, to be found in Ref. (8).

The plume is an extended source of radiation. The power on the detector from such an extended source is given simply by

$$= \Omega_f A_R N \quad (2-1)$$

where Ω_f is the solid angular field of view of the detector, A_R is the area of the receiver optics, and N is the plume radiance (emitted into the operating band of the detector; units: watts/cm²-sr). The source radiance can be written

$$N = \frac{1}{4\pi} \int_0^\infty dr \int dS_i I(S_i) n(S_i; \vec{r}, t) \quad (2-2)$$

where $I(S_i)$ is the power radiated into the band by a water molecule in the S_i th state, $n(S_i; \vec{r}, t)$ is the density of such molecules at point \vec{r} in space and at time t , the line integral dr is along the sensor line of sight, and the integral dS_i is over the manifold of accessible molecular states S_i . Although correct, this equation is not very useful as written. For the conditions under which many interceptor systems operate, considerable simplification is possible.

First, at high altitudes (e.g., above 200 km) the atmosphere is sufficiently tenuous that the average time between collisions of plume and atmospheric species becomes longer than the radiative lifetimes of the relevant LWIR active excited states, and most excited molecules completely deexcite via radiative emission between collisions. This limit of short radiative lifetimes compared to mean collision times is the exact opposite limit of the more usually encountered one of thermal equilibrium.

Second, for a narrow field-of-view detector, the plume and atmospheric gases may be considered uniform across the field of view. This means that the power radiated by an ensemble of molecules in some elemental volume is given by

$$dP = EN(E^*; \omega_1, \omega_2) \dot{n}(E^*; \vec{r}, t) \quad (2-3)$$

where \dot{n} is the creation rate of molecules in an excited state E^* , and EN is the total energy ultimately radiated by the state E^* into the frequency band of interest, ω_1 to ω_2 .

Thus, to find the plume radiance under these conditions, one need only add up the contributions of all the excited states and integrate along the observational line of sight. For the case of rotational excitation and radiation, of primary interest here as explained in the introduction, the plume radiance, N , can be written as

$$N = \frac{1}{4\pi} \int_0^\infty dr \int_0^\infty dE_R EN(E_R; \omega_1, \omega_2) \dot{n}(E_R; \vec{r}, t) \quad (2-4)$$

where $EN(E_R; \omega_1, \omega_2)$ is the total $\omega_1 \rightarrow \omega_2$ band energy emitted by a molecule in the initial rotational energy state E_R , \dot{n} is the rate of creation of such molecules at point \vec{r} and at time t per unit energy, the integral dr is still a line integral along the line of sight, and the dE_R integral is over all initial rotational energies of the molecule.

$\dot{n}(E_R; \vec{r}, t)$, the rate of creation of molecules in the state E_R per unit volume per unit energy (E_R), is related to the differential excitation cross section, the collision relative velocity, and the exhaust and ambient gas densities. That is, \dot{n} is the number of collisions between exhaust molecules and ambient atmospheric particles per unit energy per unit time producing the appropriate final rotational state, and is given by

$$\dot{n}(E_R; \vec{r}, t) = \int d^3v_a \int d^3v_e \left[|\vec{v}_a - \vec{v}_e| \frac{\partial \sigma}{\partial E_R} f_a(\vec{v}_a) f_e(\vec{v}_e) \right] \quad (2-5)$$

where \vec{v}_a is the ambient particle velocity, \vec{v}_e is the plume molecule velocity, $\partial \sigma / \partial E_R$ is the differential rotational excitation cross section, $f_a(\vec{v}_a)$ is the ambient atmospheric-phase space distribution function (units: $\text{cm}^{-3}(\text{cm/sec})^{-3}$), and $f_e(\vec{v}_e)$ is the exhaust-phase space distribution function for the appropriate plume constituent. This expression is the usual collisional rate constant expression for an ambipolar process. For the moment, the two distribution functions will remain unspecified to maintain complete generality, but it is worthwhile to note

that in virtually every conceivable case of interest, the phase space distribution function is separable into a spatial distribution function (i.e., number density) and a velocity distribution function. For example, for a uniform ambient atmosphere in thermal equilibrium at temperature T_∞ , $f_a(\vec{v}_a)$ would simply become

$$f_a(\vec{v}_a) = n_\infty \left(\frac{m_a}{2\pi kT_\infty} \right)^{3/2} \exp \left(- \frac{m_a v_a^2}{2 kT_\infty} \right) \quad (2-6)$$

where n_∞ is a constant number density (in the context of Eq. (2-6)), and the rest of the expression is the usual Maxwellian velocity distribution.

Combining the expression for \dot{n} , Eq. (2-5), with the expression for the plume radiance N , Eq. (2-4), yields the following:

$$N = -\frac{1}{4\pi} \int_{\text{LOS}} dr \int_0^\infty dE_R \int d^3v_a \int d^3v_e EN(E_R; \omega_1, \omega_2) \\ \times \left| \vec{v}_a - \vec{v}_e \right| \frac{\partial \sigma}{\partial E_R} f_a(\vec{v}_a) f_e(\vec{v}_e) \quad (2-7)$$

If the two distributions are separable into two distinct pieces,

$$f_a(\vec{v}_a) = n_a g_a(\vec{v}_a) \\ f_e(\vec{v}_e) = n_e g_e(\vec{v}_e) \quad , \quad (2-8)$$

then

$$N = \int_{\text{LOS}} dr \frac{n_a n_e}{4\pi} \int_0^\infty dE_R \int d^3v_a \int d^3v_e \quad (2-9)$$

$$\times \left[\left| \vec{v}_a - \vec{v}_e \right| \frac{\partial \sigma}{\partial E_R} g_e(\vec{v}_e) g_a(\vec{v}_a) \right]$$

where $g(\vec{v})$ is a velocity distribution function (units: (velocity)⁻³), n_e is the number density of the relevant plume species, n_a is the ambient number density, and n_e and n_a (expressed as $n_{e,a}(r, t)$) are both functions of time and position.

This expression for the plume radiance, N , along with the detailed calculations of $EN(E_R; \omega_1, \omega_2)$, $\partial \sigma / \partial E_R$, n_e and n_a , form the basis of the present far-field plume background interference analysis. The results of the separate calculations of n_a , n_e , $\partial \sigma / \partial E_R$, and EN can be used in an expression like Eq. (2-7) to calculate a plume radiance for a sensor line of sight. This formulation of the plume radiance problem is appropriate for calculating the power falling on some given detector. If more detailed information is desired, plume radiance contours and a somewhat different formulation are required. In the present context, however, it should be emphasized that the individual calculations to be described in the following sections of this report are independent of the details of the exact radiance formulation, and can be used in more detailed plume radiance calculations, or in radiance formulations that relax the short radiative lifetime or spatially homogeneous assumptions discussed above.

3. ATMOSPHERIC PENETRATION OF EXHAUST PLUMES UNDER RARIFIED FLOW CONDITIONS

3.1 Introduction

The flow pattern set up by the interaction of an exhaust plume generated by the continuous firing of a rocket motor and a tenuous atmosphere has been intensively studied in recent years. Most of this work has focused on those domains of motor thrust and operating altitude permitting this interaction to be described on the basis of continuum fluid mechanics. At altitudes sufficiently high for the ambient mean free path to become larger than the continuum interaction length scale, the analysis of such a flow must be based on the kinetic theory of gases. Under these conditions, the length scale associated with the atmospheric penetration of the exhaust plume is \sqrt{A}/Kn , where A is the nozzle exit area, and Kn is the Knudsen number based on \sqrt{A} and the mean free path, based on average exit conditions (Muntz, Hamel, and Maguire 1970)⁽⁹⁾ This scale is, typically, much larger than the dimensions of the vehicle carrying the motor, since $Kn \ll 1$. The presence of the vehicle itself may thus be ignored in analyzing phenomena on this scale.

When the penetration scale is small compared with the ambient mean free path, the response of the atmosphere to the presence of the plume is decoupled from the process by which the atmosphere modifies the vacuum plume expansion. This situation is appropriate to moderate-sized engines, such as those employed for attitude control or maneuvering purposes in the upper atmosphere. The spatial separation of these two phenomena has been exploited by Brook and Hamel (1972)⁽¹⁰⁾ in their study of a spherical source interacting with a stationary background gas. Baum (1973)⁽¹¹⁾ considered the expansion of a transient exhaust plume into a rarefied atmosphere by invoking equivalent assumptions about the scales associated with the interactions occurring in that problem.

The present work is concerned with the penetration of a hypersonic ambient stream into a steady-state exhaust plume under the conditions stated above. The exhaust gas properties are computed from a simple model proposed by Hill and Draper (1966)⁽¹²⁾ of the continuum expansion of a jet into a vacuum. This expanding jet serves as a diffuse scatterer of ambient molecules. The scattering is represented mathematically by the Krook collision integral. This formulation leads to an analytically interpretable and computationally tractable integral equation for the ambient density distribution. The molecular distribution function is described analytically in terms of the density. The distribution function is bimodal, with the unscattered molecules peaked about the uniform free-stream velocity, and the scattered gas convected with the local macroscopic exhaust velocity. An asymptotic, analytical solution to the integral equation is obtained. This result is used, in conjunction with direct numerical solutions, to obtain illustrative flow patterns for both axially symmetric and nonsymmetric configurations.

3.2 Mathematical Formulation

The formulation of the model will now be considered in detail. The penetration scale is assumed to be sufficiently small compared with the ambient mean free path for collisions between ambient molecules to be ignored. The kinetic equation for the ambient, molecular distribution function $f(\vec{x}, \vec{v})$ is a modified version of that given by Gross and Krook (1956).

$$\begin{aligned} \vec{v} \cdot \frac{\partial f}{\partial \vec{x}} &= \omega (n\Phi - f) \\ \omega &= n_e \sigma \left| \vec{u}_\infty - \frac{\vec{u}}{M} \right| \\ \Phi &= \left(\frac{m}{2\pi kT_e} \right)^{3/2} \exp \left\{ - \frac{m}{2kT_e} (\vec{v} - \vec{u}_e)^2 \right\} \\ n(\vec{x}) &= \int f d^3v \end{aligned} \tag{3-1}$$

Here $n(\vec{x})$ is the ambient number density, and n_e , \vec{u}_e , T_e are, respectively, the exhaust gas number density, macroscopic velocity, and temperature. The maximum velocity of the exhaust gas is \vec{u}_M , while the cross section σ , entering the expression for the collision frequency ω , is an effective momentum transfer cross section. The relation between the momentum transfer between species computed from Eq. (3-1), and that given by Gross and Krook (1956),⁽¹³⁾ is explained in Baum (1973).⁽¹¹⁾ The mean relative speed is taken to be that between \vec{u}_M and the ambient wind \vec{u}_∞ , because the exhaust and ambient speed ratios, W_e and W_∞ , are large under the conditions of interest.

The exhaust properties are assumed in a modified version of the form devised by Hill and Draper (1966).⁽¹²⁾ The adopted forms are equivalent to the Hill-Draper model far from the engine, but take on the prescribed nozzle exit values at $\vec{x} = 0$. The relevant equations are:

$$\frac{n_e}{n_o} = \frac{BA_{\text{exit}} \exp \left\{ -\Lambda_\infty^2 (1-\cos\theta)^2 \right\}}{r^2 + BA_{\text{exit}} \exp \left\{ -\Lambda_\infty^2 (1-\cos\theta)^2 \right\}}$$

$$\frac{T_e}{T_o} = \left(\frac{n_e}{n_o} \right)^{\gamma-1} \quad \vec{u}_e = u_e \hat{r} \quad (3-2)$$

$$\frac{u_e^2}{2} + \frac{\gamma}{\gamma-1} \frac{kT_e}{m_e} = \frac{u_M^2}{2} = \frac{u_o^2}{2} \left[1 + \frac{2}{\gamma-1} \frac{1}{M_o^2} \right]$$

The parameters B and Λ_∞ are given in terms of exit properties by

$$B = \frac{\Lambda_\infty}{(\pi)^{3/2}} \frac{u_o}{u_M}$$

$$\Lambda_\infty = \frac{1}{\sqrt{\pi}} \left\{ 1 - \frac{u_o}{u_M} \left(1 + \frac{1}{\gamma M_o^2} \right) \right\}^{-1} \quad (3-3)$$

The nozzle exit number density n_0 , speed u_0 , temperature T_0 , Mach number M_0 , and the ratio of specific heats γ are determined by the engine parameters. The exhaust properties are expressed in a spherical, polar coordinate system, centered about the unit thrust vector \hat{t} . The polar angle is θ , and the azimuthal angle ϕ is measured from the plane containing the wind and thrust vectors. The wind vector makes an angle ψ with the thrust vector. Thus (see Fig. 3-1)

$$\vec{r} = r (\hat{t} \cos\theta + \hat{j} \sin\theta \cos\phi + \hat{k} \sin\theta \sin\phi) \equiv \hat{r} r$$

$$\vec{u}_\infty = u_\infty (\hat{t} \cos\psi + \hat{j} \sin\psi)$$

$$\vec{v} \equiv V \hat{v} = V (\cos\xi \hat{t} + \sin\xi \cos\eta \hat{j} + \sin\xi \sin\eta \hat{k})$$

All quantities with a caret superscript are unit vectors. The system of Eqs. (3-1) through (3-3) must be supplemented by the boundary condition that, far from the plume, the flow is uniform.

$$\lim_{r \rightarrow \infty} f(\vec{r}, \vec{v}) = n_\infty \left(\frac{m}{2\pi k T_\infty} \right)^{3/2} \exp \left\{ \frac{-m}{2k T_\infty} (\vec{v} - \vec{u}_\infty)^2 \right\} \equiv f_\infty \quad (3-4)$$

$$W_\infty = \frac{u_\infty}{\sqrt{k T_\infty / m}}$$

Here n_∞ , \vec{u}_∞ , and T_∞ are, respectively, the ambient number density, velocity, and temperature far from the plume.

The representation of the exhaust gas displayed in Eq. (3-2) and (3-3) describes the expansion into vacuum of a continuum jet plume. The motion is isentropic and is energetic. The density distribution (and, hence, each displayed fluid quantity) satisfies the inviscid equations of motion asymptotically, far from the nozzle exit. The angular dependence of the asymptotic density distribution is chosen as an empirical curve fit to numerical methods of characteristic solutions for a variety of engines. The expressions for the parameters B and Λ_∞ ensure global conservation of mass, momentum, and energy.

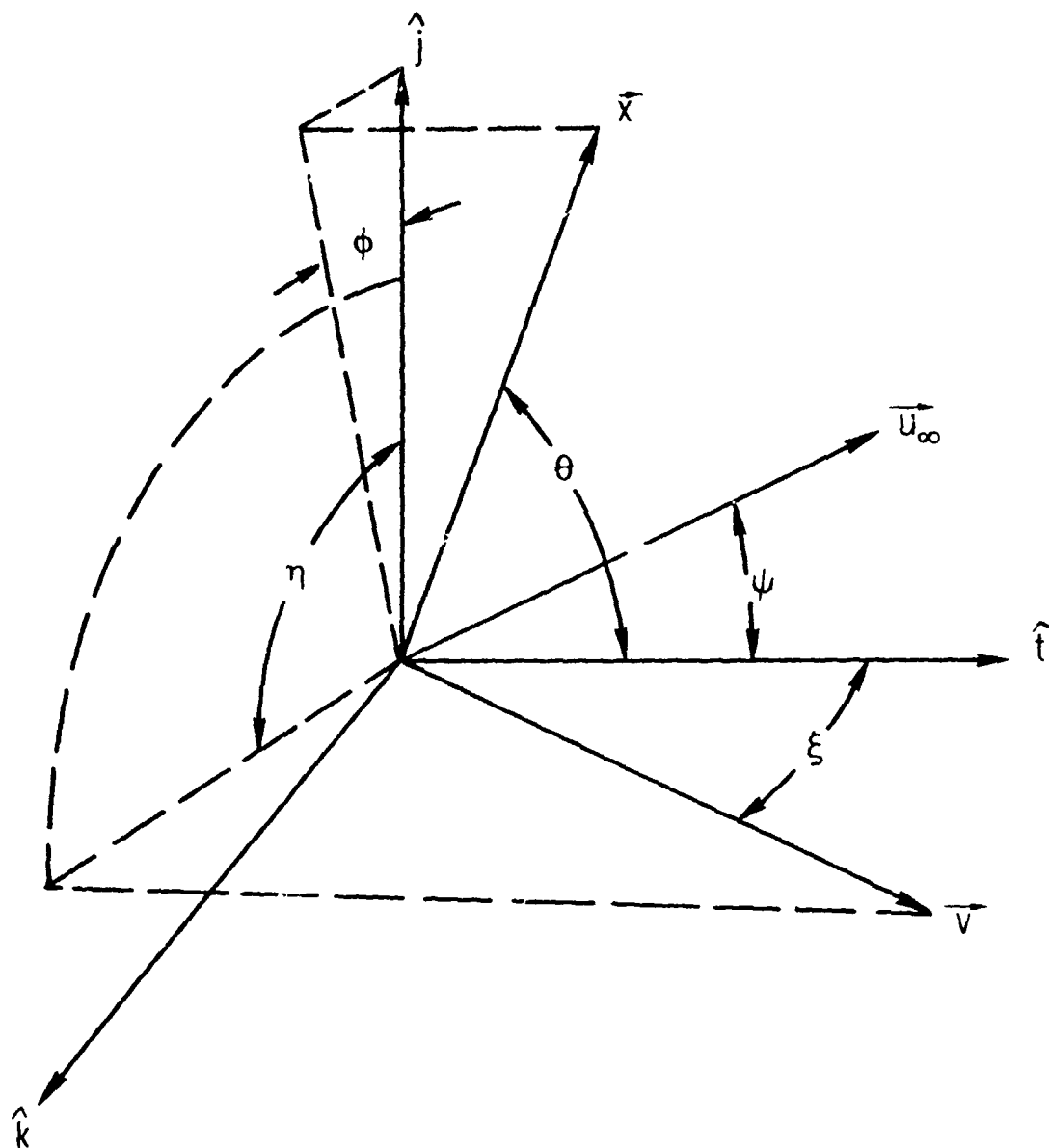


Figure 3.1 - Coordinate System Geometry. Nozzle Exit at Origin.

The continuum description of the exhaust gas ultimately breaks down as the plume expands. The rarefaction process has been studied by Grundy (1969),⁽¹⁴⁾ who shows that, except at large angles θ , with respect to the thrust axis, the density and velocity are given by the continuum solution. The radial component of the pressure tensor, on the other hand, does not continue to decrease isentropically, but levels off at a finite, "frozen" asymptote. The Mach number corresponding to the freezing temperature is typically very large, on the order of 10-20 for most angles θ . Under these circumstances, the interaction between ambient and exhaust gases is nearly independent of the local plume temperature, as shown by the asymptotic solution attained in Section 3.4.

The next step in the calculation is the construction of the fundamental integral equation for $n(\vec{x})$. Following Anderson (1965),⁽¹⁵⁾ Eq. (3-1) may be written in characteristic form as

$$V \frac{d}{ds} f(\vec{x} + \hat{v}s) = (\vec{x} + \hat{v}s) \cdot \nabla \left\{ \phi(\vec{x} + \hat{v}s) - f \right\} \quad (3-5)$$

$$\vec{r} = \vec{x} + \hat{v}s$$

This describes the evolution of f , at any point \vec{r} , a distance s along a ray through the field point \vec{x} , in the direction \hat{v} (Fig. 3-2). Now integrate Eq. (3-5) from minus infinity to the field point $s=0$, applying the boundary condition represented by Eq. (3-4). The result is

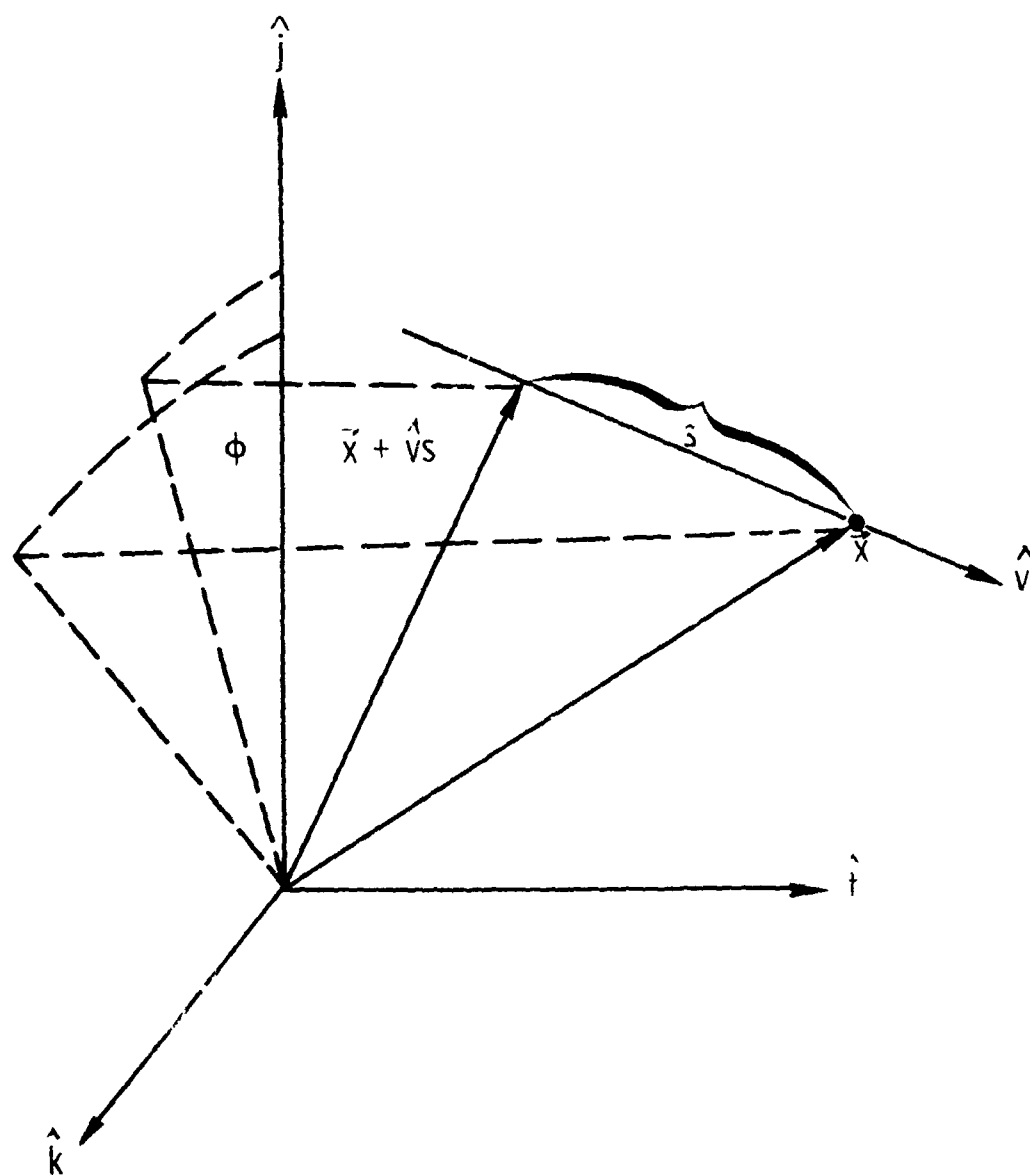


Figure 3.2 - Characteristic Ray Geometry. (Molecules at \vec{x} Arrive From all Directions \hat{v} . The Probability of Arrival Depends Upon the Distance s From the Point of Last Collision.)

$$f = f_{\infty} e^{-\tau/V} + \frac{1}{V} \int_{-\infty}^0 ds' \omega(\vec{x} + \hat{v}s') \phi(\vec{x} + \hat{v}s') e^{-\tau^*/V} n(\vec{x} + \hat{v}s')$$

$$\tau = \int_{-\infty}^0 \omega(\vec{x} + \hat{v}s) ds \quad (3-6)$$

$$\tau^* = \int_{s'}^0 \omega(\vec{x} + \hat{v}s) ds$$

$$\phi(\vec{x} + \hat{v}s') = n_e \left(\frac{m}{2kT_e} \right)^{3/2} \exp \left\{ - \frac{m}{2kT_e} \left[v - u_e \cos \alpha \right]^2 - \frac{1}{2} w_e^2 \left[1 - \cos^2 \alpha \right] \right\}$$

$$\cos \alpha \equiv \hat{v} \cdot \hat{r} = \frac{[\cos \xi \cos \theta + \sin \xi \sin \theta \cos (\eta - \phi)] r + s'}{\left\{ r^2 + (s')^2 + 2rs' [\cos \theta \cos \xi + \sin \theta \sin \xi \cos (\eta - \phi)] \right\}^{1/2}}$$

The argument of n_e , u_e , and T_e in Eq. (3-6) is $\vec{x} + \hat{v}s'$. Note that the V dependence is now displayed explicitly, since \hat{v} depends only on the angle variables ξ and η . The integral equation follows from Eq. (3-6), by using the definition of n in terms of the distribution function f .

$$n = \int_0^\pi \sin \xi d\xi \int_0^{2\pi} d\eta \int_0^\infty v^2 dv f$$

Thus

$$\begin{aligned} \frac{n}{n_\infty} = & \frac{1}{2\pi} \int_0^\pi \sin \xi d\xi \int_0^{2\pi} d\eta \left\{ H_4 \left(W_\infty \cos \beta; \tau \sqrt{\frac{m}{kT_e}} \right) \exp \left[-\frac{1}{2} W_\infty^2 (1 - \cos^2 \beta) \right] \right. \\ & \left. + \int_{-\infty}^0 ds' \omega \sqrt{\frac{m}{kT_e}} H_3 \left(W_e \cos \alpha; \tau^* \sqrt{\frac{m}{kT_e}} \right) \exp \left[-\frac{1}{2} W_e^2 (1 - \cos^2 \alpha) \right] \frac{n}{n_\infty} (\vec{x} + \hat{v}s') \right\} \end{aligned} \quad (3-7)$$

$$\cos \beta = \cos \xi \cos \psi + \sin \xi \sin \psi \cos \eta$$

Again, all exhaust properties in Eq. (3-7) are functions of $\vec{x} + \hat{v}s'$. The functions $H_n(p, q)$ are defined by:

$$H_n(p, q) = \frac{1}{\sqrt{2\pi}} \int_0^\infty dV V^{n-2} \exp \left\{ -\frac{1}{2} (V-p)^2 - q/V \right\}$$

Anderson and Macomber (1964)⁽¹⁶⁾ contains a detailed analysis of this function, together with tables for $n = 1, 2, 3$. Eq. (3-7) determines the spatial density distribution of the atmosphere as it penetrates the plume core, while Eq. (3-6) expresses the distribution function in terms of n . In this form, the equations are too complicated to be useful. However, by utilizing the fact that, in many cases of interest, both W_e and W_∞ are large, Eqs. (3-6) and (3-7) can be reduced to a tractable form.

3.3 The Hypersonic Limit

Consider the first term in the integral Eq. (3-7). For large W_∞ , the exponential factor suggests that the integrand, considered as a function of ξ , is strongly peaked about $\cos\beta^2 = 1$. Examination of the H_n functions reveals that H_n , considered as a function of p , is exponentially small for large negative p and proportional to p^{n-2} for large positive p . Since the dependence of H_n on W_∞ for large positive p is weak, part from a purely multiplicative factor W_∞^{n-2} , the dominant contribution to the ξ integration should come from the neighborhood of $\cos\beta = +1$.

To proceed formally from these ideas it is more convenient to do the ξ integral first, and employ the variable $x = \cos\xi$. The integral under consideration assumes the form:

$$I = \int_{-1}^1 dx H_4(x) \exp \left\{ -\frac{1}{2} W_\infty^2 g(x) \right\}$$

$$g(x) = 1 - \left\{ x \cos\psi + \sqrt{1-x^2} \sin\psi \cos\eta \right\}^2 \quad (3-8)$$

Applying the method of steepest descent to (3-8), the saddle point is at:

$$X_0 = \pm \frac{\cos\psi}{\sqrt{1 - \sin^2\psi \sin^2\eta}}$$

$$\cos\beta(X_0) = \pm \sqrt{1 - \sin^2\psi \sin^2\eta}$$

Both saddle points are real, but the contribution from the one associated with the minus sign is exponentially smaller than that associated with the positive value of $\cos\sigma$, and is henceforth ignored. The integral I is now readily evaluated as:

$$I \cong \frac{2}{W_\infty} \sqrt{\frac{\pi}{g''(X_0)}} e^{-\frac{1}{2} W_\infty^2 g(X_0)} H_4 \left(W_\infty \cos \beta; \tau(X_0) \frac{m}{kT_\infty} \right)$$

$$g(X_0) = \sin^2 \psi \sin^2 \eta$$

$$g''(X_0) = \frac{2}{1-X_0^2} (1 - \sin^2 \eta \sin^2 \psi)$$

$$X_0 = \frac{\cos \psi}{\cos \beta} \quad \cos \beta = \sqrt{1 - \sin^2 \psi \sin^2 \eta} \quad (3-9)$$

Using the result (3-9), the integration over η may be readily performed. The required integral is then:

$$J = \frac{1}{2\pi} \int_0^{2\pi} I d\eta$$

Examination of this expression when $W_\infty \sin \psi \gg 1$ (i.e., the undisturbed flow is neither parallel nor anti-parallel to the thrust vector) shows that the dominant contribution comes from the saddle point at $\eta = 0$. The apparent saddle point at $\eta = \pi$ is spurious, with the result that:

$$J = \frac{1}{W_\infty^2} H_4 \left(W_\infty, \sqrt{\frac{m}{kT_\infty}} \tau \right)$$

$$\tau \equiv \tau(\xi = \psi; \eta = 0) \quad (3-10)$$

A separate calculation when $W_\infty \sin\psi$ is $O(1)$ (but $W_\infty > 1$) yields the same result for J . Physically, Eq. (3-10) states that the overwhelming majority of the unscattered ambient molecules are aligned with the uniform wind upstream of the plume. A similar analysis (the details of which are presented in Appendix A) may be applied to the homogeneous term in Eq. (3-7). The hypersonic limit of Eq. (3-7) then becomes:

$$\begin{aligned} \frac{n}{n_\infty}(y) &= \frac{1}{W_\infty} H_4(W_\infty, q_\infty) + \int_0^y dy' K(y', y) \frac{n}{n_\infty}(y') \\ K(y, y') &= \left[1 + \left(\frac{u_M}{u_\infty} \right)^2 - \frac{2u_M}{u_\infty} \cos\epsilon \right]^{1/2} \left(\frac{y'}{y} \right)^2 \frac{u_\infty}{u_e}(y') \frac{n_e}{n_0}(y') \\ &\quad \cdot \frac{1}{W_e} H_3(W_e, q_e) \end{aligned} \quad (3-11)$$

$$W_e = W_e(y'), \quad q_e = q_e(y')$$

$$\cos\epsilon = \cos\theta\cos\psi + \sin\theta\sin\psi\cos\phi$$

$$y = r (BA)^{-1/2} (Kn)$$

$$(Kn)^{-1} = n_0 \sigma (BA)^{1/2}$$

$$q_\infty = \sqrt{\frac{m}{kT_\infty}} \tau(\vec{x} + \hat{a}s), \quad q_e = \sqrt{\frac{m}{kT_e}} \tau^*(\vec{x} + \hat{r}s') \quad (3-12)$$

The inhomogeneous term in Eq. (3-11) contains the variable $q_\infty \equiv \sqrt{\frac{m}{kT_\infty}} \tau (\dot{\mathbf{x}} + \hat{\mathbf{a}}s)$, where $\hat{\mathbf{a}}$ is a unit vector in the direction of the undisturbed wind. This quantity is directly proportional to the number of collisions experienced by a molecule traveling in a straight line from infinity to the point in question in the direction of the undisturbed wind. Written explicitly, it has the form:

$$\frac{q_\infty}{W_\infty} = y^{-1} \int_{-\infty}^0 dt \frac{\left[1 + \left(\frac{u_M}{u_\infty} \right)^2 - 2 \frac{u_M}{u_\infty} \cos \delta \right]^{1/2} \exp \left\{ -\Lambda_\infty^2 (1 - \cos \mu)^2 \right\}}{1 + t^2 + 2t \cos \beta^* + \frac{Kn^2}{y} \exp \left\{ -\Lambda_\infty^2 (1 - \cos \mu)^2 \right\}}$$

$$\cos \mu = \frac{\cos \theta + t \cos \psi}{\sqrt{1 + t^2 + 2t \cos \beta^*}}$$

$$\cos \delta = \frac{\cos \beta^* + t}{\sqrt{1 + t^2 + 2t \cos \beta^*}}$$

$$\cos \beta^* = \cos \psi \cos \theta + \sin \psi \sin \theta \cos \phi \quad (3-13)$$

As $y \rightarrow \infty$, the number of collisions vanishes and the inhomogeneous term in Eq. (3-11) approaches unity. As $y \rightarrow 0$, the number of collisions experienced becomes very large and the inhomogeneous term vanishes exponentially. The number of collisions also becomes large when $\phi = 0$ and $\theta = \psi$, since the molecule has then had to traverse the near singularity in exhaust gas density at the origin. Physically, the ray on the opposite side of the nozzle exit from the wind is shielded from the ambient molecules for finite distances r from the exit. The nature of q_∞ near the singular ray

corresponding to $\cos\beta^* = 1$ may be analyzed as follows: The behavior is dominated by the singularity at $\cos\beta^* = 1$, as y approaches infinity or Kn vanishes. Thus, the quantities $\cos\mu$ and $\cos\delta$ in Eq. (3-13) may be replaced by their values at $\cos\beta^* = 1$, i.e.

$$\cos\mu \cong -\cos\psi, \quad 1+t \leq 0$$

$$\cos\mu \cong \cos\psi, \quad 1+t > 0$$

$$\cos\delta \cong -1, \quad 1+t \leq 0$$

$$\cos\delta \cong 1, \quad 1+t > 0$$

Upon inserting these values into Eq. (3-13) the integral for q_∞ may be evaluated explicitly as:

$$\begin{aligned} \frac{q_\infty}{W_\infty} &\cong \frac{1}{y} \left\{ \left(1 + \frac{u_M}{u_\infty} \right) \exp \left[-\Lambda_\infty^2 (1 + \cos\psi)^2 \right] \left[\frac{1}{a} \tan^{-1} \left(\frac{-1 + \cos\beta^*}{a} \right) + \frac{\pi}{2a} \right] \right. \\ &\quad \left. + \left| 1 - \frac{u_M}{u_\infty} \right| \exp \left[-\Lambda_\infty^2 (1 - \cos\psi)^2 \right] \left[\frac{1}{b} \tan^{-1} \left(\frac{\cos\beta^*}{b} \right) - \tan^{-1} \left(\frac{-1 + \cos\beta^*}{b} \right) \right] \right\} \\ a &= \left\{ 1 - \cos^2\beta^* + \left(\frac{Kn}{y} \right)^2 \exp \left[-\Lambda_\infty^2 (1 + \cos\psi)^2 \right] \right\}^{1/2} \\ b &= \left\{ 1 - \cos^2\beta^* + \left(\frac{Kn}{y} \right)^2 \exp \left[-\Lambda_\infty^2 (1 - \cos\psi)^2 \right] \right\}^{1/2} \end{aligned} \quad (3-14)$$

This expression is exact along the singular ray $\cos\beta^* = 1$, where it reduces to:

$$\frac{q_\infty}{W_\infty} = \frac{\pi}{2}(\text{Kn})^{-1} \left\{ \left(1 + \frac{u_M}{u_\infty} \right) \exp \left[\frac{-\Lambda_\infty^2}{2} (1 + \cos\psi)^2 \right] + \left| 1 - \frac{u_M}{u_\infty} \right| \exp \left[\frac{-\Lambda_\infty^2}{2} (1 - \cos\psi)^2 \right] \right\} \quad (3-15)$$

Along the singular ray, the hypersonic approximation breaks down for large y , since the boundary condition at infinity requires q_∞ to vanish there. Actually, unscattered molecules arriving from directions other than that of the freestream flow reach the ray $\theta = \psi$, $\phi = 0$ for large y , permitting the boundary condition to be satisfied. Along any adjacent ray corresponding to a fixed value of $\cos\beta^*$ such that $\cos\beta^* \neq 1$, when $(\text{Kn}/y)^2$ is sufficiently small compared with $1 - \cos^2\beta^*$, Eq. (3-14) reduces to:

$$\begin{aligned} \frac{q_\infty}{W_\infty} \approx \frac{\pi}{2y} \sqrt{1 - \cos^2\beta^*} \left\{ \left(1 + \frac{u_M}{u_\infty} \right) \exp \left[-\Lambda_\infty^2 (1 + \cos\psi)^2 \right] \right. \\ \left. + \left| 1 - \frac{u_M}{u_\infty} \right| \exp \left[-\Lambda_\infty^2 (1 - \cos\psi)^2 \right] \right\} \end{aligned} \quad (3-16)$$

Thus, the boundary condition at infinity is recovered, but with increasing slowness as the singular ray is approached. Note that the quantity $y \sqrt{1 - \cos^2\beta^*}$ is proportional to the distance in the plane perpendicular to the ray $\beta^* = 1$ from the ray to the point in question. The "shadow" region is then a cylindrical tube surrounding the singular ray. Since the inhomogeneous term $W_\infty^{-2} H_4(W_\infty, q_\infty)$ is roughly an exponential in $(-q_\infty/W_\infty)$, the width of the shadow region is given (in units $\sqrt{\text{BA}} \text{Kn}^{-1}$) by the factor multiplying $(y \sqrt{1 - \cos^2\beta^*})^{-1}$ in Eq. (3-16).

Now consider the homogenous term in Eq. (3-11). The variable $q_e = (m/kT_e)\tau^*$ has the explicit form:

$$\frac{q_e}{W_e(y')} = (Kn)^{-1} \frac{u_\infty}{u_e(y')} \exp \left\{ -\frac{1}{2} \Lambda_\infty^2 (1 - \cos \theta)^2 \right\} \left[1 + \frac{u_M^2}{u_\infty^2} - 2 \frac{u_M}{u_\infty} \cos \epsilon \right]^{1/2} \\ \left\{ \tan^{-1} \left[\frac{y}{Kn} \exp \frac{1}{2} \Lambda_\infty^2 (1 - \cos \theta)^2 \right] \right. \\ \left. - \tan^{-1} \left[\frac{y'}{Kn} \exp \frac{1}{2} \Lambda_\infty^2 (1 - \cos \theta)^2 \right] \right\} \quad (3-17)$$

The quantity q_e is proportional to the number of collisions experienced by a molecule initially penetrating to a distance y' along a given radial ray as it travels outward along the ray to the field point at y . Note that $q_e/W_e(y')$ becomes very large ($\propto (Kn)^{-1}$) for $\theta < 60^\circ$ and realistic values of Λ_∞ and u_∞/u_0 at $y' = 0$ for fixed y . Since the function $H_3(W_e, q_e)$ is roughly exponential in $(-q_e/W_e)$, the probability that those few molecules deposited upstream of the point can penetrate to the other side is very small. Moreover, the contribution to the density at any point from molecules scattered radially inward towards the nozzle is exponentially smaller in W_e^2 than that from molecules scattered radially outward away from the nozzle. For these reasons, the lower limit of integration in the homogenous term of Eq. (3-11) is the origin. Similarly, the overwhelming preponderance of outward scattering events means that there is no contribution to the number density at y from points $y' > y$ on that ray. Further details are given in Appendix A. Finally, the functions H_n may be simplified by applying the method of steepest descent once again. The result, valid for $p \gg 1$ and $Z \equiv q/p^3$ finite, is the first term in Anderson and Macomber's (1964)⁽¹⁶⁾ asymptotic expansion:

$$H_n(P, q) = \frac{(p t_o)^{n-2}}{(1 + 2Z/t_o^3)^{1/2}} \exp \left\{ \frac{-p^2 Z}{t_o} \left[1 + \frac{1}{2} \frac{Z}{t_o^3} \right] \right\}$$

$$t_o = \left\{ \frac{1}{3} + \frac{Z}{2} + \frac{1}{27} + \sqrt{\frac{Z}{27} + \frac{Z^2}{4}} \right\}^{1/3} + \left\{ \frac{Z}{2} + \frac{1}{27} - \sqrt{\frac{Z}{27} + \frac{Z^2}{4}} \right\}^{1/3}$$

$$Z = q/p^3 \quad (3-18)$$

Note that as $q \rightarrow 0$, $H_n(P, 0) \cong p^{n-2}$, while for large $q > 0$:

$$H_n \sim \frac{q^{(n-2)/3}}{(3/2)^{1/2}} \exp \left\{ -\frac{3}{2} q^{2/3} \right\}$$

The quantity $p^2 Z$ in the exponential is equal to q_∞ / W_∞ in the inhomogeneous term of Eq. (3-11), and to q_e / W_e in the homogeneous term. These quantities are independent of W_∞ and W_e , respectively. Thus, the quantity W_∞ and W_e enter the H_n functions only through the quantity Z , which is formally $O(W_\infty^{-2})$ or $O(W_e^{-2})$ for fixed y . These terms are retained in Eq. (3-18) to allow y to vary from a moderate multiple of Kn to values $\gg 1$. The principal effect of this variation is to shift the location of the saddle point t_o for radius of $y \leq \frac{1}{2}$. Although the shift is not large, the presence of the quantity t_o in the exponent of Eq. (3-18) can change the computed value of n/n_∞ at a given location by as much as a factor of two.

The physical picture represented by Eq. (3-11) may be summarized as follows: Molecules entering in a beam parallel to the undisturbed flow are scattered out of the beam by the exhaust gas, which is unaffected by the process. The scattered molecules are thus deposited along each radial ray in accordance with the inhomogeneous term in Eq. (3-11). The molecules are then caught up in the radial expansion and swept away from the nozzle, undergoing additional collisions as they proceed radially outward. The speed ratio of both the incident beam and the scattered gas is so high that

the thermal spread in molecular velocities may be ignored, in comparison with the velocities considered. The exhaust gas density is so high in the vicinity of the nozzle exit that no molecules can penetrate this region. As the radial distance from the nozzle exit increases, the penetration process becomes more efficient. Ultimately, the exhaust gas density is sufficiently low for the ambient molecules to pass through the plume undisturbed, and the ambient density is recovered. The phenomena outlined above are illustrated schematically in Fig. 3-3.

The remainder of this paper deals with the solution of Eq. (3-11), and the computation of two examples. The following section contains an asymptotic, analytic solution of this equation, valid far from the nozzle exit. Section 3.5 discusses the computational procedures employed in the direct numerical solution of Eq. (3-11) and in the evaluation of the asymptotic result of Section 3.6. The analytical and numerical methods explained in these two sections are applied to an axially symmetric flow ($\psi = 0$) and a nonsymmetric, "side blowing" flow ($\psi = 90^\circ$) in Section 3.6.

3.4 The Asymptotic Solution

When the radial coordinate y is $0(1)$, the solution to Eq. (3-11) may be readily obtained. Under these circumstances, $u_e(y')$ approaches u_M , while q_e/W_e becomes:

$$\frac{q_e}{W_e} \cong \frac{u_\infty}{u_M} \left[1 + \left(\frac{u_M}{u_\infty} \right)^2 - 2 \frac{u_M}{u_\infty} \cos \epsilon \right]^{1/2} \exp \left[-\Lambda_\infty^2 (1 - \cos \theta)^2 \right] \left(\frac{1}{y'} - \frac{1}{y} \right) \quad (3-19)$$

Thus, q_e/W_e is $0(1)$, which means that the quantity $Z \equiv q_e/W_e^3$ in the function H_3 may be set equal to zero, reducing H_3 to an exponential. Eq. (3-11) then reduces to:

$$\left[\frac{n}{n_\infty} - \frac{1}{W_\infty^2} H_4(y) \right] J(y) = \int_0^y dy' G(y') \frac{n}{n_\infty}(y')$$

$$J(y) = y^2 \exp \left\{ - \frac{u_\infty}{u_M y} \left[1 + \left(\frac{u_M}{u_\infty} \right)^2 - 2 \left(\frac{u_M}{u_\infty} \right) \cos \epsilon \right]^{1/2} \right. \\ \left. \exp \left[- \Lambda_\infty^2 (1 - \cos \theta)^2 \right] \right\} \\ G(y) = \frac{J(y)}{y^2} \frac{u_\infty}{u_M} \left[1 + \left(\frac{u_M}{u_\infty} \right)^2 - 2 \frac{u_M}{u_\infty} \cos \epsilon \right]^{1/2} \\ \exp \left[- \Lambda_\infty^2 (1 - \cos \theta)^2 \right] \quad (3-20)$$

Equation (3-20) is readily solved by differentiating with respect to y to obtain a first-order differential equation for the quantity $\left[n/n_\infty - 1/W_\infty^2 H_4(y) \right] J(y)$. Examination of Eq. (3-20), as y approaches zero, shows that this quantity should vanish at the origin. Thus:

$$\left[\frac{n}{n_\infty} - \frac{1}{W_\infty^2} H_4(y) \right] = \frac{u_\infty}{y^2 u_M} \exp \left[- \Lambda_\infty^2 (1 - \cos \theta)^2 \right] \int_0^y dy' \frac{1}{W_\infty^2} H_4(y') \quad (3-21)$$

The function $H_4(y)$ can be simplified in a similar manner away from the singular ray. The function q_∞ then has the form:

$$\frac{q_{\infty}}{W_{\infty}} \equiv \frac{\Omega}{y}$$

$$\Omega = \int_{-\infty}^0 dt \frac{\left[1 + \left(u_M/u_{\infty} \right)^2 - 2 \left(u_M/u_{\infty} \right) \cos \delta \right]^{1/2} \exp \left[-\lambda_{\infty}^2 (1 - \cos \mu)^2 \right]}{1 + t^2 + 2t \cos \beta^*}$$

Then, provided that the numerical value of Ω on the ray under consideration is not too large, q_{∞}/W_{∞} may be set equal to zero in the function $(1/W_{\infty}^2)H_4(W_{\infty} q_{\infty})$, thereby reducing it to an exponential in $(-\Omega/y)$. The quadrature on the righthand side of Eq. (3-21) may then be evaluated in terms of the exponential integral function $E_2(Z)$, yielding the result:

$$\frac{n}{n_{\infty}} = \frac{1}{W_{\infty}^2} H_4(W_{\infty}, q_{\infty}) + \frac{u_M}{u_M y} \left[1 + \left(\frac{u_M}{u_{\infty}} \right)^2 - 2 \left(\frac{u_M}{u_{\infty}} \right) \cos \epsilon \right]^{1/2} \exp \left[-\lambda_{\infty}^2 (1 - \cos \theta)^2 \right] \cdot E_2 \left(\frac{\Omega}{y} \right)$$

$$E_2(Z) = \int_1^{\infty} \frac{e^{-Zt}}{t^2} dt$$

The first term in the solution (3-23) could also formally be replaced by $\exp \left\{ -\Omega/y \right\}$ to the present order of accuracy. However, the analysis in this section can be interpreted as an attempt to find an approximate expression for the scattered gas contribution to the number density, as represented by the homogeneous term in

Eq. (3-11). The second term in the solution (3-23) is the desired result, as is the righthand side of Eq. (3-21). However, the other expression is too complicated to study analytically, and sufficiently expensive in computer time (relative to the direct numerical solution of Eq. (3-11)) to warrant its use without the further approximation represented by Eq. (3-23).

Now consider the behavior of the solution as a function of y and θ . For small y (assuming for the moment that the asymptotic solution is at least qualitatively correct) the function $E_2(\Omega/y)$ has the asymptotic expansion

$$E_2 \sim \frac{ye^{-\Omega/y}}{\Omega} \left\{ 1 + O\left(\frac{\Omega}{y}\right) \right\}$$

The scattered gas contribution becomes very small as the nozzle exit is approached because few ambient molecules are able to penetrate the dense region of the plume. For large angles θ , the factor $\exp \left\{ -\Lambda_\infty^2 (1 - \cos \theta)^2 \right\}$ (representing the angular dependence of the exhaust gas density distribution) cuts off the scattered gas contribution because there are so few exhaust gas molecules to serve as scatterers. For large y , $E_2(\Omega/y)$ may be approximated by:

$$E_2 \sim \frac{\Omega}{y} \log \left(\frac{\Omega}{y} \right)$$

Thus, the scattered gas density rises to a peak, then decays much more slowly with increasing y . The decay is caused by the increasing volume in the plume available to molecules scattered much nearer to the nozzle and then convected radially outward. The additional local scattering far from the nozzle contributes weakly, accounting for the logarithmic factor in the scattered result. However, the exhaust gas density ultimately decreases to the point where the unscattered contribution dominates, permitting the uniform boundary condition at infinity to be recovered.

3.5 The Numerical Computation Procedure

The numerical computation of n/n_∞ requires the evaluation of the inhomogeneous term in Eq. (3-11) or Eq. (3-23), together with a procedure for calculating the homogeneous term in the integral equation. The evaluation of the asymptotic approximation to the H_n functions is straightforward, as is the computation of the function E_2 , as a function of its argument. Hence attention is confined to the computation of q_∞ , which determines the value of the inhomogeneous term; and to the evaluation of the homogeneous term in Eq. (3-11).

The computation of the integral defining q_∞ will be considered first. Note that the integrand is not singular in the entire range of integration, since its denominator is equal to or greater than one throughout this range. However, as is shown in Section 3.3, the limit of q_∞ as $y \rightarrow \infty$ and $\cos\beta^* \rightarrow 1$ is non-uniform; that is, the value of the limit depends on the order in which these two limiting processes take place. Numerically, this non-uniformity means that one must be very careful in evaluating this integral when both y is $O(1)$ or larger and $\cos\beta^*$ is very close to 1. For such values of y and $\cos\beta^*$, most of the contributions to the integral come from points very close to $t = -1$, and the accuracy with which $\cos\delta$ and $\cos\mu$ can be evaluated at these points is limited by the arithmetical precision of a computer.

A close examination of the variation of the integrand J of Eq. 3-13 with respect to t shows that the integrand varies smoothly in the entire range of integration, so long as $\cos\beta^*$ is not close to 1. For $\cos\beta^*$ near 1, the integrand has very sharp variations near $t = -1$, and a peak value in that neighborhood. For $\cos\beta^* = 1$, the peak of the integrand is exactly at $t = -1$, and is discontinuous.

In view of the above described peculiarities at the integrand J , the following method was devised to compute the integral. The integral, I , is divided into two parts, I_L and I_R :

$$I = I_L + I_R$$

$$I_L = \int_{-\infty}^{-1-\epsilon_1} J(t, y^*) dt$$

$$I_R = \int_{-1+\epsilon_2}^0 J(t, y^*) dt$$

where ϵ_1 and ϵ_2 are two small positive numbers. ϵ_1 is chosen such that the omitted part of the integral, from $-1-\epsilon_1$ to -1 divided by I_L , is equal to the specified fractional tolerance (TOL) for the computation of the inhomogeneous and homogeneous terms. ϵ_2 is chosen in a similar fashion. It can be shown that, for $\cos\beta^* = 1$, ϵ_1 and ϵ_2 are given by:

$$\epsilon_1 = \frac{\pi}{2} \text{ TOL } e^{-\frac{\Lambda_\infty^2}{2} (1+\cos\psi)^2} \frac{\text{Kn}}{y}$$

$$\epsilon_2 = \text{TOL } e^{-\frac{\Lambda_\infty^2}{2} (1-\cos\psi)^2} \arctan \left[r^* e^{\frac{\Lambda_\infty^2}{2} (1-\cos\psi)^2} \right] \frac{\text{Kn}}{y} \quad (3-24)$$

Equations (3-24) are, in fact, used to compute ϵ_1 and ϵ_2 for any value of $\cos\beta^*$. It can be shown that these values of ϵ_1 and ϵ_2 are smaller than the required values, thus resulting in smaller values for the omitted parts of the integral.

I_L is computed in steps Δt of the integration variable t , starting from $t = -1 - \epsilon_1$, and advancing to the left towards $t = -\infty$. The magnitude of each step Δt is determined, such that the integrand changes by about one order of magnitude in the range of the step. The contribution to I_L from each step is completed through a six-point Gaussian integration. I_R is computed in a similar, steplike fashion, starting from $t = -1 + \epsilon_2$ and advancing to the right towards the origin. I_L and I_R are computed concurrently, so that the total integral I is progressively built up from both sides of the point $t = -1$. The computation of I_L is terminated when the most recent contribution to I_L , divided by the accumulated I , is less than the fractional tolerance, TOL, of the computation. The computation of I_R is terminated in a similar fashion, or when the origin is reached.

Now consider the calculation of the homogeneous term in the integral equation. For computational purposes, it is more convenient to work with the radial coordinate r^* , defined by:

$$r^* \equiv \frac{r}{\sqrt{BA}} = (Kn)^{-1} y \quad (3-25)$$

The initial growth of the homogeneous term in this variable is slow and well-behaved, taking place over the range $10 < r^* < 100$ along most radial rays. Letting the dimensionless, inhomogeneous and homogeneous quantities in Eq. (3-11) be n_i^* and n_h^* , respectively, this equation may be written in the form:

$$n_h(r^*) = \int_{r_1^*}^{r^*} \tilde{K}(r', r^*) n^*(r') dr' \quad (3-26)$$

$$n^*(r') = n_i^*(r') + n_h^*(r') \quad (3-27)$$

In the "exact" definition of the integral equation, r_1^* is equal to zero. However, in the numerical evaluation of the integral of this equation r_1^* can be much larger than zero as will be shown later.

Now, consider the following mesh of points:

$$r_1^*, r_2^*, r_3^* \dots r_{m-2}^*, r_{m-1}^*, r_m^*, r_{m+1}^*$$

$$r_{m+1}^* = r_m^* + h_m \quad (3-28)$$

Note that, in general, a variable mesh size is assumed. Assume that the values of n^* are known at all points up to and including the point r_m^* . The value of n_h^* at the next point, r_{m+1}^* , is computed by the following procedure.

The integral of equation (3-26) is divided into two parts so that:

$$n_h^*(r_{m+1}^*) = I_1 + I_2 \quad (3-29)$$

where

$$I_1 = \int_{r_m^*}^{r_{m+1}^*} \tilde{K}(r', r_{m+1}^*) n^*(r') dr' \quad (3-30)$$

$$I_2 = \int_{r_1^*}^{r_m^*} \tilde{K}(r', r_{m+1}^*) n^*(r') dr' \quad (3-31)$$

I_1 is evaluated by the parabolic integration formula (3-B10) of Appendix B.

Thus:

$$\begin{aligned}
 I_1 = & - \frac{h_m^3}{6h_{m-1}(h_m + h_{m-1})} K(r_{m-1}^*, r_{m+1}^*) n^*(r_{m-1}^*) \\
 & + \frac{h_m(3h_{m-1} + h_m)}{6h_{m-1}} K(r_m^*, r_{m+1}^*) n^*(r_m^*) \\
 & + \frac{h_m(3h_{m-1} + 2h_m)}{6(h_m + h_{m-1})} K(r_{m+1}^*, r_{m+1}^*) \left[n_i^*(r_{m+1}^*) + n_h^*(r_{m+1}^*) \right]
 \end{aligned}
 \tag{3-32}$$

Substituting I_1 from Eq. (3-32) in Eq. (3-29), and solving the resulting equation for $n_h^*(r_{m+1}^*)$, one obtains:

$$n_h^*(r_{m+1}^*) = \frac{I_1' + I_2}{1 - \left[\frac{h_m(3h_{m-1} + 2h_m)}{6(h_m + h_{m-1})} \right] K(r_{m+1}^*, r_{m+1}^*)}$$

where I_1' is equal to I_1 , as given by Eq. (3-32), with $n_h^*(r_{m+1}^*)$ set to zero.

As can be seen from Eqs. (3-31) and (3-32), the righthand side of Eq. (3-33) involves:

- (i) The values of n^* for all points up to and including the point r_m^* , which are known; and
- (ii) The value of n_i^* at the point r_{m+1}^* which can be evaluated separately.

Thus, the righthand side of Eq. (3-33) involves quantities that are known, or can be evaluated independently of $n_h^*(r_{m+1}^*)$; therefore, Eq. (3-33) is an explicit expression for the unknown $n_h^*(r_{m+1}^*)$.

I_2 is computed by successive applications of the parabolic integration formula (3-B11) of Appendix B to three points at a time, starting with the point r_m^* and advancing to the left towards the point r_1^* . The reason for computing I_2 backwards, in this way, is that the kernel $\tilde{K}(r', r_{m+1}^*)$ decreases sharply as r' becomes smaller and smaller than r_m^* , and thus the contributions to I_2 decrease sharply. This means that the computation of I_2 can be terminated when a desired accuracy is achieved, much before reaching the initial point r_1^* . The computation of I_2 is terminated when the most recent contribution to I_2 , divided by the sum of I_2 (accumulated) and I_1' , is smaller than a specified fractional tolerance (TOL), which is also the tolerance within which n_1^* is computed. If m is even, and the computation of I_2 must be extended all the way to r_1^* , then the last contribution to I_2 is from two points, rather than three, namely, points r_2^* and r_1^* , and formula (3-B9) of Appendix B is applied instead of formula (3-B11).

The procedure described above for the computation of n_h^* requires that n_h^* be known at the first three points, r_1^* , r_2^* and r_3^* . The value of n_h^* at r_1^* is the initial condition of the problem, and when r_1^* is taken equal to zero, one has the "exact initial condition" of the problem, which is $n_h^*(0) = 0$. A close examination of the situation reveals that, as one travels along a radial ray from the origin outward, n_1^* decays rapidly from 1 to a very small value, then increases back to 1, while n_h^* increases slowly from 0 to some maximum value, then decays back to zero. Thus, in the numerical evolution of n_h^* , a great deal of computer time is saved, without any loss in accuracy, by starting the solution of some r_1^* larger than zero, with the approximate initial condition $n_h^* = 0$ at r_1^* . r_1^* is selected so that it is in the region where n_1^* has its minimum plateau. The rapidly decaying kernel annihilates the errors associated with this approximate initial condition. Thus:

$$n_h^*(r_1^*) = 0 \quad (3-34)$$

The value of n_h^* at r_2^* is computed by evaluating I_1 in Eq. (3-30) through the trapezoidal rule (I_2 in this case is, of course, equal to zero). As for the value of n_h^* at r_3^* , it is computed by evaluating both I_1 and I_2 in Eqs. (3-30) and (3-31) by the trapezoidal rule. Thus:

$$n_h^*(r_2^*) = \frac{h_1/2 \left[\tilde{K}(r_1^*, r_2^*) n^*(r_1^*) + \tilde{K}(r_2^*, r_2^*) n^*(r_2^*) \right]}{1 - (h_1/2) \tilde{K}(r_2^*, r_2^*)} \quad (3-35)$$

$$n_h^*(r_3^*) = \frac{1/2 \left[h_1 \tilde{K}(r_1^*, r_3^*) n^*(r_1^*) + (h_1 + h_2) \tilde{K}(r_2^*, r_3^*) n^*(r_2^*) + h_2 \tilde{K}(r_3^*, r_3^*) n^*(r_3^*) \right]}{1 - (h_2/2) \tilde{K}(r_3^*, r_3^*)} \quad (3-36)$$

If the integrating step, h_m , from r_m^* to r_{m+1}^* is too large, then the denominator in Eq. (3-33) can be small, or even negative. This must not be allowed since instabilities will result. Now, it can be shown that:

$$\tilde{K}(r_{m+1}^*, r_{m+1}^*) < \tilde{K}(r_m^*, r_m^*) \quad (3-37)$$

and, therefore, if the integrating step is chosen such that:

$$h_m = \frac{\alpha}{\tilde{K}(r_m^*, r_m^*)} \quad (3-38)$$

then the denominator of Eq. (3-33) is roughly equal to one to 0.5α . Thus, for sufficiently small values of the parameter α , instabilities can be avoided. The correct value of α for a given radial ray cannot be defined a priori, but one anticipates that a value between 0.1 and 1 should do. Indeed, in the applications discussed in the next section, the value $\alpha = 0.5$ was employed. This ambiguity in the right value of α notwithstanding, Eqs. (3-37) and (3-38) show that h_m increases as r_m^* increases, a very desirable result. Another criterion for the selection of h_m is derived by fitting a parabola to the values of n_h^* at the three points, r_{m-2}^* , r_{m-1}^* , and r_m^* , then extrapolating to a point r_{m+1}^* , where the fractional change in n_h^* is a small number β , on the order of 0.01 to 0.1. The value of β actually used is 0.05. The resulting value of h_m is compared to that given by Eq. (3-38), and the smaller of the two is selected. For the two initial integrations with the trapezoidal rule, a sufficiently small integrating step is taken readily satisfying the stability considerations discussed above.

The computer program is in FORTRAN IV, and has been run successfully on the UNIVAC 1108 system. Before final production runs were made, the accuracy, stability, and efficiency of the program were investigated through several test runs, by use of a trial integral equation whose exact solution was known.

The procedure for calculating n_i^* works very well for any value of r^* , so long as $\cos \beta^*$ is not equal to 1. For $\cos \beta^* = 1$, the computer program is only accurate for moderate values of r^* . However, the solution is not physically meaningful for r^* sufficiently large for y to be $O(1)$ on this ray. The procedure for calculating n_h^* is stable and accurate. It is efficient for values of θ equal to or less than about 45° if an accuracy of 0.1% (TOL = 0.001) is required. By accepting an error of 0.5% (TOL = 0.005), the program can be utilized out to angles θ of 60° . For larger values of θ , the value of the parameter α , required for an accurate solution, is so small that the integrating steps become very small, and a great deal of computer time is required to obtain the solution. For such values of θ , n_h^* can be computed much more efficiently from the asymptotic expression (3-23), valid quite close to the origin for such large angles. A computer program with the asymptotic expressions for n_h^* has also been developed, and works quite well.

For an accuracy of one part in a thousand (TOL = 0.001), it takes, on the average, about 30 sec of 1108 central processing unit (CPU) time to compute n_i^* and n_h^* along a radial ray, all the way from the origin to the value of r^* where the ambient condition is recovered. The CPU time required for the calculation of n_h^* is about three times that for n_i^* .

3.6 Numerical Results

The theoretical and numerical analyses described in the previous sections have been applied to the calculation of an axially symmetric flow ("aligned flow") $\psi = 0$: and to a "non-aligned" case, $\psi = 90^\circ$. The values of the remaining parameters needed to uniquely determine the solution for n/n_∞ were the same for both flows, and are listed in Table 3-I.

TABLE 3-I. Parameters Employed in Computed Results

Kn	W_∞	u_M/u_∞	γ	M_O	m/m_e
10^{-3}	6	0.3	1.3	4	0.8

The integral equation was solved directly, to an accuracy of 0.1%, on rays spaced at five-degree intervals for $\theta \leq 45^\circ$, and with a reduced accuracy of 0.5% for values of θ between 45° and 60° . Equation (3-23) was used to obtain results for angles θ greater than 60° .

First consider the aligned flow: Figure (3-4) illustrates the relative magnitude of the scattered and unscattered contributions to the density on the $\theta = 30^\circ$ ray. Near the nozzle exit, both contributions are small because most of the molecules in the incident, ambient stream are deposited before reaching the 30° ray. As y increases, more molecules are deposited on the ray, and then convected outward by the exhaust. Since the scattered gas at a given y station is an accumulation of molecules scattered earlier, this buildup is quite rapid, and gives rise to the overshoot in density depicted in the figure. The combination of the geometric relieving effect and reduced scattering discussed in Section 3.4 then reduces the scattered gas contribution very slowly (note the logarithmic scale) to zero. The unscattered gas density rises monotonically with increasing y to recover the boundary condition at infinity.

The above picture holds qualitatively on all rays, with only the magnitude and location of the maximum in the scattered gas contribution changing from ray to ray. Figures (3-5) and (3-6) show the development of the radial profiles with increasing θ . Near the thrust axis, the recovery of the ambient condition is slowest because the plume is densest. The density overshoot begins at about $\theta = 15^\circ$, and increases in magnitude with increasing θ , until peak values are reached for values of θ slightly larger than $\theta = 60^\circ$. The location of the peak moves closer to the nozzle with increasing θ . For larger angles, the density drops rapidly towards the ambient value, because the exhaust gas density is so low that no significant scattering takes place.

The results predicted by the present theory for values of y smaller than about 10^{-2} , corresponding to $r^* = 10$, must be treated with extreme caution. Since r^* measures the radial coordinate in units of exit radii (β is about 0.3 in the present example), phenomena on this scale may be strongly influenced by the details of the geometry of the body carrying the motor. Moreover, even in the absence of a finite body, the exhaust gas characteristics in the vicinity of the nozzle are not described

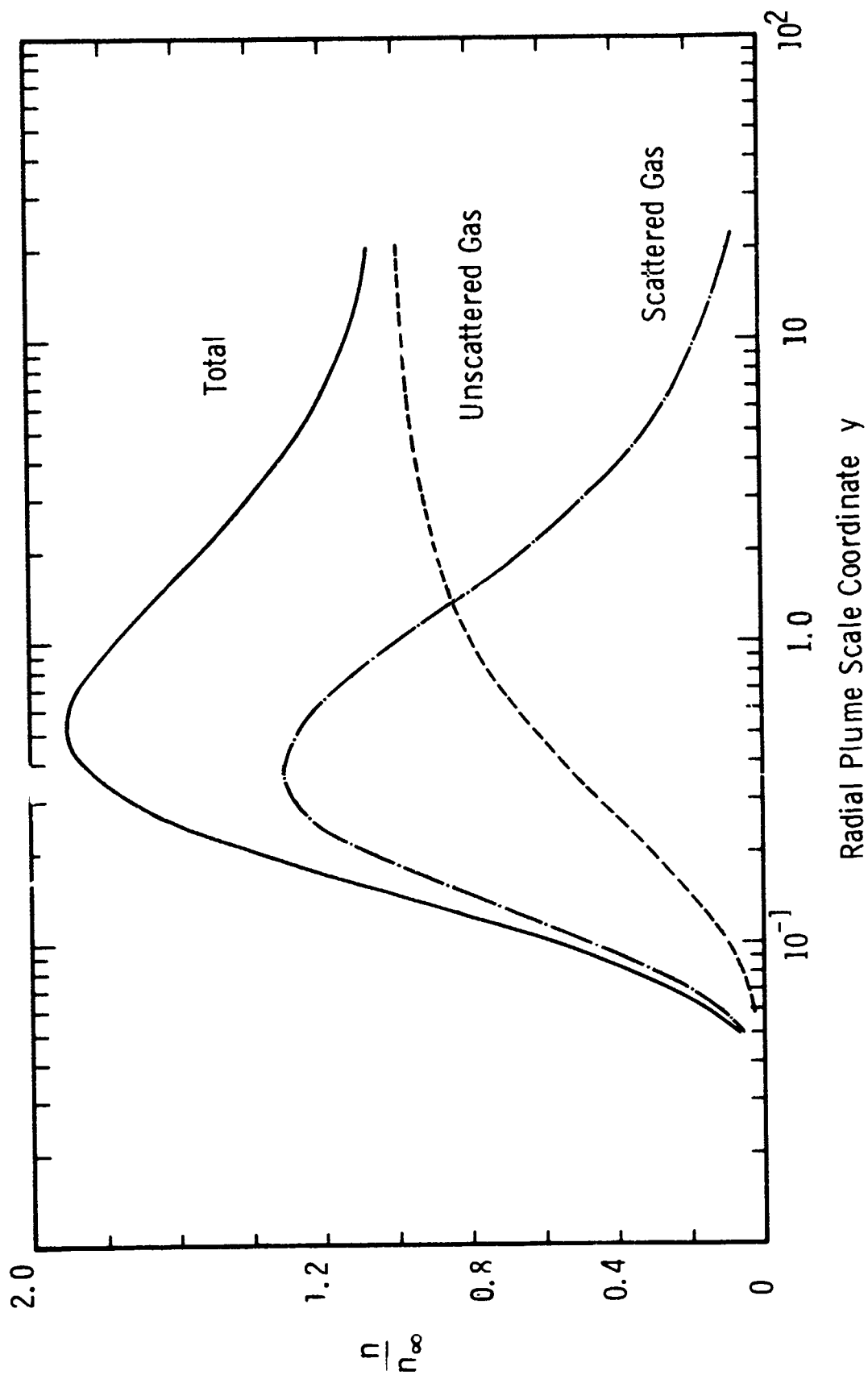


Figure 3.4 - Ambient Penetration of Exhaust Plume

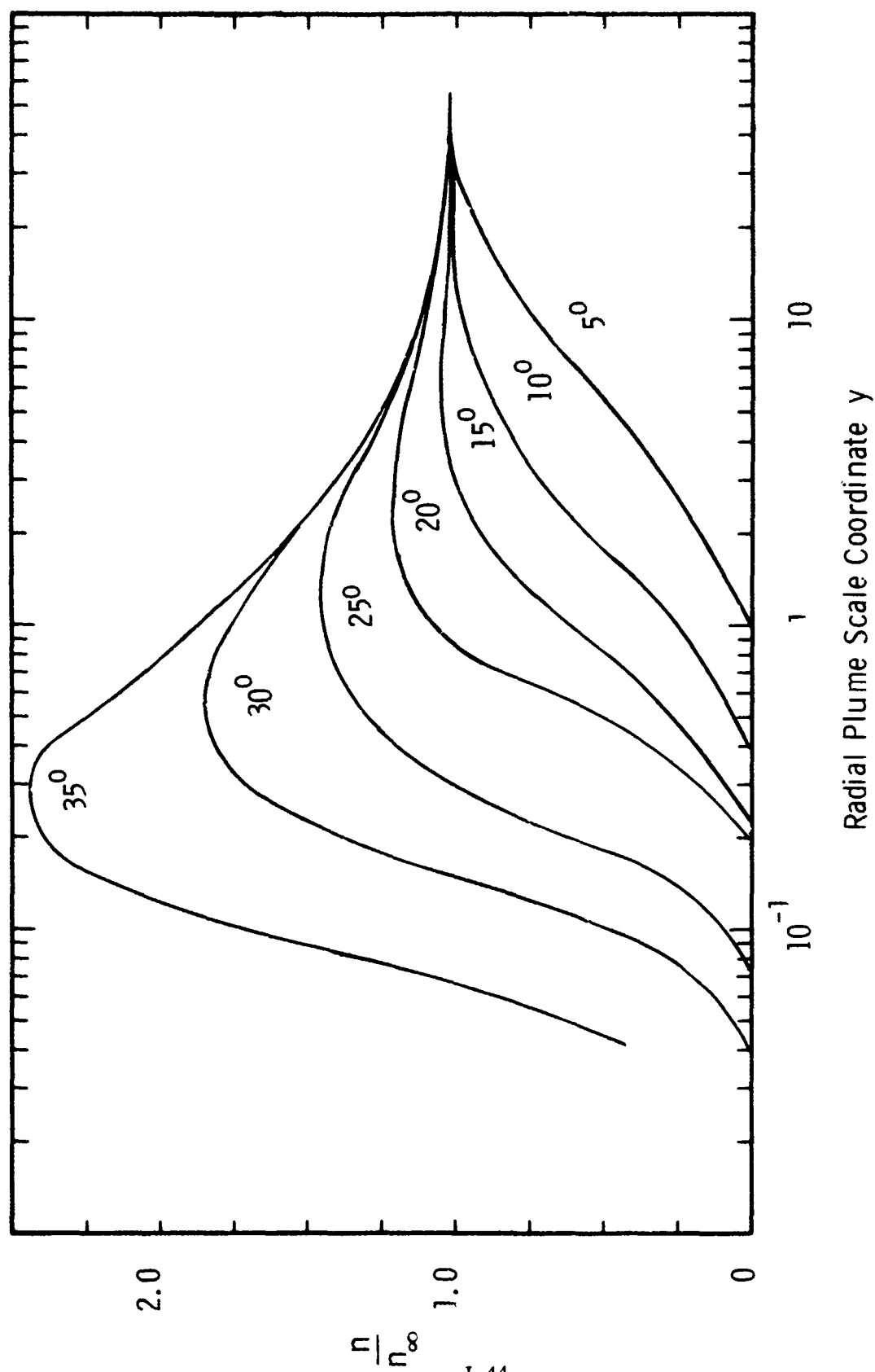


Figure 3.5 - Radial Density Distribution for Aligned Plume

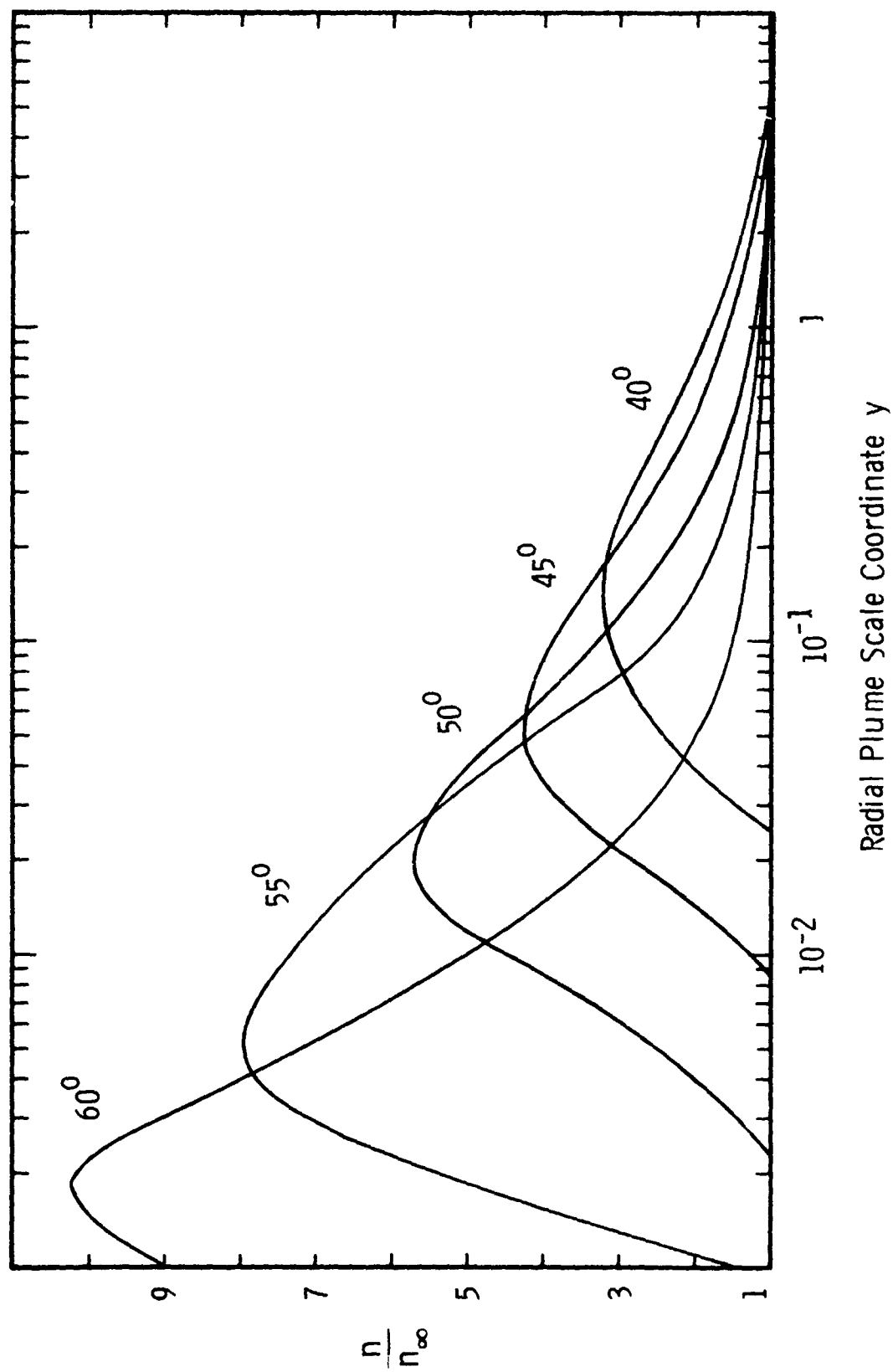


Figure 3.6 - Radial Density Distribution for Aligned Plume

accurately by Eq. (3-2). However, the solutions for larger y are not sensitive to the behavior of the results for $y \ll 10^{-2}$.

The density is plotted as a function of angle at several radial stations in Fig. (3-7). The ambient conditions are recovered progressively later in the expansion as θ decreases, since the region near the thrust axis is the least accessible to the atmospheric gases. Figure (3-8) shows the corresponding curves for the windward portion of the plane containing the wind and thrust vectors in the non-aligned case. The density distribution is qualitatively similar to that in the aligned flow. However, the asymmetry is such that the recovery must be made slower on the leeward side (Fig. (3-9)), because of the fact that the atmosphere must penetrate through the entire windward portion of the plume before reaching these rays. The singular ray is now at $\theta = 90^\circ$, on the leeward side. Although the model predicts some scattering along this ray, the value of q_∞/W_∞ is $O(e^{-\Lambda_\infty^2/K_n})$, which is less than 10^{-3} in the present problem.

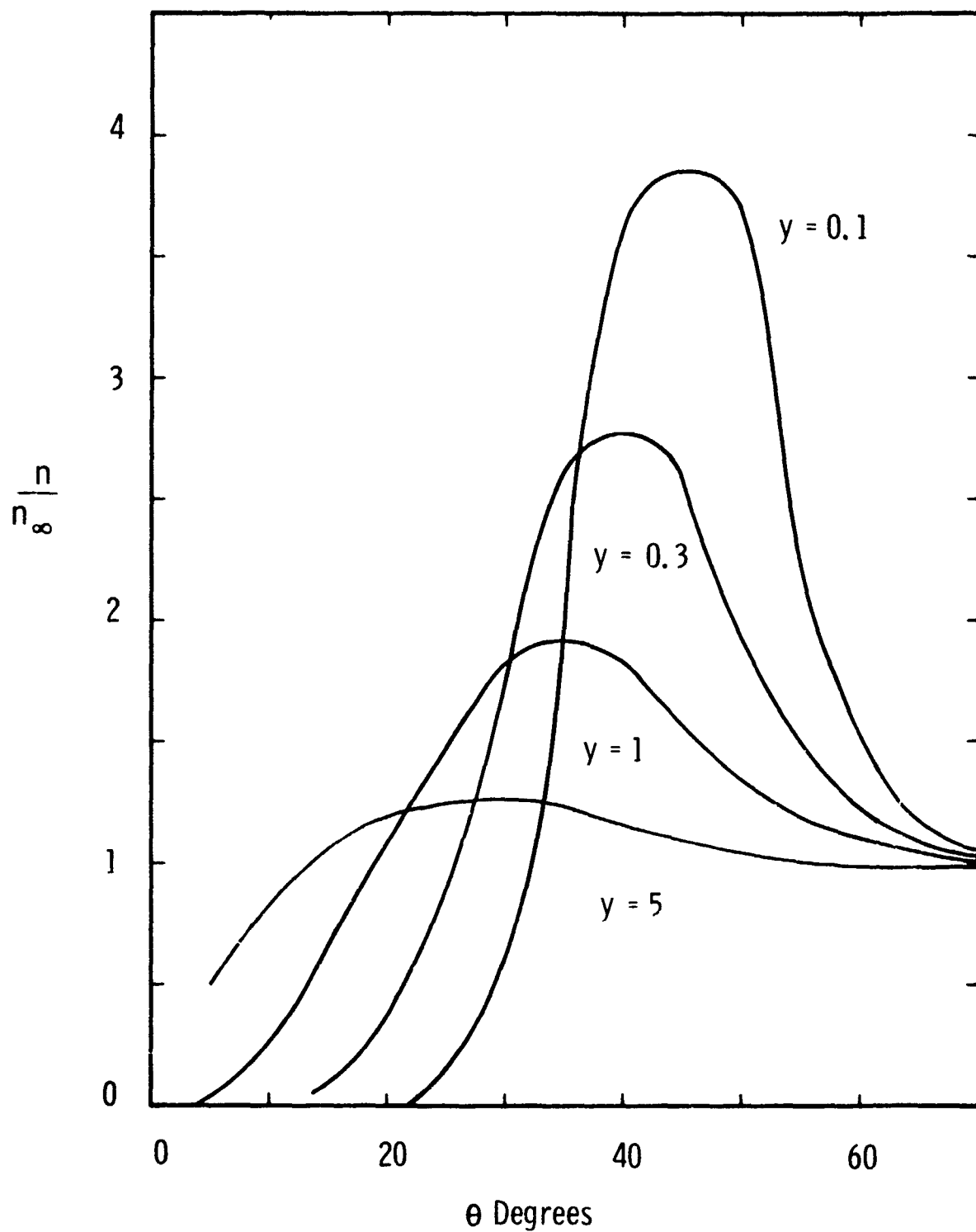


Figure 3.7 - Angular Density Distribution for Aligned Plume

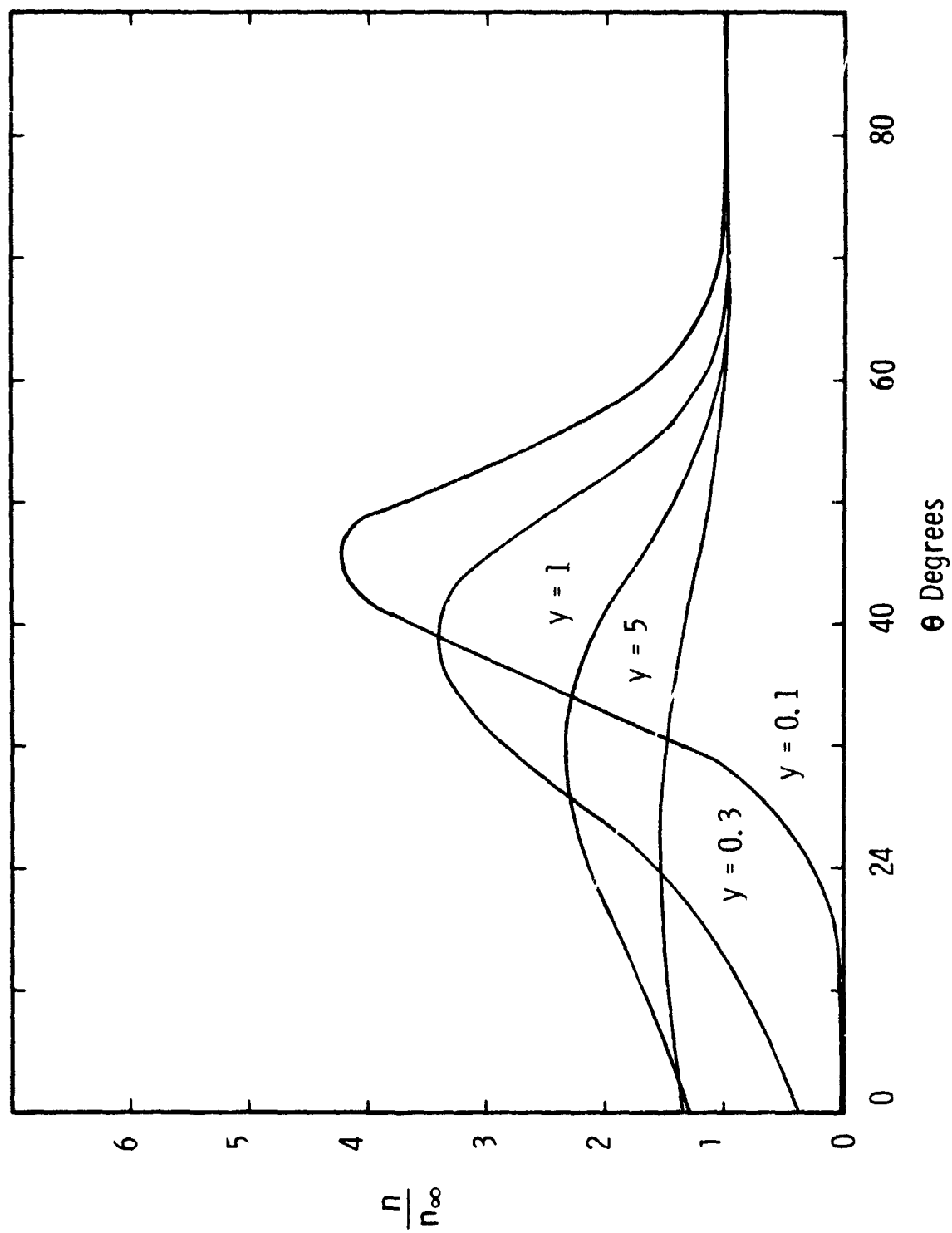


Figure 3.8 - Angular Density Distribution for Non-Aligned Plume Windward Side

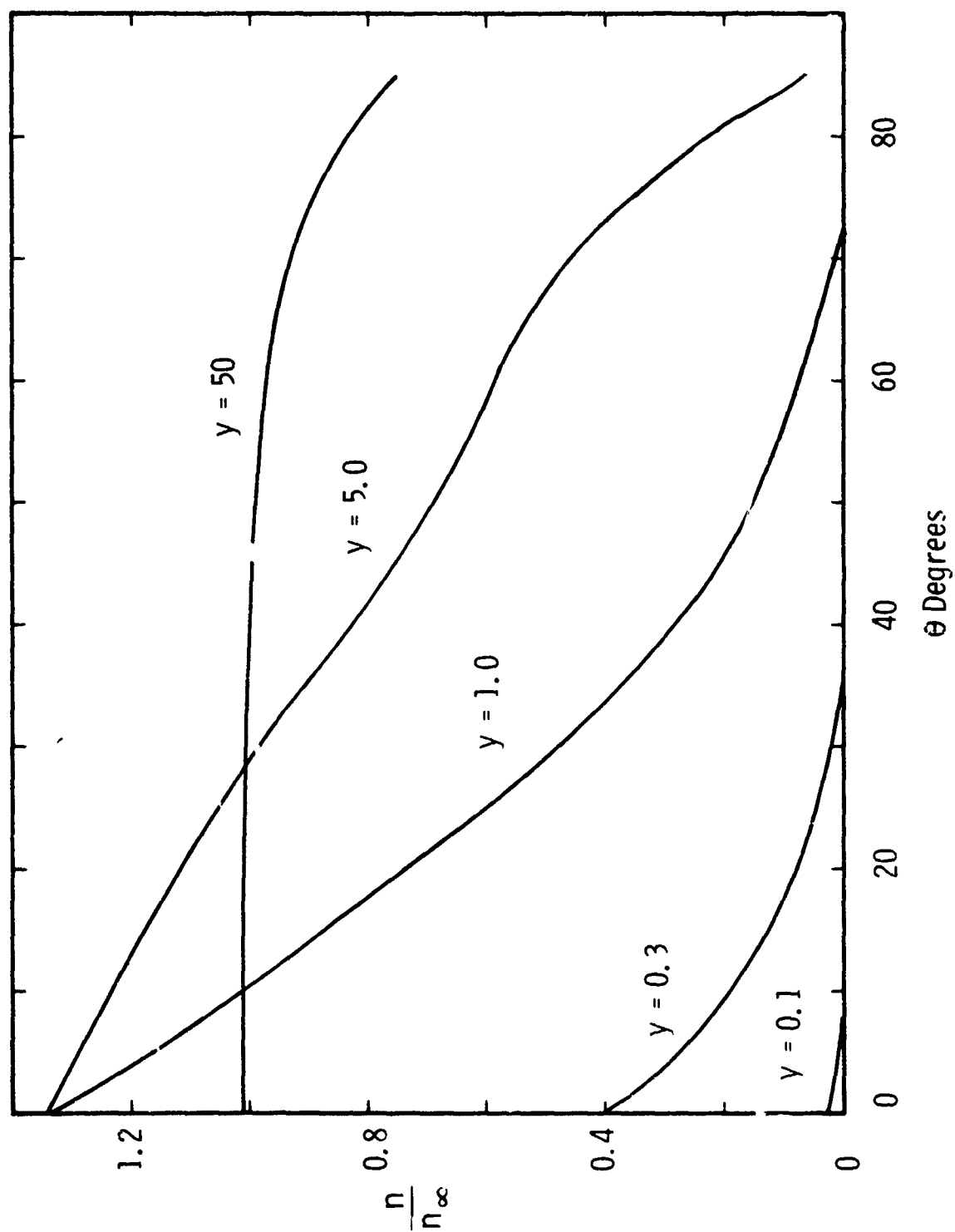


Figure 3.9 - Angular Density Distribution for Non-Aligned Plume Leeward Side

APPENDIX A. HYPERSONIC LIMIT - HOMOGENEOUS TERM

The homogeneous term in Eq. (3-7) may be rewritten (inverting the order of integration) as:

$$\int_{-\infty}^0 ds' \frac{1}{2\pi} \int_0^{2\pi} d\eta \int_0^{\pi} \sin \xi \, d\xi \sqrt{\frac{m}{kT_e}} \omega e^{-\frac{1}{2} W_e^2 (1 - \cos^2 \alpha)} H_3(W_e \cos \alpha, q_e) \frac{n}{n_{\infty}} \quad (3-A1)$$

$$q_e = \sqrt{\frac{m}{kT_e}} \int_{s'}^0 ds \, \omega(\vec{x} + \hat{v}s) \quad .$$

Here, $\cos \alpha$ is given by Eq. (3-6), while the quantities T_e , ω , W_e , and n/n_{∞} are functions of $\vec{x} + \hat{v}s'$. The basic assumption is analogous to that employed in Section 3.3, that the dominant contribution to the angular integrations over ξ and η comes from the neighborhood of $\cos \alpha = 1$, because of the large factor W_e^2 in the exponential in the integrand of term (3-A1). By letting $x = \cos \xi$ be the first integration variable, the exponential factor in term (3-A1) becomes:

$$-\frac{1}{2} W_e^2 \frac{r^2}{(\vec{x} + \hat{v}s')^2} f(x) \quad (3-A2)$$

$$f(x) = 1 - \left[x \cos \theta + \sqrt{1-x^2} \sin \theta \cos(\eta - \phi) \right]^2 \quad .$$

Although the quantity multiplying $f(x)$ in (3-A2) is itself a function of x , through its dependence on the variable $\vec{x} + \hat{v}s'$, the fact that it is large and positive for all values of \hat{v} means that the contribution to (3-A1) will be exponentially small, except for values of \hat{v} corresponding to $\cos \alpha = 1$. Examination of Eq. (3-6) shows that $\cos \alpha = 1$ can only occur for $\hat{v} = \hat{r}$. Thus, the exponential factor (3-A2) may be approximated by:

$$-\frac{1}{2} W_e^2 \frac{r^2}{(r + s')^2} f(x) \quad . \quad (3-A3)$$

W_e is a function of $\hat{r}(r + s')$ in Eq. (3-A3). The method of steepest descent may now be applied to (3-A1) in the same way that the corresponding integrals for the inhomogeneous term were evaluated in Section 3.3. The result implies that the remaining terms in the integral are to be evaluated at $x = \cos \theta$, $\eta = \phi$. When these values are inserted into the expression (3-6), then $\cos \alpha = 1$, as required for consistency, provided that $s' + r$ is positive. Where $s' + r$ is negative, $\cos \alpha = -1$, and the contribution to (3-A1) is again exponentially small in W_e , this time because of the fact that the function $H_3(-W_e, q_e)$ is $O(e^{-W_e^2/2})$. If now, the substitution $r' = s' + r$ is made in the integration over s' which remains in Eq. (3-A1), then the homogeneous term in Eq. (3-11) is recovered.

APPENDIX B. PARABOLIC INTEGRATION FORMULAE WITH VARIABLE INTEGRATION STEP

Consider the following mesh of three points x_1 , x_2 , and x_3 :

$$x_2 = x_1 + h_1, \quad x_3 = x_2 + h_2$$

and the following integrals of a function $f(x)$:

$$I_{1,2} = \int_{x_1}^{x_2} f(x) dx \quad (3-B1)$$

$$I_{2,3} = \int_{x_2}^{x_3} f(x) dx \quad (3-B2)$$

$$I_{1,3} = \int_{x_1}^{x_3} f(x) dx \quad (3-B3)$$

Obviously

$$I_{1,3} = I_{1,2} + I_{2,3} \quad (3-B4)$$

The objective here is to derive approximate expressions for these integrals, by use for $f(x)$ of the second-order, lagrange interpolating polynomial:

$$f(x) = \frac{f_1}{h_1(h_1 + h_2)} (x - x_2)(x - x_3) - \frac{f_2}{h_1 h_2} (x - x_1)(x - x_3) + \frac{f_3}{h_2(h_1 + h_2)} (x - x_1)(x - x_2) \quad (3-B5)$$

where $f_1 = f(x_1)$, and so on.

$$\begin{aligned} \int_{x_1}^{x_2} (x - x_2)(x - x_3) dx &= \frac{1}{3} (x_2^3 - x_1^3) - \frac{1}{2} (x_2 + x_3) (x_2^2 - x_1^2) + x_2 x_3 (x_2 - x_1) \\ &= \frac{1}{6} (x_2 - x_1)^2 (3x_3 - x_2 - 2x_1) \\ &= \frac{h_1^2}{6} (3h_2 + 2h_1) \quad (3-B6) \end{aligned}$$

By interchanging x_1 and x_2 in Eq. (3-B6), one obtains:

$$\begin{aligned} \int_{x_1}^{x_2} (x - x_1)(x - x_3) dx &= \frac{1}{6} (x_1 - x_2)^2 (3x_3 - x_1 - 2x_2) \\ &= - \frac{h_1^2}{6} (3h_2 + h_1) \quad (3-E7) \end{aligned}$$

By substituting x_3 by x_2 in Eq. (3-B7), one obtains:

$$\begin{aligned} \int_{x_1}^{x_2} (x - x_1)(x - x_2) dx &= -\frac{1}{6} (x_2 - x_1)^3 \\ &= -\frac{h_1^3}{6} \end{aligned} \quad (3-B8)$$

Therefore:

$$I_{1,2} = -\frac{h_1(3h_2 + 2h_1)}{6(h_2 + h_1)} f_1 + \frac{h_1(3h_2 + h_1)}{6h_2} f_2 - \frac{h_1^3}{6h_2(h_2 + h_1)} f_3 \quad (3-B9)$$

Furthermore, by interchanging h_2 and h_1 , and f_1 and f_3 in Eq. (3-B9), one obtains:

$$I_{2,3} = -\frac{h_2^3}{6h_1(h_2 + h_1)} f_1 + \frac{h_2(h_2 + 3h_1)}{6h_1} f_2 + \frac{h_2(2h_2 + 3h_1)}{6(h_2 + h_1)} f_3 \quad (3-B10)$$

Finally, by adding Eqs. (3-B9) and (3-B10), one obtains:

$$I_{1,3} = \frac{h_2 + h_1}{6} \left[\frac{2h_1 - h_2}{h_1} f_1 + \frac{(h_2 + h_1)^2}{h_1 h_2} f_2 + \frac{2h_2 - h_1}{h_2} f_3 \right] \quad (3-B11)$$

The error involved in the approximate integration formulae (3-B9) to (3-B11) is of the order of h^4 . For $h_1 = h_2$, formulae (3-B9) and (3-B10) reduce to the well-known formula of Adams-Moulton, while formula (3-B11) reduces to Simpson's rule.

4. CLASSICAL CALCULATIONS OF ROTATIONAL AND VIBRATIONAL EXCITATION IN ENERGETIC ATOM-DIATOMIC HYDRIDE COLLISIONS

4.1 Introduction

Since 1960, literally hundreds of calculations of inelastic energy transfer in simple atom-diatom or diatom-diatom collisions have been published. The overwhelming bulk of this work has been performed while using either the rigid rotor approximation to study only translational-rotational energy transfer or a collinear collision scheme to isolate translational-vibrational energy transfer.

Recently, a number of workers have published studies that treat the problem of coupled vibrational and rotational energy transfer in simple collisions. These efforts include the classical, two-dimensional models of Benson and Berend,⁽¹⁷⁾ Kelley and Wolfsberg,⁽¹⁸⁾ and Bergeron and Chapuisat,⁽¹⁹⁾ which aim primarily at elucidating the effects of rotational inelasticity on collisionally induced vibrational excitation or de-excitation. Semiclassical, three-dimensional treatments of this same problem have been presented recently by Wartell and Cross,⁽²⁰⁾ Stallcup⁽²¹⁾ and Sorensen.⁽²²⁾ Other studies of interest include the quantum mechanical treatment of the He-H₂ collision system by Eastes and Secrest,⁽²³⁾ which uses the He-H₂ interaction potential calculated by Gordon and Secrest,⁽²⁴⁾ and the semiclassical treatment of the Ar-H₂ system by Shin,⁽²⁵⁾ which uses an interaction potential based on molecular beam data. Doll and Miller⁽²⁶⁾ have also treated the He-H₂ problem by using classical S-matrix techniques. In addition, Thompson⁽²⁷⁾ has been able to calculate reasonable rotational and vibrational energy transfers for a number of atom-diatom systems by using Monte Carlo classical trajectory techniques and semiempirical valence-bond interaction surfaces.

The focus of the present work is the effect of vibrational inelasticity on the rotational excitation of such diatomic hydrides as HF, HCl, and OH in energetic collisions with atomic species. Classical, three-dimensional calculations of rotational excitation probabilities for both rigid and nonrigid diatomics in collisions with several atomic species are presented here, and the effect of the rigid rotor approximation is evaluated.

4.2 Interaction Potentials

The collisions of interest have center-of-mass energies in the range of 1 to 5 eV. Such interactions occur well up on the repulsive core of reasonable intermolecular potentials and are insensitive to the weaker "long-range" portions of the potentials. This insensitivity is exploited by adopting hard-sphere potentials for the colliding species. Each diatomic is modeled with two interpenetrating hard spheres, while monatomic species are represented by a single sphere. The diatomics are either held rigid along their line-of-centers at a distance between sphere centers fixed by the equilibrium ground-state internuclear distance of the hydride in question or are attached along the line-of-centers by a one-dimensional harmonic oscillator.

Sphere sizes for bound and unbound atoms are estimated from the high-energy molecular beam-scattering data of the Amdur-Jordan group at MIT or of the Leonas group at the Moscow State University. The sphere sizes selected represent the effective range of one eV potential for the species in question and are determined by methods outlined in earlier work on atom-H₂O collisions.⁽²⁸⁾

Equilibrium bond distances for the hydride molecules are taken from Herzberg,⁽²⁹⁾ and are shown in Table 4-I, along with hard-sphere radii for molecular atoms and monatomic-collision partners. Sphere radii for O, H, Ar and He are taken from Ref. (28). The F-atom radius is based on data of Belyaev, et al.,⁽³⁰⁾ which determined a potential of $V(\text{Ar-F})$ of $506/r^{9.30}$, where V is expressed in eV and r in Å. The Cl radius is estimated, since no pertinent

molecular beam data could be located. The same radius and internuclear separation is used for cases involving the isotopes ^{35}Cl and ^{37}Cl . All other atoms are assumed to have only the mass of their predominate isotope.

Table 4-I. Molecular Parameters

Molecular Atom		Hard-Sphere Radius (A)
H		0.65
O		0.88
F		0.83
Cl		1.18
Monatomic Collision Partner		Hard-Sphere Radius (A)
He		0.63
O		0.85
Ar		1.12
Diatomic	Equilibrium Bond Distance = (A)	Average Geometric Cross Section (\AA^2)
OH	0.9706	3.06
HF	0.9171	2.80
HCl	1.2746	4.92

4.3 Collision Mechanics

The choice of a hard sphere interaction potential reduces the analysis of the collision process to a study of the configuration at the moment of impact. The calculation is most conveniently performed in the precollision rest frame of the molecule. The rotational and vibrational degrees of freedom of the molecule are assumed to be initially unexcited. Thus, the configuration is fixed in an inertial frame at the collision instant.

Now consider the impact of the collision partners q with the molecular atoms denoted by the subscripts 1 and 2 (Fig. 4-1). The conservation of momentum, angular momentum, and energy are given respectively by

$$m_q \underline{v}_q = m_q \underline{v}'_q + m_1 \underline{v}'_1 + m_2 \underline{v}'_2 \quad (4-1)$$

$$m_q \underline{r}_q \times \underline{v}_q = m_q \underline{r}_q \times \underline{v}'_q + m_1 \underline{r}_1 \times \underline{v}'_1 + m_2 \underline{r}_2 \times \underline{v}'_2 \quad (4-2)$$

$$\frac{1}{2} m_q v_q^2 = \frac{1}{2} m_q v_q'^2 = \frac{1}{2} m_1 v_1'^2 + \frac{1}{2} m_2 v_2'^2 \quad (4-3)$$

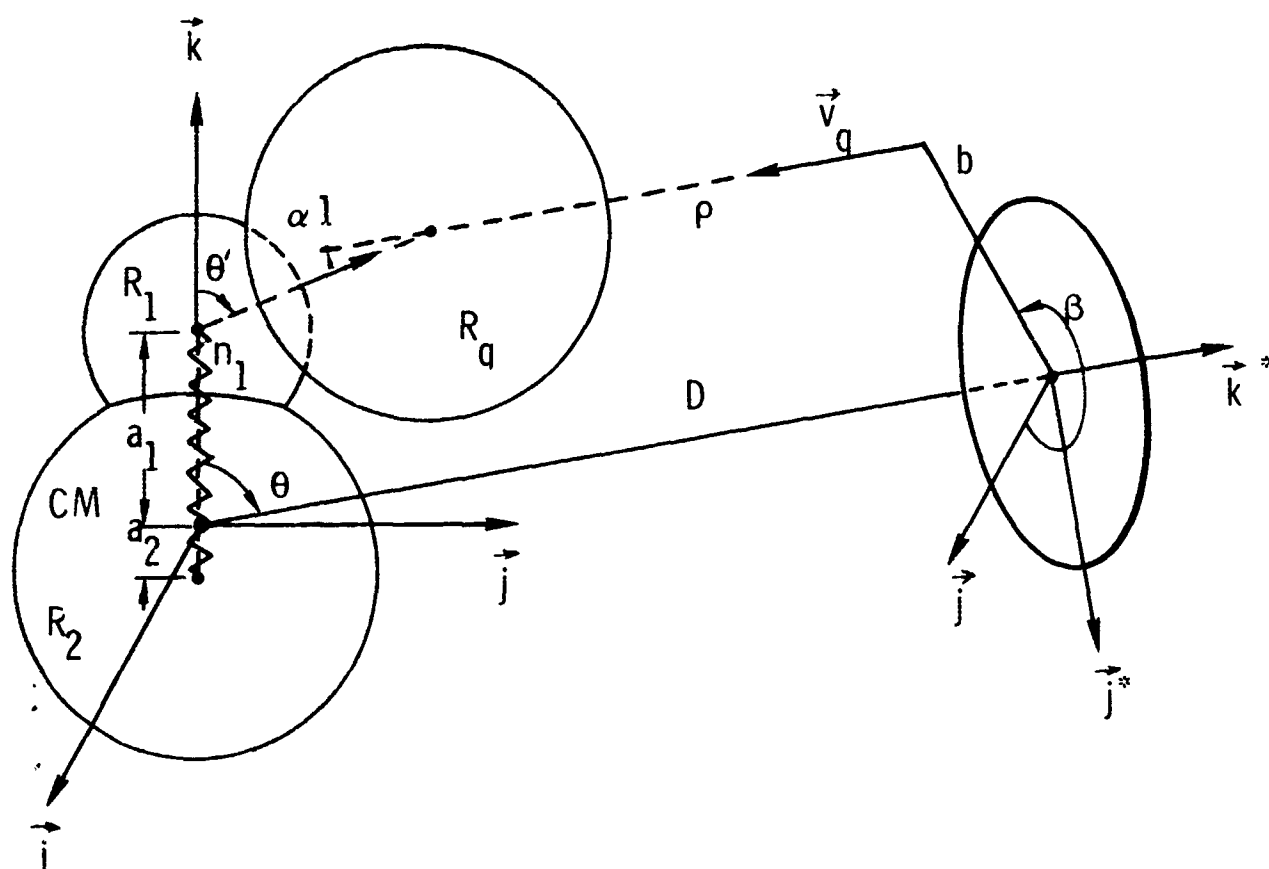


Figure 4.1 - Coordinate systems used to describe collision.

The primed quantities denote post collision values of the atom velocities \underline{v}'_{α} ($\alpha = 1, 2, q$), while \underline{r}_{α} denotes the position of the center-of-mass of the α atom with respect to the center-of-mass of the molecule at the instant of collision.

In order to proceed further, it is necessary to consider the relationship between the hard-sphere model and a continuous molecular interaction potential $\phi(\underline{r})$ of the form

$$\phi(\underline{r}) = \phi_1(\underline{r}_{1q}) + \phi_2(\underline{r}_{2q}) + \frac{1}{2} \mu_{12} \omega^2 \xi^2, \quad (4-4)$$

$$r_{\alpha q} = |\underline{r}_{\alpha} - \underline{r}_q|, \quad \alpha = 1, 2. \quad (4-5)$$

Here μ_{12} is the reduced mass of the molecular atoms, ω is the frequency of vibration, and ξ is the amount by which the distance between the molecular atoms has departed from its equilibrium value (the "spring" deflection). For collisions sufficiently energetic to penetrate well up on the repulsive core of either atomic potential, $\phi_{\alpha}(r_{\alpha q})$, the local length, ℓ , over which the interaction occurs may be characterized by

$$\ell \sim \phi_{\alpha} \left(\frac{\partial \phi_{\alpha}}{\partial r_{\alpha q}} \right)^{-1} (r_{\alpha q} = r_0). \quad (4-6)$$

The radius, r_0 , is chosen so that $\phi_{\alpha}(r_0)$ is in the interaction energy range under consideration. ⁽²⁸⁾ The interaction time, τ , is approximately

$$\tau \sim \frac{2\ell}{|\underline{v}_q|}. \quad (4-7)$$

The hard-sphere model may be regarded as the limiting form of $\phi(r)$ as ℓ/r_0 approaches zero, provided that two further conditions are satisfied. First, the rotational excitation must be such that $|\underline{\Omega}| \tau \ll 1$. The angular velocity $\underline{\Omega}$ is defined so that the impulsively generated angular momentum of the molecule about its center of mass is $I\underline{\Omega}$, where I is the moment of inertia. Under these conditions, the magnitude of the impulse W transmitted to the collision partner q is directed along the line connecting the centers of the two colliding atoms. Thus,

$$m_q (\underline{v}_q - \underline{v}_q) = \underline{n}_1 W \quad (4-8)$$

where \underline{n}_1 is the unit normal to the molecular atom.

The manner in which the impulse, $\underline{n}_1 W$, is divided between the molecular atoms is determined from the final condition that must be satisfied for the hard-sphere model to be employed. If the frequency of the vibration is sufficiently low so that $\omega\tau \ll 1$, then the impulse is transmitted before the "spring" can deform.⁽³¹⁾ Since the impulse must be transmitted to the second molecular atom via the vibrational mode, the instantaneous post-collision state of the molecule must be such that the molecular atom experiencing the impact absorbs the component of the impulse directed along the spring axis, \underline{k} . (See Fig. 4-1.)

$$-\underline{n}_1 \underline{k} W = m_1 \underline{v}_1 \cdot \underline{k} \quad (4-9)$$

If, on the other hand, the vibrational frequency is sufficiently high so that $\omega\tau \gg 1$, then the molecule will behave like a rigid rotor, and Eq. (4-3) must be replaced by the condition⁽³¹⁾

$$\xi(t) = 0 \quad (4-10)$$

When $\omega\tau$ is neither large nor small, the use of the hard-sphere model cannot be justified on the basis of classical mechanics. However, in order to apply the classical approximation to a molecule containing a vibrational degree of freedom, the classically computed vibrational excitation must be much larger than the energy $\hbar\omega$ needed to excite that degree of freedom. When this is not the case, the rigid rotor assumption [Eq. (4-4)] may still provide a useful approximation to the rotational excitation, even though the condition $\omega\tau \ll 1$ is not satisfied. This point is discussed further in Sec. 4.7.

The system of Eqs. (4-1) through (4-4) is now used to determine the excitation of the internal degrees of freedom in a single collision for both the rigid rotor ($\omega\tau \gg 1$) and the harmonic oscillator model ($\omega\tau \ll 1$). To this end, it is convenient to replace the molecular velocities, \underline{v}'_α , by a center-of-mass velocity, \underline{v}_{CM} , an angular velocity, $\underline{\Omega}$, and a spring deflection velocity, $w^*\underline{k}$. These quantities are defined by the conditions

$$(m_1 + m_2) \underline{v}_{CM} = m_1 \underline{v}'_1 + m_2 \underline{v}'_2 \quad , \quad (4-11)$$

$$\underline{\Omega} = m_1 \underline{a}_1 \underline{k} \times \underline{v}'_1 - m_2 \underline{a}_2 \underline{k} \times \underline{v}'_2 \quad . \quad (4-12)$$

$$(\underline{v}'_1 - \underline{v}'_2) \cdot \underline{k} = w^* \quad , \quad (4-13)$$

thus,

$$\underline{v}'_1 = \underline{v}_{CM} + \underline{\Omega} \times \underline{a}_1 \underline{k} + \frac{m_2 w^*}{m_1 + m_2} \underline{k} \quad , \quad (4-14)$$

$$\underline{v}'_2 = \underline{v}_{CM} - \underline{\Omega} \times \underline{a}_2 \underline{k} - \frac{m_1 w^*}{m_1 + m_2} \underline{k} \quad . \quad (4-15)$$

By substituting Eqs. (4-14) and (4-15) into Eqs. (4-1) through (4-3), the conservation laws take the form

$$(m_1 + m_2) \underline{v}_{CM} = m_q (\underline{v}_q - \underline{v}'_q) \quad (4-16)$$

$$m_q \underline{r}_q \times (\underline{v}_q - \underline{v}'_q) = I \underline{\Omega} \quad , \quad (4-17)$$

$$\frac{1}{2} m_q v_q^2 = \frac{1}{2} m_q v_q'^2 + \frac{1}{2} (m_1 + m_2) v_{CM}^2 + \frac{1}{2} I \Omega^2 + \frac{1}{2} \mu_{12} w^{2*} \quad . \quad (4-18)$$

Equations (4-2) and (4-6), together with the expression

$$-\underline{n}_1 W \cdot \underline{k} = m_1 \underline{v}_{CM} \cdot \underline{k} + \mu_{12} w^* \quad (4-19)$$

for the oscillator model, and the condition

$$w^* = 0 \quad (4-20)$$

for the rigid rotor model, constitute the formulation of the problem.

The above system of equations is readily solved by using Eq. (4-8) to eliminate \underline{v}'_q from Eqs. (4-16) and (4-19). Thus, \underline{v}_{CM} , $\underline{\Omega}$, and w^* can be expressed as functions of the impulse W as

$$\underline{v}_{CM} = - \frac{\underline{n}_1 W}{m_1 + m_2} \quad , \quad (4-21)$$

$$\underline{\Omega} = - \frac{(\underline{r}_q \times \underline{n}_1) W}{I} \quad , \quad (4-22)$$

$$w^* = - \frac{(\underline{n}_1 \cdot \underline{k}) W}{m_1} \quad . \quad (4-23)$$

The last equation is replaced by $w^* = 0$ for the rigid rotor model. Substitution of Eq. (4-22) into the energy conservation equation yields the following results for W by using the harmonic oscillator model

$$W = \frac{2v_g \cdot n_1}{\left[(\mu_{qD})^{-1} + \left(\frac{n_1 \cdot k}{m_1} \right)^2 \mu_{12} + \frac{(r_q \times n_1)^2}{I} \right]}, \quad (4-24)$$

where

$$r_q = a_1 k + (R_1 + R_q) n_1$$

and

$$\mu_{qD} = \frac{m_D m_q}{m_D + m_q}, \quad m_D = m_1 + m_2.$$

Here, R_1 and R_q are, respectively, the hard-sphere radii for the molecular atom experiencing the collision and the collision partner. The corresponding expression for the rigid-rotor model is

$$W = \frac{2v_g \cdot n_1}{\left[(\mu_{qD})^{-1} + \frac{(r_q \times n_1)^2}{I} \right]}. \quad (4-25)$$

Expressions (4-21) through (4-25) constitute the required solution. Ignoring those incident configurations that lead to multiple impacts (e.g., certain col-linear collisions) as statistically unimportant compared with those that do not,

the rotational and vibrational excitation energies experienced in an individual collision are given by

$$E_V = \frac{1}{2} \mu_{12} w^{*2} \quad , \quad (4-26)$$

$$E_R = \frac{1}{2} I \Omega^2 \quad . \quad (4-27)$$

These expressions follow immediately from the assumption that the deformation ξ is small compared with $a_1 + a_2$, so that the post collision oscillations can be expressed in terms of a Lagrangian, L_V , of the form

$$L_V = \frac{1}{2} \mu_{12} (w^*)^2 - \frac{1}{2} \mu_{12} \omega^2 \xi^2 \quad . \quad (4-28)$$

The modification of these results because of the presence of a steep, continuous potential of the type considered above could be calculated, in principle, using multi-time scale perturbation techniques. For example, such a calculation could be employed to determine the effect of a slow rotation or vibration of the molecule about the center of mass on the trajectory of the collision partner as it passed through the potential, $\phi_\alpha(r_{\alpha q})$, of one of the molecular atoms. The rotational and vibrational excitation would be altered by an amount of the order of $|\Omega|\tau$ by this phenomenon, which would permit vibrational excitation of this magnitude to occur even for collisions perpendicular to the molecular axis.

Similar procedures could be employed when the vibrational period is much smaller than the interaction time. However, it is not clear that such elaborate, classical calculations of vibrational effects should be performed until it is evident that a classical description of this channel is appropriate.

4.4 Kinematics and Probability Model

The colliding atom is assumed to be drawn from a uniform beam of such atoms with common velocity vector \underline{v}_q . The diatomic molecule is assumed to have a random orientation with respect to its center-of-mass at the time of impact. In what follows, the $(\underline{i}, \underline{j}, \underline{k})$ coordinate system is fixed in the molecule with origin at the center-of-mass and the axis-of-symmetry in the z -direction (see Fig. 4-1), so that the beam is viewed as randomly oriented. By symmetry, \underline{v}_q can be assumed to lie in the y - z plane for all collisions, making an angle θ with the z axis, with differential probability density, $\sin \theta d\theta$. The location of the collision partner's center prior to impact is given by the impact parameter b and an angle β , which are polar coordinates in a plane orthogonal to \underline{v}_q . Since this distribution is uniform, the differential probability density is $b db d\beta$. The third location parameter, D , the initial distance apart, is, of course, arbitrary. A second coordinate system $(\underline{i}^*, \underline{j}^*, \underline{k}^*)$, centered in the colliding atom, is defined by rotation

$$\underline{i}^* = \underline{i}, \quad \underline{j}^* = \underline{j} \cos \theta - \underline{k} \sin \theta, \quad \underline{k}^* = \underline{j} \sin \theta + \underline{k} \cos \theta, \quad (4-29)$$

so that the beam axis is \underline{k}^* . It follows that the initial location of the atomic center is

$$\begin{aligned} \underline{p} &= D \underline{k}^* + b (\cos \beta \underline{i}^* + \sin \beta \underline{j}^*) \\ &= (D \sin \theta + b \sin \beta \cos \theta) \underline{j} + (b \cos \beta) \underline{i} \\ &\quad + (D \cos \theta - b \sin \beta \sin \theta) \underline{k}. \end{aligned} \quad (4-30)$$

The point of impact with one of the molecular atoms (say atom 1) is determined next. Let the vector between atomic centers initially be $\underline{c} = \underline{p} - a_1 \underline{k}$. At the time of impact, the colliding atom has traveled a distance ρ in the

direction $-\underline{k}^*$. Let the final vector between centers be $(R_1 + R_q)\underline{n}'$, where \underline{n}' is a unit vector relative to atom 1. It follows that

$$(R_1 + R_q)\underline{n}' = \underline{c} - \rho \underline{k}^* \quad , \quad (4-31)$$

which defines both ρ and \underline{n}' . The local angles θ' and α' are found from $\cos \theta' = \underline{n}' \cdot \underline{k}$ and $\cos \alpha' = \underline{n}' \cdot \underline{k}^*$. The solution to these equations yields

$$\sin \alpha' = \sqrt{(a_1 \sin \theta + b \sin \beta)^2 + (b \cos \beta)^2} / (R_1 + R_q) \quad , \quad (4-32)$$

$$\rho = D - a_1 \cos \theta - (R_1 + R_q) \cos \alpha' \quad , \quad (4-33)$$

$$\cos \theta' = \cos \theta \cos \alpha' - \sin \theta (a_1 \sin \theta + b \sin \beta) / (R_1 + R_q) \quad . \quad (4-34)$$

where, if the r.h.s. of the first equation is greater than unity, there is no collision. In the case of impact with atom 2, one must replace R_1 by R_2 , and a_1 by $-a_2$.

Finally, let ρ_1, ρ_2 denote the distance ρ from impact with atom 1 and atom 2, respectively. Then, the actual impact will occur on atom 1 if $\rho_1 < \rho_2$, and on atom 2 otherwise (which choice is independent of D). Also, given the angles θ and β , a maximum feasible impact parameter, b_{\max} , is obtained by setting $\sin \alpha' = 1$.

4.5 Calculation of Rotational and Vibrational Energy Distributions

For each collision, the rotational and vibrational energies are given by Eqs. (4-26) and (4-27), where for the rigid rotor, $E_V = 0$. In the following treatment, these energies are normalized by the center-of-mass energy,

$E_{CM} = 1/2 \mu_{qD} v_q^2$. Assuming for definiteness that the impact occurs on atom 1, in the vibrational case the formulas simplify to

$$E_R^V/E_{CM} = E_1 \sin^2 \theta' \cos^2 \alpha', \quad E_V^V/E_{CM} = E_1 \cos^2 \theta' \cos^2 \alpha'. \quad (4-35)$$

Thus, the maximum energies, E_R and E_V , occur for normal collisions at $\theta' = \pi/2$ and $\theta' = 0$, respectively. The maximum normalized value in either case is

$$E_1 = 4 \frac{\mu_{qD} \mu_{12}}{m_1^2} \left(1 + \frac{\mu_{qD} \mu_{12}}{m_1^2} \right)^{-2}, \quad (4-36)$$

which is a function of the masses only and never exceeds unity. It is also easily seen that E_1 is larger than E_2 (corresponding to impact on the heavier atom 2).

In the rigid rotor case, the formula (for atom 1) becomes

$$E_R^r/E_{CM} = 4 \frac{\mu_{qD} \mu_{12}}{m_1^2} \left(1 + \frac{\mu_{qD} \mu_{12}}{m_1^2} \sin^2 \theta' \right)^{-2} \sin^2 \theta' \cos^2 \alpha'. \quad (4-37)$$

In this case, the maximum normalized energy is a function of θ' , as well as the masses, and attains the value unity for a normal collision with

$$\sin^2 \theta' = \frac{m_1}{m_q} \left(1 + \frac{m_1 + m_q}{m_2} \right), \quad (4-38)$$

(if, and only if, the r.h.s. is less than unity).

This condition is equivalent to $\mu_{qD} a_1^2 \geq I$, and, if violated, the maximum value is identical to the vibrational case (namely, E_1 at $\theta' = \pi/2$). Again, impact on the heavier atom clearly leads to higher energies.

The probability distributions for the normalized energies are computed by a Monte Carlo technique for each of the collision pairs in Table 4-I, and for both the rigid rotor and vibrational models. Pseudorandom numbers are used to generate sample collisions with the collision parameters (θ , β , b) drawn from a probability density with differential

$$b \sin \theta \, d\theta \, db \, d\beta \quad . \quad (4-39)$$

This amounts to generating uniform random variables ($\cos \theta$, β , b^2) and determining the local collision angles (θ' , α') or (θ'' , α'') by the formulas of the previous section. By considering symmetry and realizability, the collision parameters are restricted to the intervals $0 \leq \theta \leq \pi$, $\theta \leq \beta \leq \pi$, and $0 \leq b \leq b_{\max}(\theta, \beta)$.

From the sample collisions, a frequency histogram of E/E_{CM} is constructed for each of the three energies, E_R^r , E_R^v , and E_V^v . This histogram is converted to an approximate probability density $P(x)$ by the definition

$$P(x) = \text{prob} \left\{ x_i \leq E/E_{CM} \leq x_i + \Delta x \right\} / \Delta x \quad , \quad (4-40)$$

for $x_i \leq x < x_i + \Delta x$. In all cases, 20 subintervals are used on the interval $0 < E/E_{CM} \leq (E/E_{CM})_{\max}$, so that $\Delta x = 0.05 E_1$ for the vibrational model, and $\Delta x = 0.05$ for the rigid model. The total number of sample points used is 50,000. The results are displayed in Figs. 4-2 through 4-10.

Figures 4.2 through 4.10 - Normalized probability distributions for the inelastic excitation of the diatomic hydrides OH, HF, and HCl in collisions with He, O, and Ar. Solid histogram represents E_V^V/E_{CM} , and dashed-dotted histogram, E_R^V/E_{CM} , for the harmonic oscillator-atom collisions. Dashed histogram represents E_R^R/E_{CM} for rigid-rotor-atom collisions. Specific sets of collision partners are indicated for each figure.

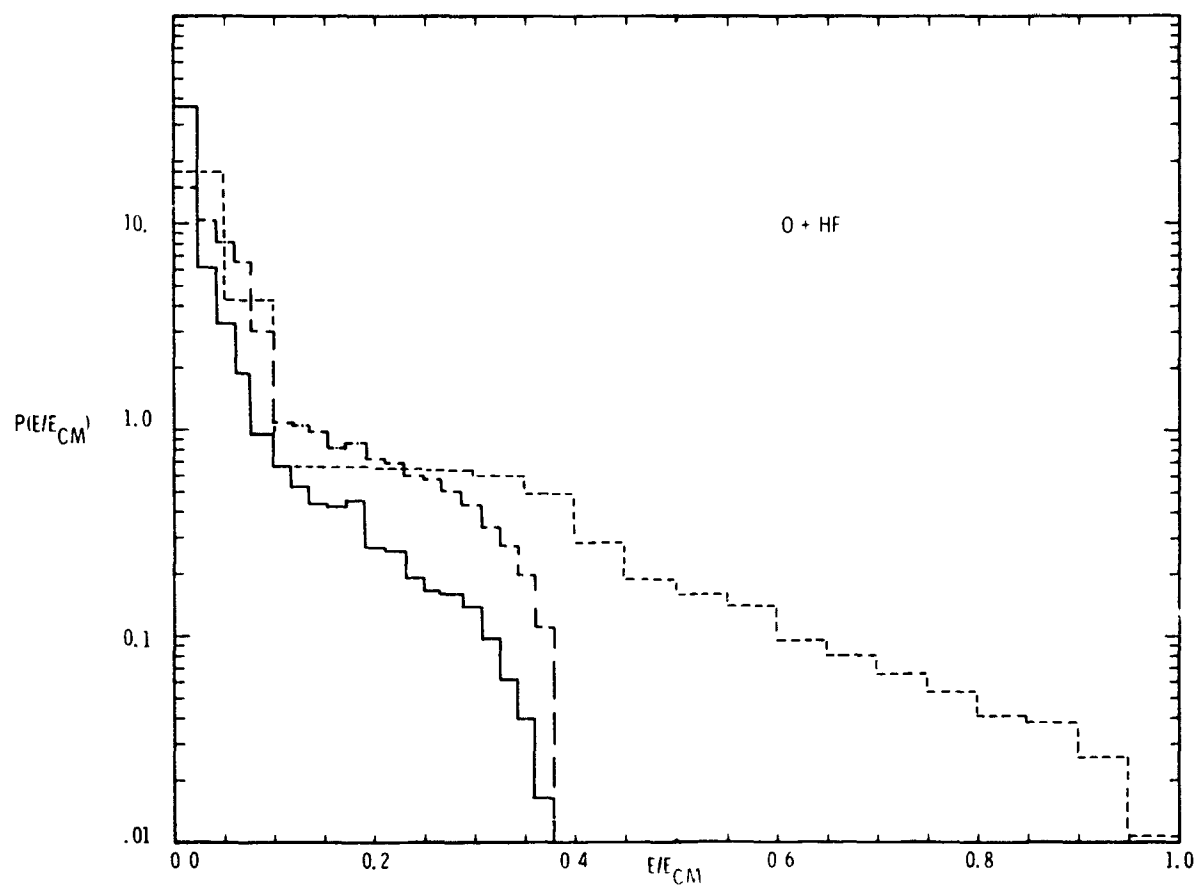


Figure 4.2 - O + HF

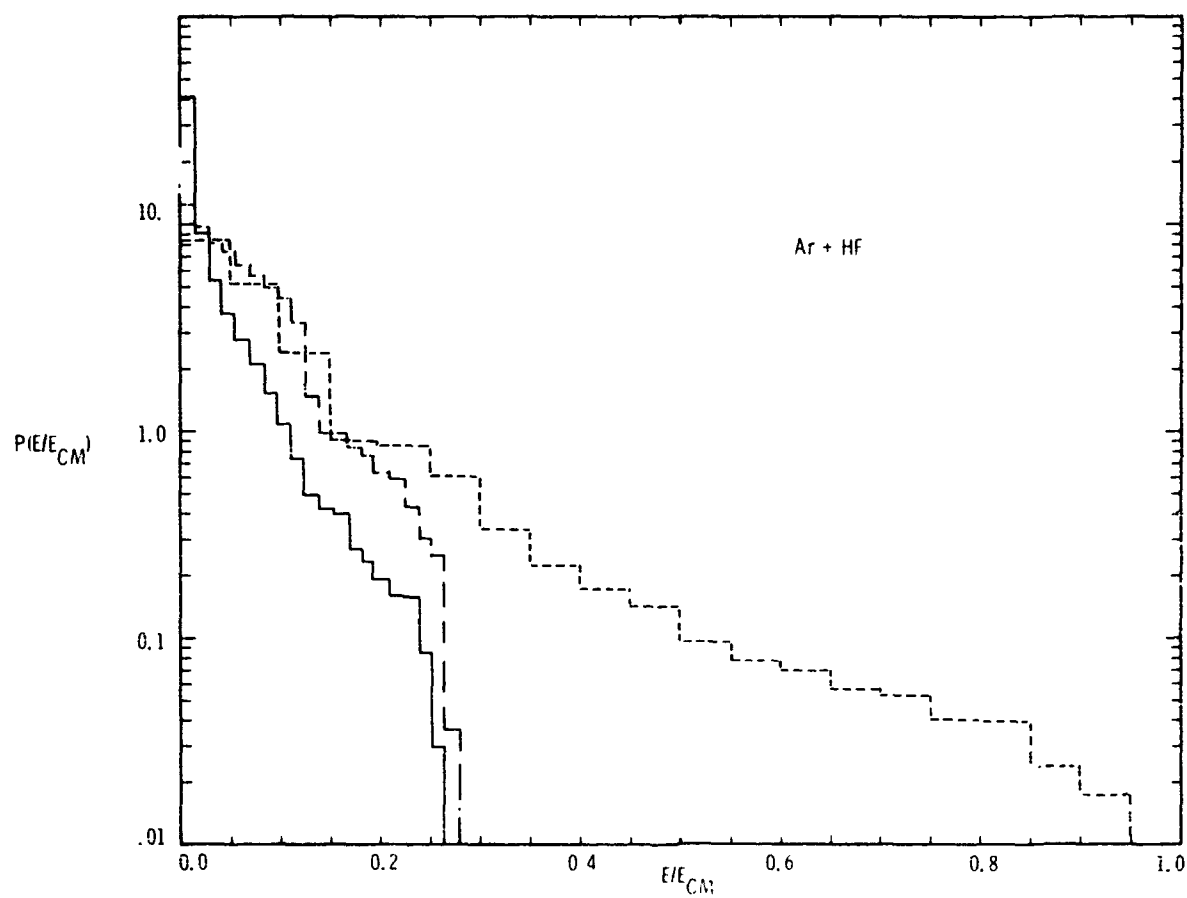


Figure 4.3 - Ar + HF.

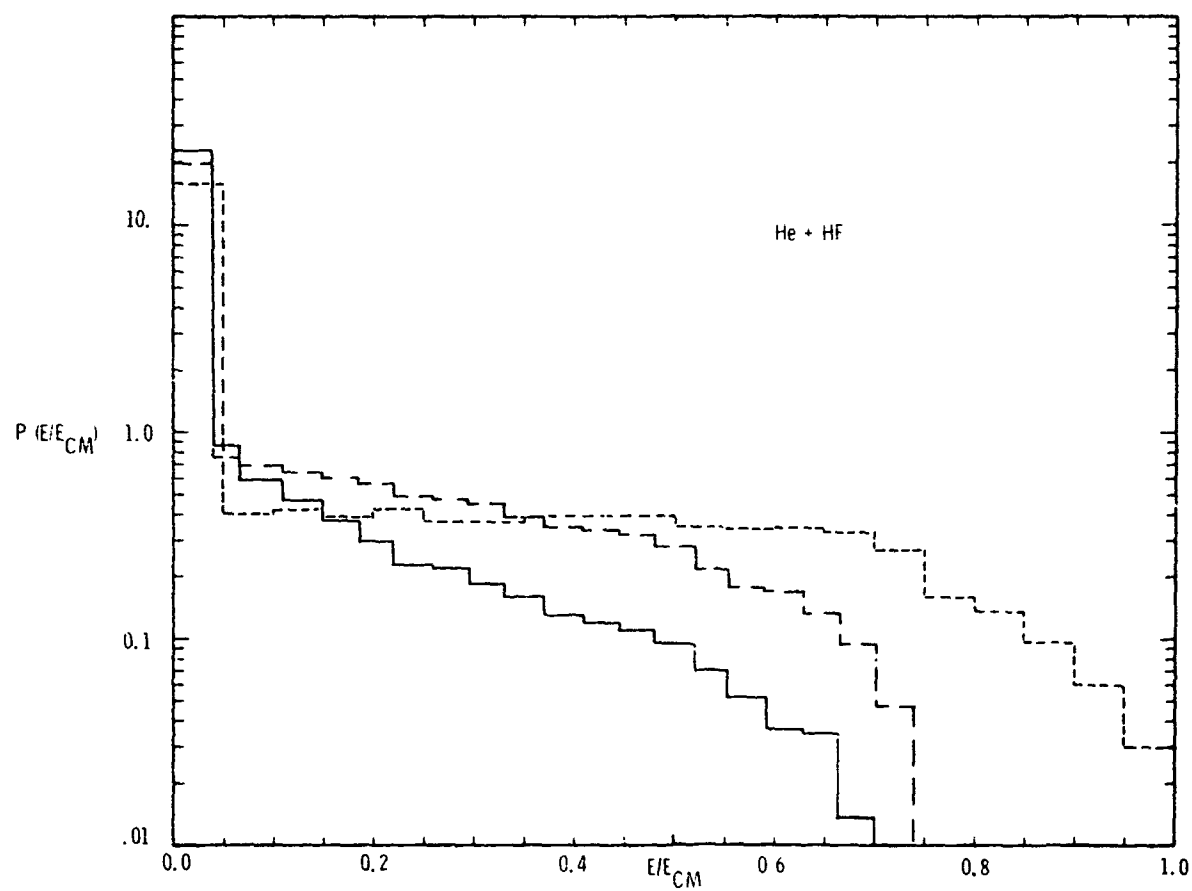


Figure 4.4 - He + HF.

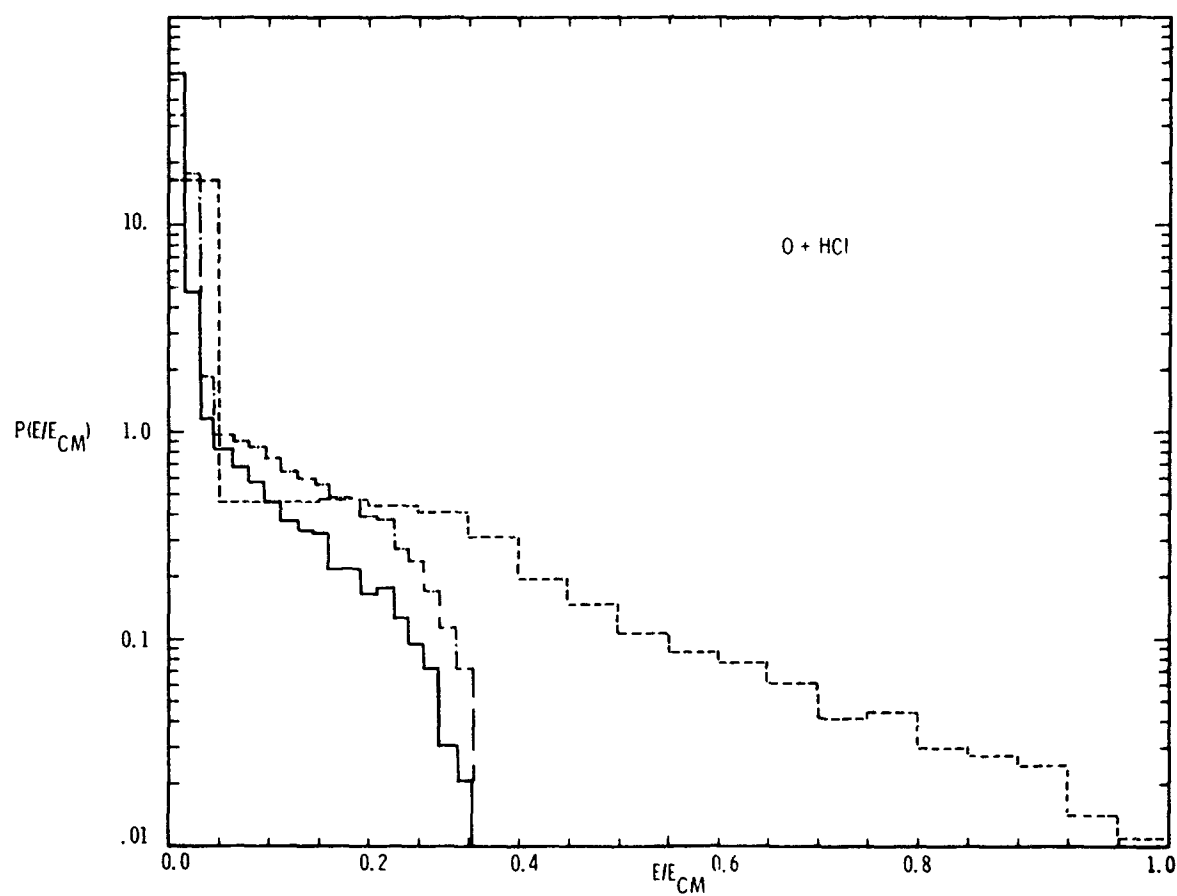


Figure 4.5 - $O + HCl$.

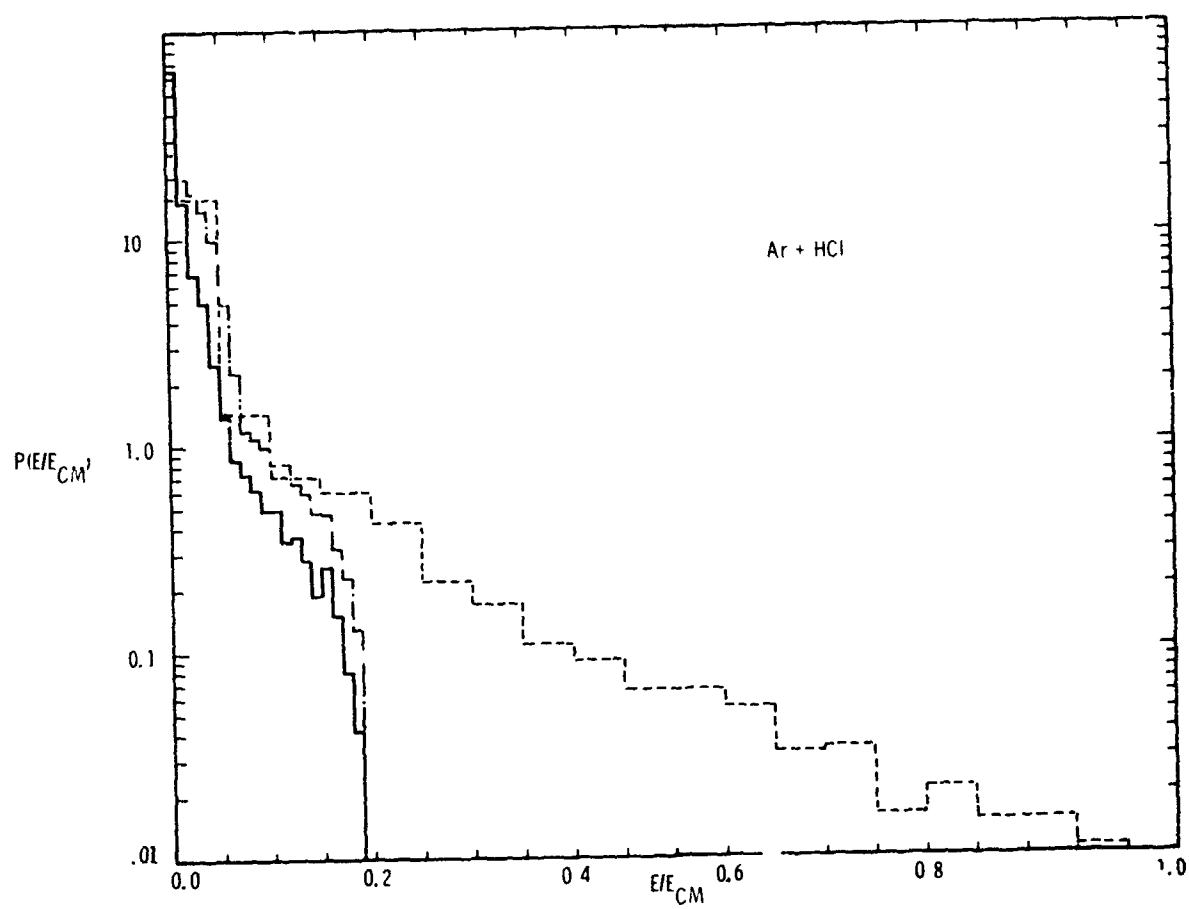


Figure 4.6 - Ar + HCl.

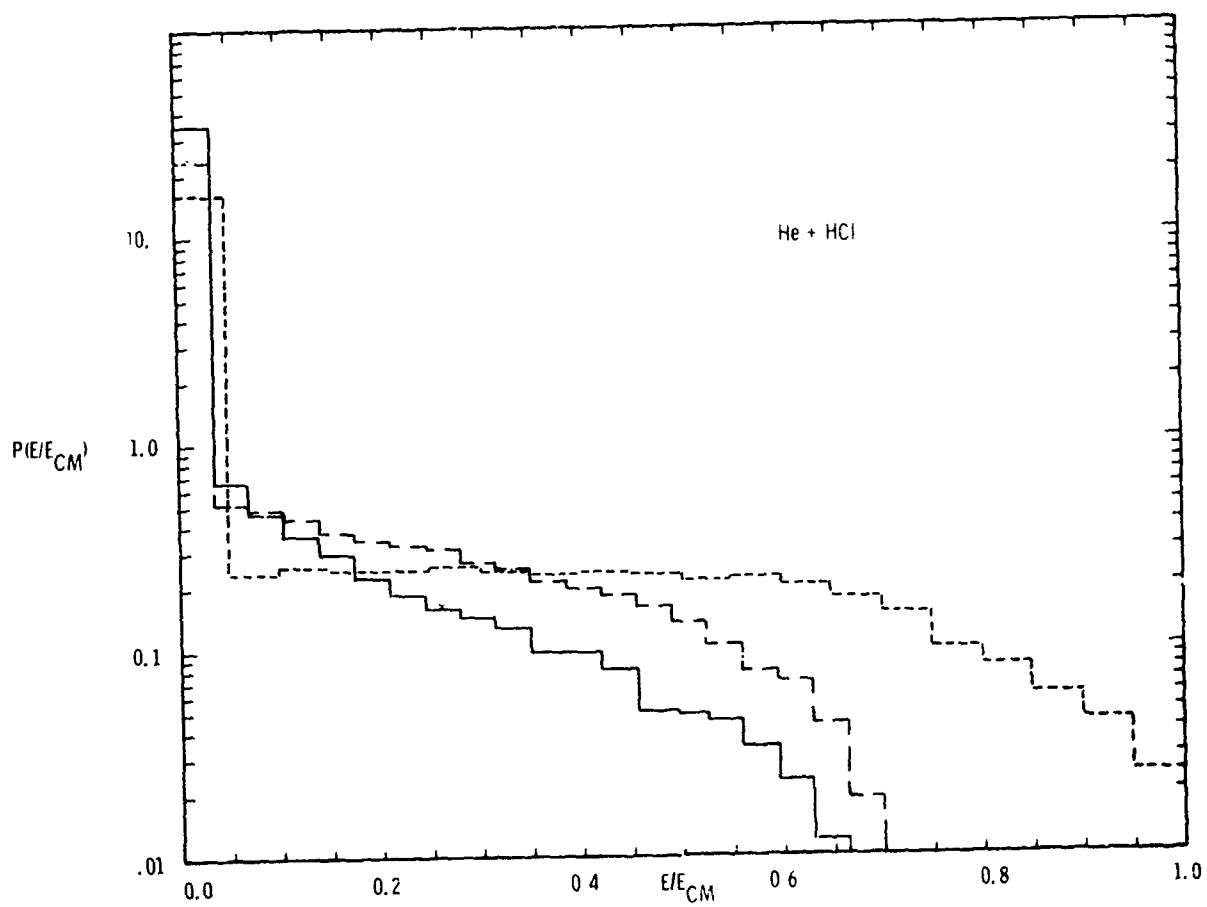


Figure 4.7 - He + HCl.

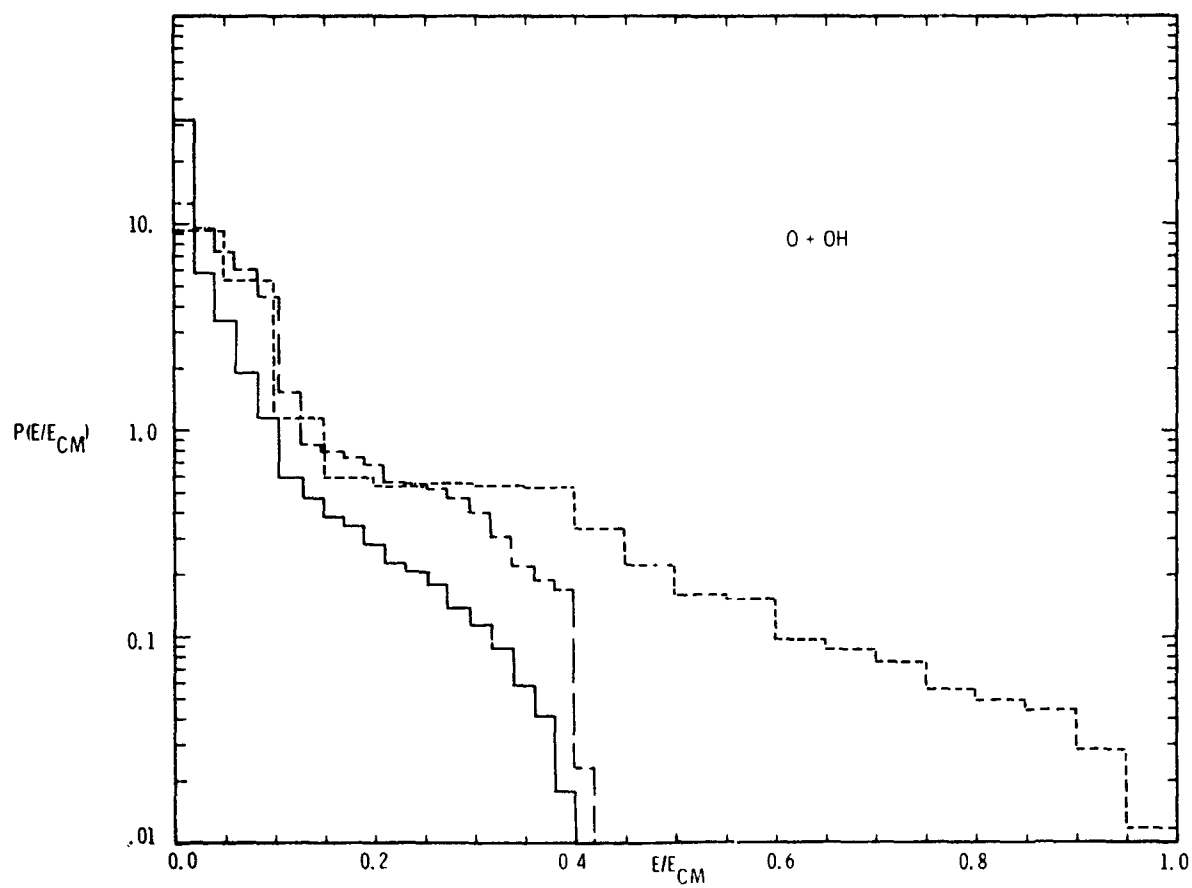


Figure 4.8 - O + OH.

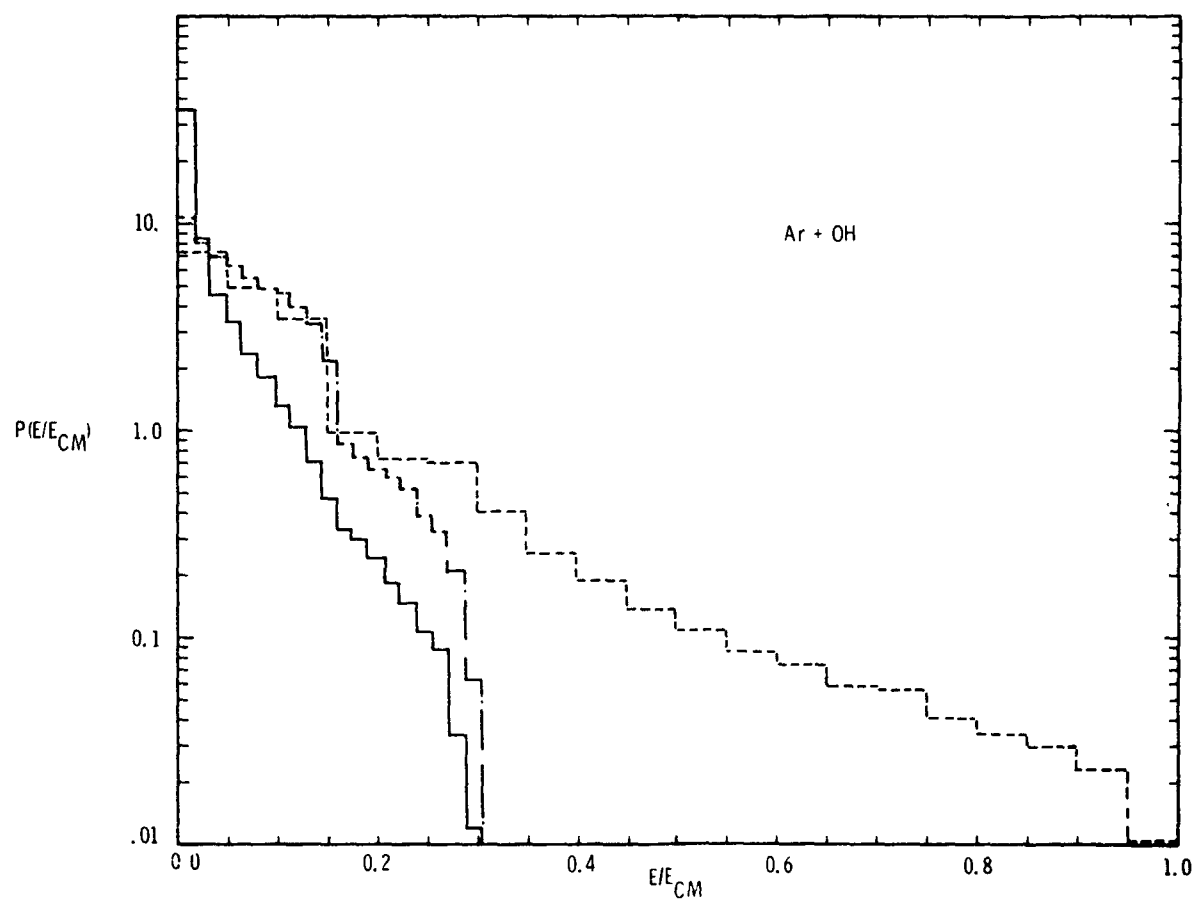


Figure 4.9 - Ar + OH.

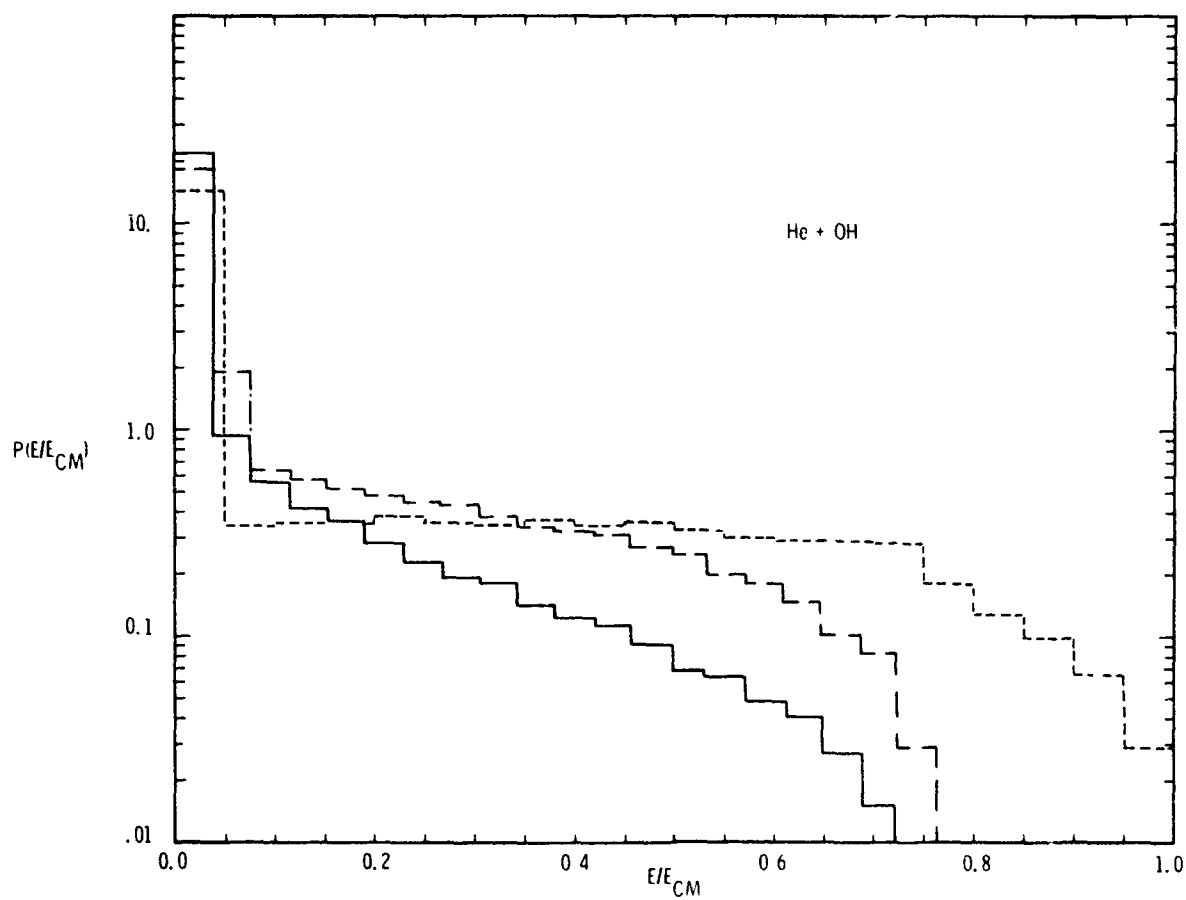


Figure 4.10 - He + OH.

Separate runs were made for atomic collisions with $H^{35}Cl$ and $H^{37}Cl$. However, the probability distributions showed virtually no isotope effect, and only the results for $H^{35}Cl$ are displayed. Table 4-II gives the sample means in the following format. The top number for each collision pair represents the

Table 4-II. Normalized Mean Excitations

Diatomic	Atom	He	O	Ar
OH	E_R^F/E_{CM}	0.127	0.112	0.113
	E_R^V/E_{CM}	0.083	0.069	0.072
	E_{rr}^V/E_{CM}	0.036	0.029	0.029
	p_1	0.283	0.296	0.309
HF	E_R^F/E_{CM}	0.127	0.106	0.103
	E_R^V/E_{CM}	0.083	0.063	0.062
	E_V^V/E_{CM}	0.035	0.026	0.025
	p_1	0.300	0.319	0.329
HCl	E_R^r/E_{CM}	0.077	0.059	0.055
	E_R^V/E_{CM}	0.044	0.029	0.030
	E_V^V/E_{CM}	0.023	0.015	0.014
	p_1	0.186	0.195	0.210

mean fraction of the center-of-mass collision energy which the rigid rotor-atom collision imparts to the diatomic's rotational modes (E_R^V/E_{CM}). The second number for each pair is the mean fraction imparted to the rotational modes in the harmonic oscillator-atom collision (E_R^V/E_{CM}). The third number represents the mean fractional energy in the vibrational mode for the harmonic oscillator-atom collisions (E_V^V/E_{CM}). The sample probability p_1 of impacting on atom 1 (the H atom) rather than atom 2 is also shown as the fourth number. Estimates of the maximum relative error in the plotted values of $P(x)$ can be made by using a normal approximation to the multinomial distribution for a histogram. These estimates typically range from 2% for $P(0)$ to 100% for $P(E_{max})$. The relative errors in the means and p_1 are all within 2%.

4.6 An Approximate Distribution for the Vibrational Model

The simplicity of the energy expressions in the vibrational case leads naturally to an approximate analytic expression for $P(x)$ which is quite accurate. First, assume that the probabilities p_1 , p_2 of impacting atom 1 or atom 2, respectively, have been accurately estimated by Monte Carlo methods, and then restrict attention to, say, atom 1. The probability distributions for the random variables (θ', α') are derived from those for (θ, b, β) , and then transformed analytically to obtain the distributions for the energies. However, to make the transformation tractable, a certain geometric approximation is introduced.

From physical considerations, one expects the distribution of hits on the surface of atom 1 to be random; that is, $\cos \theta'$ is uniformly distributed. This conjecture is verified both by simulation and manipulation of the equations of transformation. Similarly, inspection of the equation for $\sin^2 \alpha'$ leads to the conclusion that it (and hence $\cos^2 \alpha'$) is also uniformly distributed independently of θ' .

Both these results ignore the effects of shielding by atom 2 on some trajectories that would otherwise impact atom 1. Such shielding is of two types (see Fig. 4-11). In the first type (total shielding), a range of angles $\theta'_K < \theta' \leq \pi$ is totally inaccessible. In the second type (partial shielding), for a range of angles $\theta'_T < \theta' \leq \theta'_K$ the probability of impact is reduced, and the distribution of α' depends on θ' . For $0 \leq \theta' \leq \theta'_T$ atom 2 has no effect. The approximation made is to ignore partial shielding, while taking account of total shielding. The formula for θ'_K is easily obtained from the geometry,

$$-\cos \theta'_K = \left[- (R_2 + R_q)^2 + (a_1 + a_2)^2 + (R_1 + R_2)^2 \right] \left[2 (a_1 + a_2) (R_1 + R_q) \right]^{-1}. \quad (4-41)$$

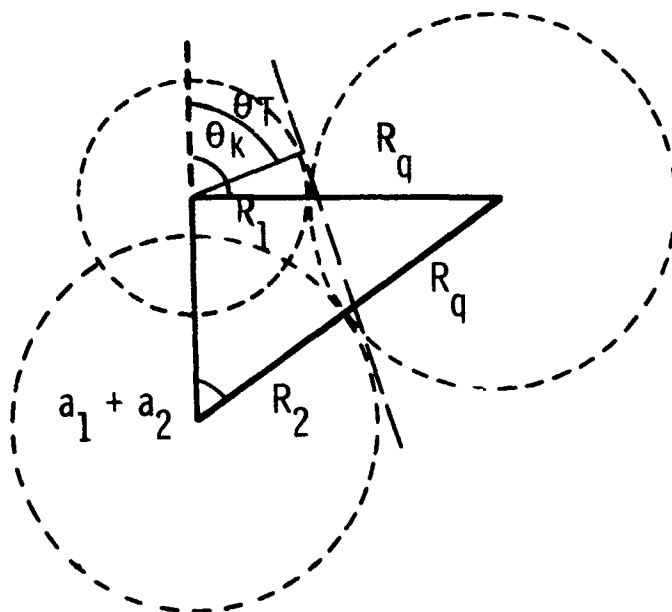


Figure 4.11 - Definition of the angles θ'_K and θ'_T .

Now, still restricting attention to atom 1, let

$$y_1 = \left(E_V^V / E_{CM} \right) / E_1 , \quad y_2 = \left(E_R^V / E_{CM} \right) / E_1 , \quad (4-42)$$

$$x_1 = \cos^2 \alpha' , \quad x_2 = \cos \theta' . \quad (4-43)$$

Then,

$$y_1 = x_1 x_2^2 , \quad y_2 = x_1 \left(1 - x_2^2 \right) .$$

and (x_1, x_2) are uniform random variables with ranges $0 \leq x_1 \leq 1$ and $-\delta_1 \equiv \cos \theta'_K \leq x_2 \leq 1$. (Note: $\theta'_K < \pi/2$ for the collision pairs considered.)

It is now straightforward to derive the distribution of (y_1, y_2) . Using the Jacobian of the transformation $J = 2x_1x_2$, the joint distribution is found to be

$$\frac{1}{1 + \delta_1} dx_1 dx_2 = \frac{1}{2(1 + \delta_1)} \left[y_1 (y_1 + y_2) \right]^{-1/2} dy_1 dy_2 , \quad (4-44)$$

from which the marginal distributions for y_1 and y_2 are obtained by integration. Denote the joint density function by $f(y_1, y_2)$. In order to do the integrations, it is necessary to specify the region of admissible (y_1, y_2) [outside of which $f(y_1, y_2) \equiv 0$]. Since the Jacobian, J , equals zero along the line $x_2 = 0$, the integrals must be calculated separately over different regions, according to the sign of x_2 . By using the bounds on (x_1, x_2) , these regions are R_1 and R_2 , as indicated in Fig. 4-12; i.e.,

$$\int_{R_1} \int_{R_2} f(y_1, y_2) dy_1 dy_2 = 1 . \quad (4-45)$$

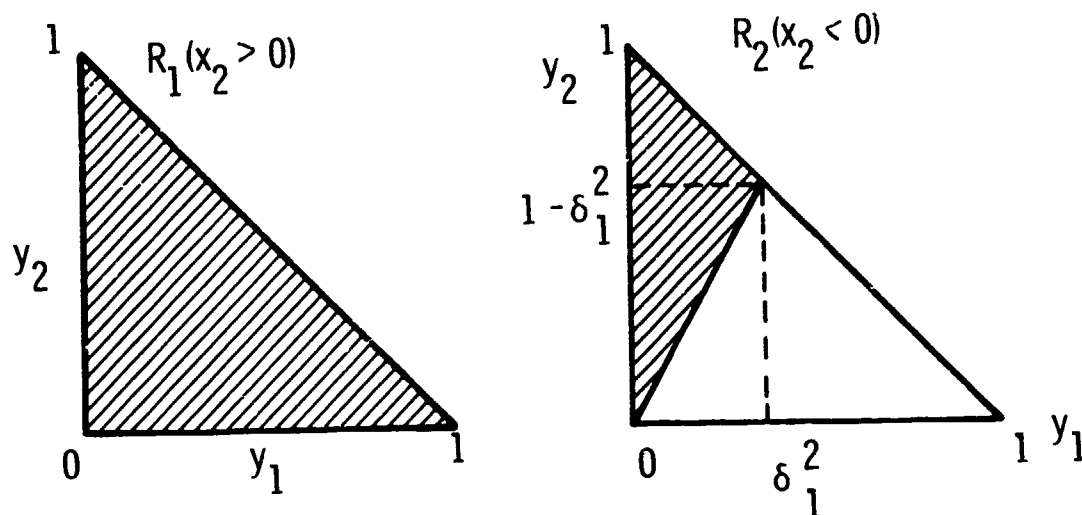


Figure 4.12 - Regions of integration in the y_1, y_2 plane.

Finally, the marginal distributions are obtained as follows:

$$f_1(y_1, \delta_1) = \begin{cases} \int_0^{1-y_1} f(y_1, y_2) dy_2 = \frac{1}{1+\delta_1} \left(y_1^{-1/2} - 1 \right), & \text{if } y_1 \geq \delta_1^2 \\ \int_0^{1-y_1} + \int_{[(1-\delta_1^2)/\delta_1^2]y_1}^{1-y_1} f(y_1, y_2) dy_2 = \frac{1}{1+\delta_1} \left(2y_1^{-1/2} - \frac{1}{\delta_1} - 1 \right), & \text{if } y_1 \leq \delta_1^2 \end{cases}$$

(4-46)

$$f_2(y_2, \delta_1) = \begin{cases} 2 \int_0^{1-y_2} f(y_1, y_2) dy_1 = \frac{2}{1+\delta_1} \cosh^{-1} \left(y_2^{-1/2} \right), & \text{if } y_2 \geq 1 - \delta_1^2 \\ \int_0^{1-y_2} + \left[\frac{\delta_1^2}{1-\delta_1^2} \right] y_2 \int_0^{1-y_2} f(y_1, y_2) dy_1 = \frac{1}{1+\delta_1} \left\{ \cosh^{-1} \left(y_2^{-1/2} \right) \right. \\ \left. + \cosh^{-1} \left[\left(1 - \delta_1^2 \right)^{-1/2} \right] \right\}, & \text{if } y_2 \leq 1 - \delta_1^2. \end{cases} \quad (4-47)$$

The means are found to be $\bar{y}_1 = 1/6 \left[(1 + \delta_1^3)/(1 + \delta_1) \right]$, and $\bar{y}_2 = 1/2 - \bar{y}_1$, where the last relation follows from the identity $y_1 + y_2 = x_1$.

Now consider impacts on atom 2. Exactly the same reasoning leads to identically the same distributions if δ_1 is replaced by $\delta_2 = \cos \theta_K''$. (Note: $\theta_K'' < \pi/2$.) The distributions on the two atoms separately can be folded together with the empirical probabilities p_1 and p_2 to yield the total density

$$P \left(\frac{E_V}{E_{CM}} \right) = p_1 f_1 \left[\left(\frac{E_V}{E_{CM}} \right) / E_1, \delta_1 \right] / E_1 + p_2 f_1 \left[\left(\frac{E_V}{E_{CM}} \right) / E_2, \delta_2 \right] / E_2. \quad (4-48)$$

and similarly for E_R^V , replacing f_1 by f_2 . (Recall that $dy_1 = d(E_V^V/E_{CM})/E_1$.)

In Fig. 4-13, this approximate density is compared with the Monte Carlo results for one case and is observed to be within the statistical error. The approximate and sample means differ by less than 3%. (Note: A similar approximation can be constructed for the rigid rotor model, but would involve numerical integration for the densities.)

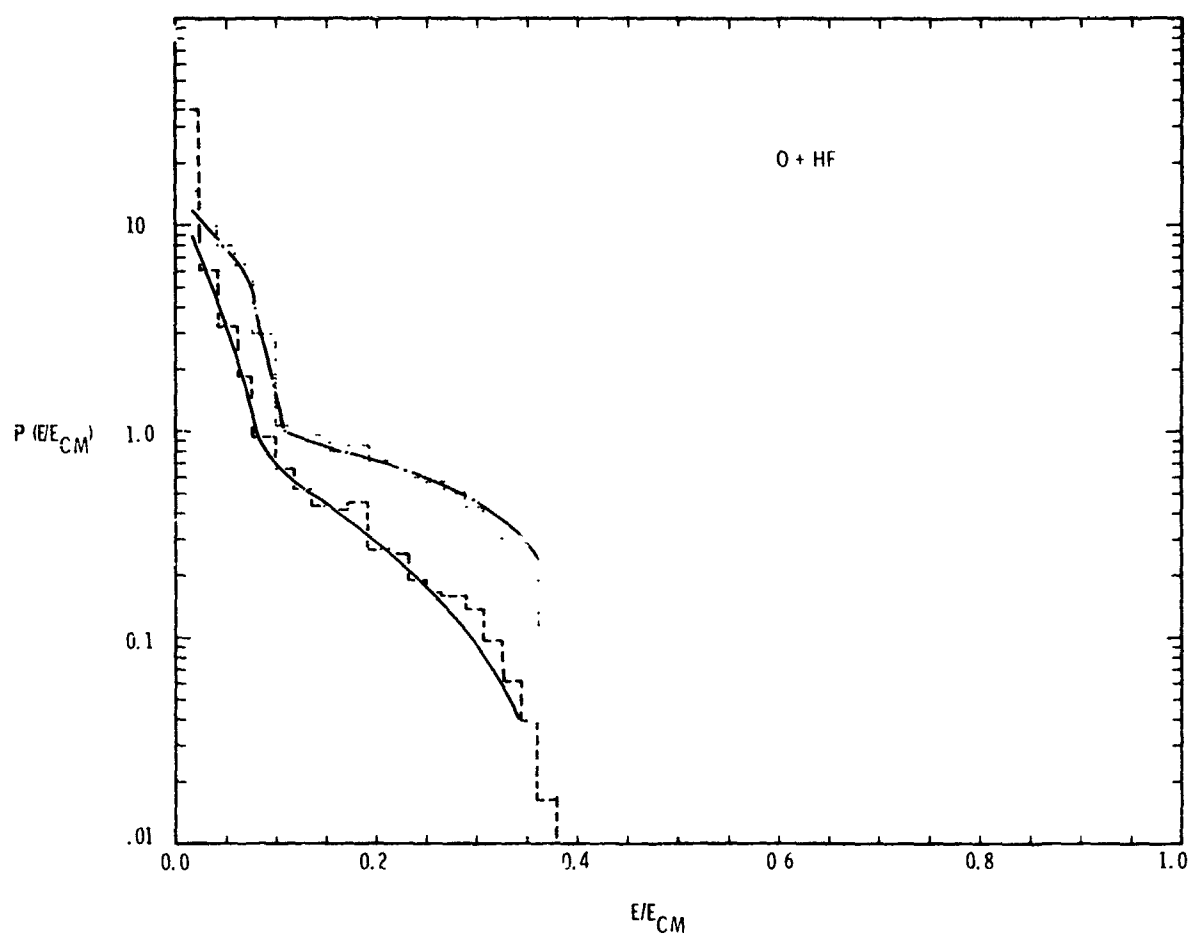


Figure 4.13 - Comparison between approximate and empirical distributions for O + HF within the vibrational model. Dashed histogram represents E_V^V/E_{CM} , and dotted histogram, E_R^V/E_{CM} , and smooth curves represent approximate solutions for these distributions.

4.7 Differential Energy Transfer Cross Sections

The probability distributions, $P(E/E_{CM})$, shown in Figs 4-2 through 4-11, can be converted to differential energy transfer cross sections describing the harmonic oscillator rotational or vibrational excitation or the rigid rotor rotational excitation as a function of incident center-of-mass kinetic energy by the relation,

$$\frac{\partial \sigma(E/E_{CM})}{\partial E} = \frac{\sigma_{hs} P(E/E_{CM})}{E_{CM}}, \quad (4-49)$$

where σ_{hs} is the geometric hard-sphere cross section for the appropriate atom-diatom pair, and $E = E_R^V$, E_V^V , or E_R^R , respectively.

Approximate hard-sphere cross sections for the system studied can be calculated by the following procedure: The average geometric cross sections for the hard-sphere diatomic models are listed in Table 4-I. These cross-sectional areas correspond to spherical areas of projection with radii equal to 0.99A, 0.94A, and 1.25A for OH, HF, and HCl, respectively. Normal hard-sphere collision cross sections (in units of \AA^2) for each atom-diatom pair can then be constructed from the relation

$$\sigma_{hs} = \pi d_{ab}^2, \quad (4-50)$$

where d_{ab} is equal to the effective spherical radius for the appropriate diatomic as listed above, plus the hard-sphere radius, R_q , of the appropriate atomic collision partner, as listed in Table 4-I.

4.8 Discussion

The average energy transfer results listed in Table 4-II, and the energy transfer probability distributions shown in Figs. 4-2 through 4-10 can be interpreted by noting that energy transfer in the classical, hard-sphere collision model used in this study depends only on the reduced mass of the atom-diatomic hydride system and on geometrical constraints that are, in turn, dependent on hard-sphere radii and bond distances. These geometrical constraints arise partly from the fact that some impact points on the diatomic molecule are inaccessible from certain directions due to shielding by the second molecular atom, while other impact points are completely inaccessible due to the finite size of the colliding atom. A discussion of the interplay between the reduced mass and geometric effects for atom-rigid rotor collisions was included in a previous publication.⁽²⁸⁾

For kinematic reasons, collisions with the hydrogen atom in the diatomic hydride are much more effective in transferring precollision center-of-mass kinetic energy into the diatom's internal modes. It is well known that for simple atom-diatomic models, collisions perpendicular to the diatomic bond activate only rotation, while collinear collisions activate only vibration. As can be seen from Eq. (4-35), for impacts on the hydrogen atom the model used in this work predicts that a specific fraction of the impulse imparted during a collision is transmitted to the internal modes. This impulse is transmitted into the vibrational mode for collinear collisions and into the rotational mode for perpendicular collisions, and is divided between the two modes at intermediate angles. Table 4-III shows this fraction of center-of-mass energy [from Eq. (4-36)], transmitted into internal modes for normal collisions on the diatomic hydrogen atom as a function of the atom-diatomic hydride collision pair. These entries, then, represent the maximum fraction of the center-of-mass energy which can go into either internal mode for each collision pair. These results can be contrasted with the fact that for each of the atom-rigid rotor pairs, impact points exist that allow transmittal of all the center-of-mass kinetic energy into the

Table 4-III. Maximum Normalized Energy Transfer to Internal Modes (E_R^V/E_{CM} or E_V^V/E_{CM}) in Atom-Harmonic Oscillator Collisions.

Diatomic Atom	He	O	Ar
OH	0.744	0.405	0.300
HF	0.730	0.379	0.271
HCl	0.691	0.311	0.195

diatomic rotational mode. This difference between the dynamics of the atom-rigid rotor and the atom-harmonic oscillator systems is mirrored in the extended tails of the $P(E_R^r/E_{CM})$ distributions shown in Figs. 4-2 through 4-9.

Some uncertainty exists in determining the proper way to interpret the results of classical calculations involving the collisional activation or deactivation of a quantized internal mode when the average classical collision exchanges less than a full quantum of energy with the mode in question. Thompson has discussed this point recently in regard to his Monte Carlo trajectory calculations of vibrational deactivation.^{(27(b))} Parker⁽³²⁾ has shown that a classical calculation of the collinear collisional excitation of a harmonic oscillator will yield the same average vibrational energy transfer as the quantum mechanical solution first proposed by Jackson and Mott⁽³³⁾ if the initial collisional kinetic energy is much greater than the energy of a vibrational quantum transition in the quantum treatment. For the diatomic hydrides considered in this work, the transition from the ground to the first vibrational state requires on the order of 0.4 to 0.5 eV. Thus, unless the average impulse transmitted along the diatomic bond axis becomes significantly larger than 0.4 eV, the vibrational energy distribution functions, $P(E_V^V/E_{CM})$, shown in Figs. 4-2 through 4-10, will be largely invalid. Since the great majority of any sample of collisions will be both grazing and off the collinear axis, the average initial center-of-mass

collisional energies must exceed the 1- to 10-eV range for which our calculation was originally intended before the vibrational distributions in Figs 4-2 through 4-10 apply. Table 4-II shows that the average classical vibrational excitation varies between 3.6% (He + OH) and 1.4% (Ar + HCl) of the initial center-of-mass collision energies. Thus, even in the most favorable case (He + OH), the initial center-of-mass energy must exceed 12 eV before one vibrational quantity will be excited on the average. Since, on the average, more of the collision energy goes into rotation and even the higher rotational levels are much more closely spaced than vibrational levels, a similar problem does not arise in calculating the rigid-rotor rotational excitation.⁽²⁸⁾

The purpose of this calculation was to assess the appropriateness of the rigid-rotor approximation in the calculation of rotational excitation probabilities in collisions with initial center-of-mass energies of a few eV. The results of the atom-harmonic oscillator calculations show that, classically, vibrational excitation does reduce the number of collisions that exhibit high degrees of rotational excitation. However, in the collision range between 1 and 10 eV, most of the classically calculated vibrational excitation is "forbidden," in the sense that it corresponds to less than a vibrational quantum. It remains for future work to determine, in detail, how seriously this nearly "closed" channel affects the rotational energy distribution for this energy range. In the meantime, it seems reasonable to expect the rigid-rotor rotational excitation probabilities, $P(E_R^R/E_{CM})$, rather than the harmonic oscillator collision probabilities, $P(E_R^V/E_{CM})$, to more closely mirror the actual situation in the energy range of 1 to 10 eV. At higher center-of-mass collision energies, the harmonic oscillator excitation probabilities, $P(E_R^V/E_{CM})$ and $P(E_V^V/E_{CM})$, should be closer to reality.

The calculations presented in this work represent only a "physical" or dynamic picture of inelastic excitation in atom-diatomic hydride collisions. They can be expected to be reasonably approximate for collisions between such closed-shell species as Ar and He with HCl and HF.

Although "chemical" effects have generally been disregarded in this study, two types of chemical effects can be expected to modify the picture presented above. The first is actual chemical reaction, which should be most important in the interaction of oxygen atoms with the hydroxyl radical. The reaction



is over 0.7 eV exothermic, while exchange of the hydrogen atom between oxygen atoms is, of course, thermoneutral. Reaction (4-51) has a bimolecular rate constant of $2.16 \times 10^{-11} \text{ cm}^3/\text{sec}$, apparently independent of temperature.⁽³⁴⁾ If this rate holds to the highly nonthermal velocities modeled in this calculation it would represent a reaction cross section (at a relative velocity of $6 \times 10^5 \text{ cm/sec}$) of 3.6 \AA^2 . The approximate hard-sphere cross section for the models of O and OH used above is 10.6 \AA^2 , so that an appreciable fraction of the collisions between O and OH may be expected to follow a chemically reactive channel, rather than the inelastic activation channel calculated above. A chemical reaction could also be important in the nearly thermoneutral hydrogen atom exchange between O and HCl.

The second type of "chemical" effect has been demonstrated in a number of shock tube studies where nonrare-gas atom collisions with diatomics have shown an anomalously large cross section for vibrational deactivation.⁽³⁵⁻³⁹⁾ This effect has been attributed to the increased "stickiness" of the collisions, as represented by the formation of some type of moderately long-lived collision complex that can effectively transfer energy out of the diatomic's vibrational mode. Nikitin and Umunski⁽⁴⁰⁾ have recently speculated that this stickiness is due to "vibronic" vibrational-to-translational transfer involving excited electronic states of the atom-diatomic complex. Because of the principle of microscopic reversibility, this effect could also be important in the translational-to-vibrational energy exchange modeled above for collisions involving O and OH.

collisional energies must exceed the 1- to 10-eV range for which our calculation was originally intended before the vibrational distributions in Figs 4-2 through 4-10 apply. Table 4-II shows that the average classical vibrational excitation varies between 3.6% (He + OH) and 1.4% (Ar + HCl) of the initial center-of-mass collision energies. Thus, even in the most favorable case (He + OH), the initial center-of-mass energy must exceed 12 eV before one vibrational quantity will be excited on the average. Since, on the average, more of the collision energy goes into rotation and even the higher rotational levels are much more closely spaced than vibrational levels, a similar problem does not arise in calculating the rigid-rotor rotational excitation. ⁽²⁸⁾

The purpose of this calculation was to assess the appropriateness of the rigid-rotor approximation in the calculation of rotational excitation probabilities in collisions with initial center-of-mass energies of a few eV. The results of the atom-harmonic oscillator calculations show that, classically, vibrational excitation does reduce the number of collisions that exhibit high degrees of rotational excitation. However, in the collision range between 1 and 10 eV, most of the classically calculated vibrational excitation is "forbidden," in the sense that it corresponds to less than a vibrational quantum. It remains for future work to determine, in detail, how seriously this nearly "closed" channel affects the rotational energy distribution for this energy range. In the meantime, it seems reasonable to expect the rigid-rotor rotational excitation probabilities, $P(E_R^r/E_{CM})$, rather than the harmonic oscillator collision probabilities, $P(E_R^v/E_{CM})$, to more closely mirror the actual situation in the energy range of 1 to 10 eV. At higher center-of-mass collision energies, the harmonic oscillator excitation probabilities, $P(E_R^v/E_{CM})$ and $P(E_V^v/E_{CM})$, should be closer to reality.

The calculations presented in this work represent only a "physical" or dynamic picture of inelastic excitation in atom-diatomic hydride collisions. They can be expected to be reasonably approximate for collisions between such closed-shell species as Ar and He with HCl and HF.

Although "chemical" effects have generally been disregarded in this study, two types of chemical effects can be expected to modify the picture presented above. The first is actual chemical reaction, which should be most important in the interaction of oxygen atoms with the hydroxyl radical. The reaction



is over 0.7 eV exothermic, while exchange of the hydrogen atom between oxygen atoms is, of course, thermoneutral. Reaction (4-51) has a bimolecular rate constant of $2.16 \times 10^{-11} \text{ cm}^3/\text{sec}$, apparently independent of temperature.⁽³⁴⁾ If this rate holds to the highly nonthermal velocities modeled in this calculation, it would represent a reaction cross section (at a relative velocity of $6 \times 10^5 \text{ cm/sec}$) of 3.6 \AA^2 . The approximate hard-sphere cross section for the models of O and OH used above is 10.6 \AA^2 , so that an appreciable fraction of the collisions between O and OH may be expected to follow a chemically reactive channel, rather than the inelastic activation channel calculated above. A chemical reaction could also be important in the nearly thermoneutral hydrogen atom exchange between O and HCl.

The second type of "chemical" effect has been demonstrated in a number of shock tube studies where nonrare-gas atom collisions with diatomics have shown an anomalously large cross section for vibrational deactivation.⁽³⁵⁻³⁹⁾ This effect has been attributed to the increased "stickiness" of the collisions, as represented by the formation of some type of moderately long-lived collision complex that can effectively transfer energy out of the diatomic's vibrational mode. Nikitin and Uman'ski⁽⁴⁰⁾ have recently speculated that this stickiness is due to "vibronic" vibrational-to-translational transfer involving excited electronic states of the atom-diatomic complex. Because of the principle of microscopic reversibility, this effect could also be important in the translational-to-vibrational energy exchange modeled above for collisions involving O and OH.

As noted in Section 3, the problem of multiple collisions has also been ignored in the present work. Multiple impacts are important for collinear or nearly collinear collisions, and can influence the vibrational excitation distribution. Since the focus of this work is on the rotational excitation distribution, which is unaffected by collinear collisions in the impulse approximation, it was felt that ignoring multiple impacts was a justifiable approximation. The classical calculation of collinear collisions between hard sphere atoms and diatomics, including the effects of multiple collisions, has been explored in detail by Benson et al.⁽⁴¹⁾

5. PURE ROTATIONAL EMISSION FROM DIATOMIC MOLECULES IN THE QUANTUM AND CLASSICAL LIMITS

5.1 Introduction

One of the most useful concepts in the construction of the quantum theory is the correspondence principle.⁽⁴²⁾ It can be stated in several ways, including the following way: "Quantum theory must approach classical theory asymptotically in the limit of large quantum numbers."⁽⁴³⁾ Thus, when dealing with manifestly macroscopic phenomena, classical physics is an appropriate description of nature. There is, therefore, a transition region where classical physics is a more-or-less good approximation to the more exact quantum description of whatever system is of interest, or put somewhat differently, classical physics is one approximation in the arsenal of all possible approximations to the complete, exact quantum theory. As such, the quantitative limits on the region of validity of the classical approximation for a system are clearly of interest, just as are the limits of validity of any approximation.

Furthermore, there are two reasons why the limits of validity and usefulness for the classical theory are especially interesting. First, a calculation that displays the explicit evolution from quantum to classical behavior as quantum numbers increase is a quantitative illustration of the correspondence principle. Second, classical calculations tend to be more tractable than the analogous quantum calculations, so that when the classical theory may be usefully applied, it is usually advantageous so to do.

The problem that is addressed here is that of pure rotational radiation emission from diatomic molecules with a permanent electric dipole moment. In particular, the emission into a broad frequency band, which includes the contributions of several individual transitions, is studied. This calculation is done

both purely quantum mechanically and purely classically; then the results of the two theories are quantitatively compared to demonstrate the onset of classical behavior as the relevant quantum numbers (and hence energies) increase.

To compare the classical and quantum theories of pure rotational emission, it is necessary to consider radiation in a broad wavelength band. If spectral information, line-by-line, were desired, a classical approximation would be of little use. Thus, the wavelength band must enclose a number of rotational lines for straightforward comparison between the two theories. The results of the calculation show that for large quantum numbers, a band containing as few as approximately five lines is sufficient for reasonably close agreement between the two theories.

Quantitatively, the results of this calculation apply only to simple rigid rotors whose energy levels are $(2\ell + 1)$ -fold degenerate, where ℓ is the principal rotational quantum number. Qualitatively, however, these results shed light, as well, on the classical limit for the asymmetric rotor with a permanent electric dipole moment. Since the levels of an asymmetric rotor are nondegenerate, and the energy levels are more closely spaced on the average than for the case of a simple rotor, it is clear that whenever the classical model of rotational emission is valid for the diatomic case, the classical model for radiative emission from an asymmetric rotor will certainly be valid for similar quantum numbers. ⁽⁴⁴⁾

5.2 Quantum Mechanical Formulation

The only nonzero Einstein coefficients for purely radiative decay for a rigid rotor with permanent electric dipole moment, μ , and moment of inertia I , are those in which the principal quantum number decreases by 1, and the second quantum number, m , changes by 0 or ± 1 . ⁽⁴⁵⁾

$$A_{\ell m \rightarrow \ell-1, m} = \kappa \frac{\ell^3 (\ell+m) (\ell-m)}{(2\ell+1) (2\ell-1)} \quad (5-1)$$

$$A_{\ell m \rightarrow \ell - 1, m-1} = \kappa \frac{1}{2} \frac{\ell^3 (\ell + m) (\ell + m - 1)}{(2\ell + 1) (2\ell - 1)} \quad (5-2)$$

$$A_{\ell m \rightarrow \ell - 1, m+1} = \kappa \frac{1}{2} \frac{\ell^3 (\ell - m) (\ell - m - 1)}{(2\ell + 1) (2\ell - 1)} \quad , \quad (5-3)$$

where

$$\kappa = (4\hbar^2 \mu^2 / 3c^3 I^3) \quad . \quad (5-4)$$

The Einstein coefficient for the transition from any m value in state ℓ to all m' values in state $\ell - 1$ is simply the sum of the above three expressions, and is independent of m . Thus,

$$A_{\ell} = \kappa \ell^4 / (2\ell + 1) \quad . \quad (5-5)$$

This means that the problem of radiative cascade from one rotational energy level to the next is independent of the quantum number, m .

In order to determine the power radiated by an ensemble of excited rigid rotors, the population of each excited rotor energy level must be found. If it is assumed that at $t = 0$ there is an ensemble of rotors all excited into the rotational state with principal rotational quantum number ℓ_0 , then the equation governing the average population of the ℓ_0 level is given by the following expression, in the absence of collisions:

$$\frac{dN_{\ell_0}}{dt} = -A_{\ell_0} N_{\ell_0}(t) \quad , \quad (5-6)$$

where $N_{\ell_0}(t)$ is the average population of the ℓ_0 level, regardless of the quantum number m . If the normalized boundary condition of $N_{\ell_0}(t=0) = 1$ is imposed, the solution of this simple equation is

$$N_{\ell_0}(t) = e^{-A_{\ell_0} t} \quad (5-7)$$

In general, the population of the $\ell_0 - n$ level obeys the following equation:

$$\frac{dN_{\ell_0 - n}}{dt} = -A_{\ell_0 - n} N_{\ell_0 - n} + A_{\ell_0 - n + 1} N_{\ell_0 - n + 1} \quad (5-8)$$

Because of the selection rule, $\ell' = \ell - 1$ for radiative decay, only the population of the level one step higher than the level of interest can contribute to the population. Thus, the only two nonzero terms on the right side of the above equation have been included.

The above set of equations, along with the ℓ_0 equation and the boundary condition at $t = 0$, is easily solved. For $\ell \neq \ell_0$, the general solution is

$$N_{\ell}(t) = \sum_{\ell'=\ell}^{\ell_0} e^{-A_{\ell'} t} \frac{(A_{\ell_0} A_{\ell_0-1} \dots A_{\ell'+1})}{\prod_{\substack{\ell''=\ell \\ \ell'' \neq \ell'}}^{\ell_0} (A_{\ell''} - A_{\ell'})} \quad (5-9)$$

The above equation gives the average population of the various rotational energy levels for an ensemble of rotors with the normalized boundary condition that $N_{\ell_0}(t=0) = 1$ and $N_{\ell \neq \ell_0}(t=0) = 0$.

The energy given up by a rigid rotor when it undergoes a radiative transition from state ℓ to state $\ell-1$ is

$$E_{\ell} - E_{\ell-1} = (\hbar^2/2I) [\ell(\ell+1) - (\ell-1)(\ell-1+1)] = (\hbar^2/I) \ell \quad (5-10)$$

The contribution to the average radiated power by the ℓ^{th} level P_{ℓ} is, therefore, given by

$$P_{\ell} = N_{\ell}(t) (E_{\ell} - E_{\ell-1}) A_{\ell} \quad (5-11)$$

To compute the total average emitted power, it is now only necessary to sum up the contribution from each individual transition. The average total power emitted by an ensemble of particles, all of which were in the state ℓ_0 at $t = 0$, is

$$P(\ell_0, t) = (\hbar^2/I) \left\{ \sum_{\ell=1}^{\ell_0-1} \ell A_{\ell} \sum_{\ell'=\ell}^{\ell} e^{-A_{\ell'} t} \left[\frac{A_{\ell_0} A_{\ell_0-1} \dots A_{\ell+1}}{\prod_{\substack{\ell''=\ell \\ \ell'' \neq \ell'}} (A_{\ell''} - A_{\ell'})} \right] + \ell_0 A_{\ell_0} e^{-A_{\ell_0} t} \right\} \quad (5-12)$$

The above expression is the total radiated power. If only the power emitted into some frequency band is of interest, the sum over ℓ must be modified to include only those transitions that contribute to the band. If the lower and upper limits for the angular frequency for the band are designated ω_1 and ω_2 , respectively, then,

$$\omega_1 \leq (E_{\ell} - E_{\ell-1})/\hbar \leq \omega_2 \quad (5-13)$$

This is an implicit relation for the maximum and minimum allowed ℓ 's in the first sum over ℓ in Eq. (5-12). The power in a given band will simply be denoted by $P(\ell_0, t; \omega_1, \omega_2)$.

Equation (5-12) gives the power radiated as a function of time. Therefore, to find the total energy radiated into the band, P must be integrated with respect to time from $t = 0$ to $t = \infty$. Thus,

$$EN(\ell_0; \omega_1, \omega_2) = \int_0^{\infty} dt P(\ell_0, t; \omega_1, \omega_2) \quad , \quad (5-14)$$

and

$$EN(\ell_0; \omega_1, \omega_2) = (\hbar^2/I) \left\{ \sum_{\ell=0}^{\ell_0-1} \left[\theta(\hbar \ell/I - \omega_1) \theta(\omega_2 - \hbar \ell/I) \right. \right. \\ \left. \sum_{\ell'=\ell_0}^{\ell} \left(\prod_{\substack{\ell''=\ell \\ \ell'' \neq \ell'}}^{\ell_0} \frac{A_{\ell''}}{(A_{\ell''} - A_{\ell'})} \right) \right] \\ \left. + \theta(\hbar \ell_0/I - \omega_1) \theta(\omega_2 - \hbar \ell_0/I) \ell_0 \right\} \quad , \quad (5-15)$$

$$\text{where } \theta(x) = \begin{cases} 0 & \text{for } x < 0 \\ 1 & \text{for } x > 0 \end{cases} \quad . \quad (5-16)$$

The two-step functions in Eq. (5-15) arise because of the band limits on the first ℓ sum (i.e., as a result of Eq. (5-13)).

Rewriting the sum of the products of the pair-wise differences of the A_{ℓ} 's in Eq. (5-15) in terms of a Vandermonde determinant,⁽⁴⁶⁾ then putting all the terms in the ℓ' sum over this common denominator, the total band energy, EN , simplifies considerably.

$$EN(\ell_0; \omega_1, \omega_2) = \sum_{\ell=0}^{\ell_0} (\hbar^2/I) \ell \theta(\hbar \ell/I - \omega_1) \theta(\omega_2 - \hbar \ell/I) . \quad (5-17)$$

This expression simply means that each level in the band pass contributes an energy of $(\hbar^2 \ell/I)$ to the total energy, which could have been written in the beginning. The integration of the power to get this simple expression for the energy is, therefore, a check on the validity of the power formula, Eq. (5-12).

Equations (5-12) and (5-17) are the quantum mechanical expressions for the power and energy emitted by a rigid rotor with a permanent electric dipole moment. The power emitted by such a rotor may also be calculated by using strictly classical physics. It is this classical version of the calculation to which attention is now directed.

5.3 Classical Formulation

A classical rigid rotor with a permanent electric dipole moment radiates as it rotates, since the two charges making up the dipole are being accelerated because of their circular motion. The dipole is radiating energy away, so that there is an effective torque acting on it, the radiative damping torque, $\underline{\Gamma}$ ^(44, 47)

$$\underline{\Gamma} = (2/3c^3) \underline{\mu} \times \ddot{\underline{\mu}} , \quad (5-18)$$

where $\underline{\mu}$ is the electric dipole moment, and the dots signify a time derivative.

For pure rotation

$$\ddot{\underline{\mu}} = \underline{\omega} \times \underline{\omega} \times \underline{\mu} , \quad (5-19)$$

where $\underline{\omega}$ is the rotor's angular velocity.

This classical model for radiative damping and emission now reduces to solving the equation of motion for $\underline{\omega}$, using the torque, $\underline{\Gamma}$. For a simple rigid rotor,

$$I \dot{\underline{\omega}} = \underline{\Gamma} \quad , \quad (5-20)$$

or

$$\dot{\omega} = (2\mu^2/3c^3I) \omega^3 \quad , \quad (5-21)$$

The solution of this equation is straightforward, and leads to the following expressions when using the initial condition that $\omega(t=0) = \omega_0$.

$$\omega = \omega_0 / (1 + \delta \omega_0^2 t)^{1/2} \quad , \quad (5-22)$$

where

$$\delta = 4\mu^2/3c^3I \quad . \quad (5-23)$$

In order to find the power radiated by this rotating dipole, it is necessary only to use these expressions for $\underline{\omega}$ in Larmor's power formula:⁽⁴⁷⁾

$$P = (2/3c^3) \left| \ddot{\underline{\mu}} \right|^2 \quad , \quad (5-24)$$

or, upon using Eq. (5-22),

$$P = (1\delta/2) \omega_0^4 / (1 + \delta \omega_0^2 t)^2 \quad . \quad (5-25)$$

This is the classical analog to Eq. (5-12) for the power emitted from a quantum mechanical rigid rotor with a permanent electric dipole moment.

The above equation is the total average power emitted by the rotating dipole. If one is interested in the power emitted into some frequency band from ω_2 to ω_1 with, for example, $\omega_2 > \omega_1$, then this expression must be modified to

include contributions between only the proper frequencies. Thus,

$$P(\omega_1, \omega_2) = \left[(I\delta/2) \omega_0^4 / (1 + 2\delta \omega_0^2 t) \right] \times \left[\theta(\omega_2 - \omega) \theta(\omega - \omega_1) \right] \quad (5-26)$$

The total energy radiated during a complete band pass, EN , by a classical rotor is simply the difference in energy of the rotor between the state when it is at the top of the band and the state when it is at the bottom of the band.

$$EN = \begin{cases} (1/2) I(\omega_2^2 - \omega_1^2) & \text{for } \omega_0 > \omega_2 \\ (1/2) I(\omega_0^2 - \omega_1^2) & \text{for } \omega_2 < \omega_0 < \omega_2 \\ 0 & \text{for } \omega_0 < \omega_1 \end{cases} \quad (5-27)$$

In the completely classical limit, the power described by Eqs. (5-12) and (5-26) should become identical. In fact, if a classical approximation is made in Eq. (5-8), the classical result in Eq. (5-22) may be obtained directly. For a state, l , Eq. (5-8) may be rewritten as

$$\frac{\partial N_l}{\partial t} = -\kappa \left(\frac{l^4}{2l+1} \right) N_l + \kappa \left(\frac{(l+1)^4}{(2(l+1)+1)} \right) N_{l+1} \quad (5-28)$$

having used the expression for the Einstein coefficient, Eq. (5-5). In order to approach the classical limit in the equation, l must become a continuous variable so that N becomes a function of the two variables t and l . Also, the difference between the l^{th} and the $(l+1)^{\text{th}}$ terms on the right side of Eq. (5-28) must become a partial derivative. Finally, by recognizing that

$$2l+1 \cong 2l, \quad (5-29)$$

in the classical limit, Eq. (5-28) becomes

$$\frac{1}{\kappa} \frac{\partial N(\ell, t)}{\partial t} = \frac{1}{2} \frac{\partial}{\partial \ell} \left[\ell^3 N(\ell, t) \right], \quad (5-30)$$

or

$$\frac{1}{\kappa} \frac{\partial N}{\partial t} - \frac{1}{2} \ell^3 \frac{\partial N}{\partial \ell} = \frac{3}{2} \ell^2 N. \quad (5-31)$$

The characteristic equations for this partial differential equation are

$$\frac{dt}{ds} = \frac{1}{\kappa} \quad (5-32)$$

$$\frac{d\ell}{ds} = -\frac{1}{2} \ell^3 \quad (5-33)$$

$$\frac{dN}{ds} = \frac{3}{2} \ell^2 N. \quad (5-34)$$

The solution of these equations is straightforward.

$$t = s/\kappa \quad (5-35)$$

and

$$\ell^2 = (s + \ell_0^{-2})^{-1} \quad (5-36)$$

Having used the boundary condition that when s is zero (and hence, when t is zero), ℓ is ℓ_0 . From Eq. (5-10), the relation between the frequency ω and the quantum number ℓ in the classical limit is clearly given by

$$\omega = \hbar \ell / I. \quad (5-37)$$

Thus, using Eq. (5-35) along with the definitions of κ and δ , Eq. (5-36) becomes

$$\omega^2 = \omega_0^2 / (1 + \delta \omega_0^2 t), \quad (5-38)$$

which is identical to the purely classical result, Eq. (5-22).

5.4 Results

In order to examine the onset of the classical limit for the rotational radiation from a diatomic molecule, the power as calculated from both quantum (Eq. (5-12)) and classical (Eq. (5-26)) theories has been computed for a variety of initial quantum levels and band passes. The curves for radiated power as a function of time are shown in Figs. 5-1 through 5-4. In each case the prediction of the quantum theory is represented by the solid line, and the prediction of the classical theory is represented by the dashed line. The classical curve has been drawn so that the area under the curve (i.e., the total energy emitted in a band pass) is the same as that for the quantum curve. This means that the energy of the rotating molecule as it decays into the band, classically, is the same as the highest quantum energy state included in the band; and for the decay out of the band, the classical energy is equal to the lowest quantum state included in the band.

The expressions for the radiated power are applicable to any diatomic molecule with a permanent electric dipole moment, but in order to be concrete, all the results have been plotted for the hydrogen fluoride molecule. The results will be qualitatively the same for other molecules, but since the moment of inertia and electric dipole moment will vary from case to case, the time scale for decay will be different for each case. It is a reasonably straightforward matter to apply the results to any other molecule of interest.

There are a number of interesting features shown in Figs. 5-1 through 5-4. First of all, as the relevant quantum numbers increase, the agreement between the quantum and classical theories improves, as one would expect on the basis of the correspondence principle. In fact, the results plotted in Fig. 5-3 for an

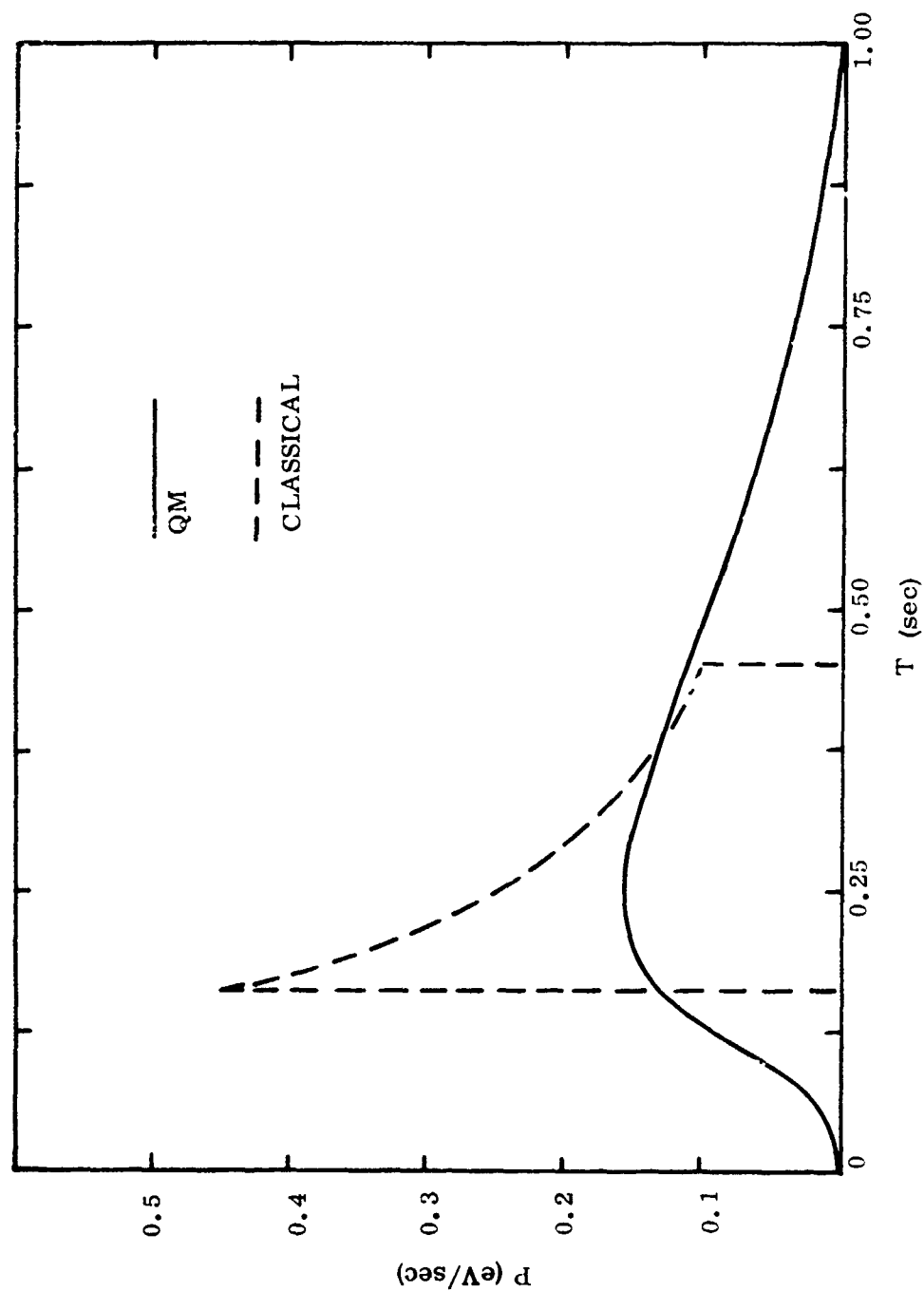


Figure 5.1 - Radiated power as a function of time for the molecule HF with initial rotational quantum number $J_0 = 10$, and for a band pass including contributions from the 6th through the 4th level.

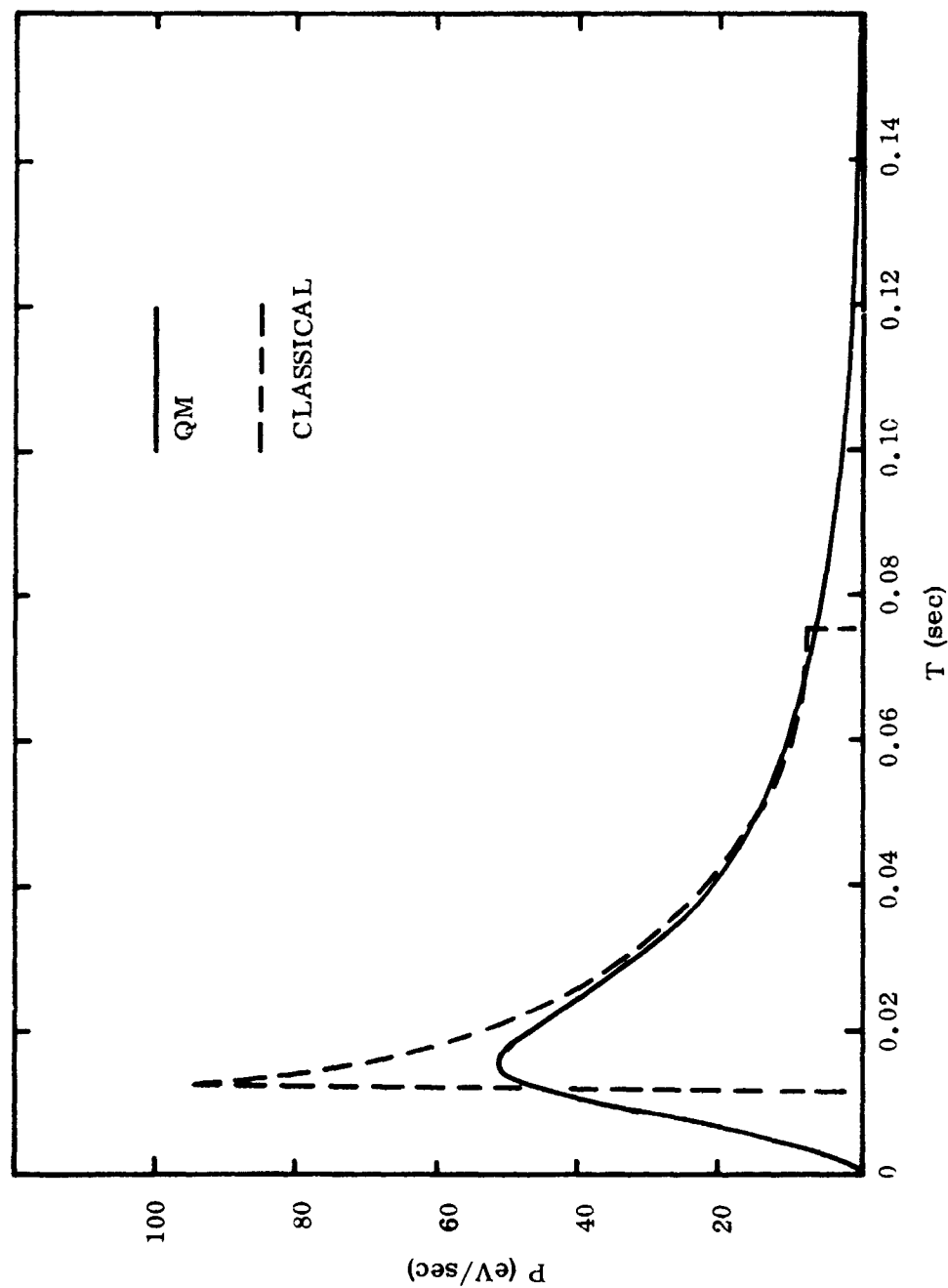


Figure 5.2 - Radiated power as a function of time for the molecule HF with initial rotational quantum number $j_0 = 15$, and for a band pass including contributions from the 10th through the 5th level.

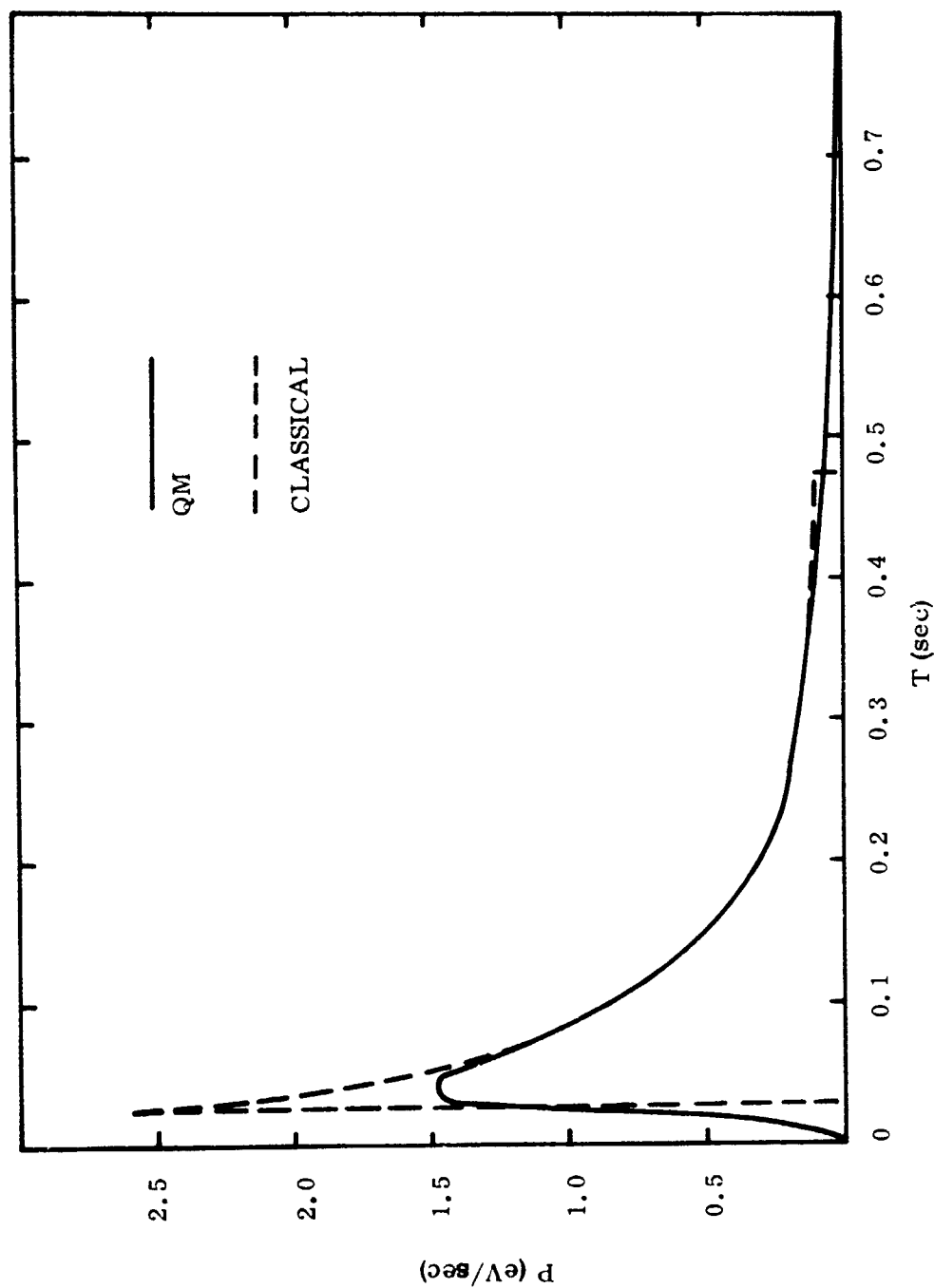


Figure 5.3 - Radiated power as a function of time for the molecule HF with initial rotational quantum number $j_0 = 30$, and for a band pass including contributions from the 25th through the 10th level.

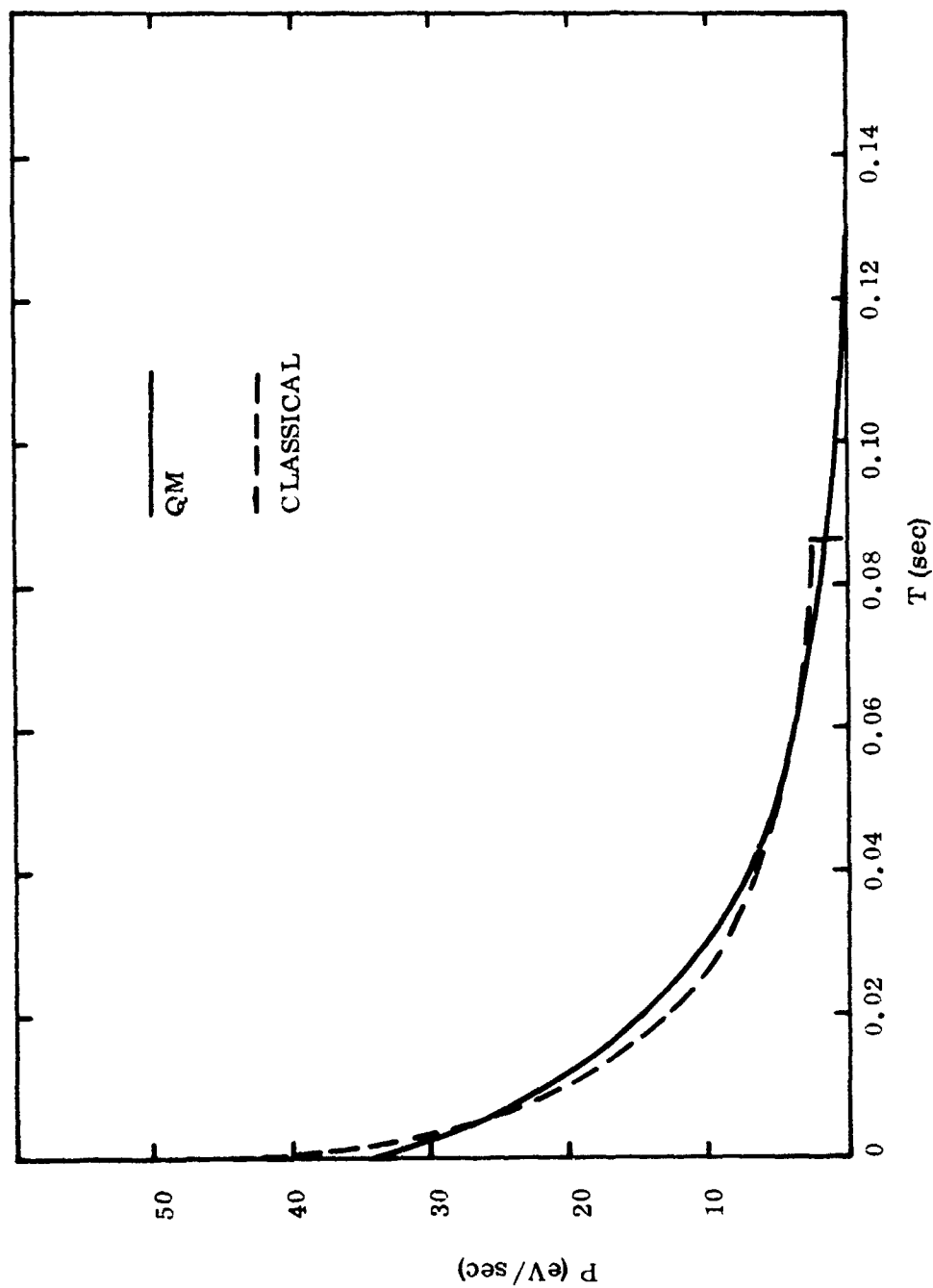


Figure 5.4 - Radiated power as a function of time for the molecule HF with initial rotational quantum number $j_0 = 20$, and for a band pass including contributions from the 20th through the 101 level.

initial rotational quantum number of 30, and a band enclosing contributions from the 25th through the 10th levels, show close agreement between the two theories for almost all times of interest.

In Figs. 5-1 through 5-3, the initial rotational state emits at a frequency too high to contribute to the band power, so that there is some nonzero time interval when there is little or no radiation. Classically, the onset of radiation is abrupt, but quantum mechanically, it is gradual, and, in fact, is nonzero before the beginning of the classical radiating region. This precursor is a manifestation of the fact that there is always a nonzero, albeit sometimes quite small, probability for a very rapid quantum transition.

At the onset of the classical radiation, the classically computed power is larger than the quantum mechanically computed power by roughly a factor of 1.5 or 2. This "overshoot" remains at higher quantum levels, but tends to become increasingly narrow, so that this initial classical peak becomes a spike of infinitesimal area.

Finally, just as the classical curve begins abruptly, it ends abruptly as the frequency decays to a value outside the band limits. The quantum curve decays continuously across this region, and the decay is asymptotically described by an exponential function with a lifetime equal to the lifetime of the lowest energy state that contributes to the band.

As Fig. 5-1 through 5-3 show, the main difference between the classical power and the quantum power for quantum numbers above approximately 10 occurs in the precursor and overshoot at the beginning of the classical radiating region. Figure 5-4 shows the case where the initial state is able to contribute to the band power, so that there is neither a precursor nor an overshoot. The agreement between the two curves is within a few percent everywhere in the classical radiating region.

A number of conclusions can be drawn from the foregoing discussion. For rotational quantum numbers greater than 15 to 20, and for bands sufficiently wide to include the contributions of 5 or more levels, the classical theory very closely reproduces the quantum mechanical prediction of the radiated power as a function of time. This is especially true in those cases in which the initial state can contribute to the power radiated into the band. Any distribution of initial radiating states (e.g., a thermal distribution) would remove the abrupt beginning and end of the classical radiating region. Hence, the sharp corners of the classical curve would be smoothed, bringing the predictions of the two theories into considerably closer agreement.

This work is for the case of a simple or diatomic rotor whose energy levels are $(2l + 1)$ -fold degenerate. For an asymmetric rotor whose levels are not degenerate, the classical theory would probably be adequate at even lower quantum numbers or energies, and for bands somewhat narrower than those considered for the diatomic rotor. The classical theory for an asymmetric rotor does not predict sharp cutoffs for the power;⁽³⁾ thus, there would be relatively few precursor or overshoot problems, as described above.

REFERENCES

- (1) H. Wolfhard, "(S) Report of ARPA/IDA Workshop on High Altitude Plumes (U)," IDA Paper P-794, August 1971.
- (2) T.J. Rieger (Ed.), "(S) High Altitude Rocket Plume Self-Interference. ABMDA HIT Program Technical Report (U)," Aerodyne Research, Inc., SR-1, January 1972.
- (3) "HIT-to-Kill Homer Ground Test (HIT PHASE II) Milestone Report, Preliminary Design Review, Vol. I, Technical," Vought Missile and Space Company Report, January 25, 1972.
- (4) H. R. Baum, et al., "(S) Water Vapor Rotational Band Radiation from High Altitude Rocket Plumes (U)," Aerodyne Research, Inc., RN-4, November 1971.
- (5) H. R. Baum, J. Fluid Mech., 58, Part 4, May 22, 1973, p. 795.
- (6) K. S. Tait, C. E. Kolb, and H. R. Baum, "Classical Calculations of Rotational and Vibrational Excitation in Energetic Atom-Diatomic Hydride Collisions," to be published in J. Chem. Phys., Sept. 1, 1973.
- (7) T. J. Rieger, "Pure Rotational Emission from Diatomic Molecules in the Quantum and Classical Limits," Aerodyne Research, Inc., RR-14, February 1973; to be published in J. Chem. Phys.
- (8) H. R. Baum, C. E. Kolb, T. J. Rieger, and E. A. Sutton, "(S) Water Vapor Rotational Band Radiation from High Altitude Rocket Plumes (U)," Aerodyne Research, Inc., RN-16, March 1972.
- (9) E. P. Muntz, B. B. Hamel, and B. L. Maguire, "Some Characteristics of Exhaust Plume Rarefaction," AIAA J. 8, 1651 (1970).
- (10) J. W. Brook and B. B. Hamel, "Spherical Source Flow with a Finite Back Pressure," Phys. Fluids, 15, 1898 (1972).
- (11) H. R. Baum, "The Interaction of a Transient Exhaust Plume with a Rarefied Atmosphere," J. Fluid Mech., 58, 795 (1973).
- (12) J. A. F. Hill and J. S. Draper, "Analytical Approximation for the Flow from a Nozzle into a Vacuum," J. Spacecraft and Rockets, 4, 1552 (1966).
- (13) E. P. Gross, and M. Krook, "Model for Collision Processes in Gases: Small Amplitude Oscillations of Charged Two-Component Systems," Phys. Rev., 102, 593 (1956).

References (continued)

- (14) R. E. Grundy, "Axially Symmetric Expansion of a Monatomic Gas from an Orifice into a Vacuum," Phys. Fluids, 12, 2011 (1969).
- (15) D. G. Anderson, "On the Steady Krook Kinetic Equation: Part 1," J. Fluid Mech., 26, 17 (1966).
- (16) D. G. Anderson and H. K. Macomber, Engineering Sciences Laboratory, Harvard University, Cambridge, Mass., Technical Report 10 (1964).
- (17) S. W. Benson and G. C. Berend, J. Chem. Phys. 44, 4247 (1966) and J. Chem. Phys. 47, 4199 (1967).
- (18) J. D. Kelley and M. Wolfsberg, J. Phys. Chem. 71, 2373 (1967); J. Chem. Phys. 50, 1894 (1969) and J. Chem. Phys. 53, 2967 (1970).
- (19) G. Bergeron and X. Chapuisat, Chem. Phys. Lett. 11, 334 (1971) and J. Chem. Phys. 57, 3436 (1972).
- (20) M. A. Wartell and R. J. Cross, Jr., J. Chem. Phys. 55, 4983 (1971).
- (21) J. R. Stallcop, Chem. Phys. Lett. 12, 30 (1971) and J. Chem. Phys. 56, 4505 (1972).
- (22) G. D. B. Sorenson, J. Chem. Phys. 57, 5421 (1972).
- (23) W. Eastes and D. Secrest, J. Chem. Phys. 56, 640 (1972).
- (24) M. D. Gordon and D. Secrest, J. Chem. Phys. 52, 120 (1970).
- (25) H. K. Shin, J. Phys. Chem. 76, 2006 (1972).
- (26) J. D. Doll and W. H. Miller, J. Chem. Phys. 57, 5019 (1972).
- (27) (a) D. L. Thompson, J. Chem. Phys. 56, 3470 (1972); (b) J. Chem. Phys. 57, 4164 (1972); and (c) J. Chem. Phys. 57, 4170 (1972).
- (28) C. E. Kolb, H. R. Baum, and K. S. Tait, J. Chem. Phys. 57, 3409 (1972).
- (29) G. Herzberg, Spectra of Diatomic Molecules, D. Van Nostrand, New York, 1950.
- (30) Yu. No. Belyaev, V. B. Leonas, and A. V. Semyagin, Abstracts of the Fifth International Conference on the Physics of Electronic and Atomic Collisions, Nauka, Leningrad, 1967, p. 643.
- (31) L. D. Landau and E. M. Lifshitz, Mechanics, Addison-Wesley, Reading, Mass., 1960, p. 63.

ferences (continued)

- (32) J. G. Parker, Phys. Fluids, 2, 449 (1959).
- (33) J. M. Jackson and N. F. Mott, Proc. Roy. Soc. (London), A137, 703 (1932).
- (34) D. L. Baulch, D. D. Drysdale, and A. C. Lloyd, High Temperature Reaction Rate Data, 3, 14 (1969).
- (35) C. W. von Rosenberg, Jr. and K. L. Wray, J. Chem. Phys. 54, 1406 (1971).
- (36) J. F. Bott and N. Cohen, J. Chem. Phys. 55, 5124 (1971).
- (37) J. F. Kiefer and W. R. Lutz, 11th Symp. Combust., Pittsburgh, Pa. (1967) p. 67.
- (38) W. P. Breshears and D. F. Bird, J. Chem. Phys. 48, 4768 (1968).
- (39) J. F. Bott and N. Cohen, J. Chem. Phys. 58, 934 (1973).
- (40) E. E. Nikitin and S. Ya. Umanski, Comm. on At. and Mol. Phys., 3, 195 (1972).
- (41) S. W. Benson, G. C. Berend, and J. C. Wu, J. Chem. Phys. 38, 25 (1963).
- (42) N. Bohr, Z. Physik 13, 117 (1923).
- (43) A. Messiah, Quantum Mechanics, North-Holland, Amsterdam, 1966, Vol. I, p. 29.
- (44) H. R. Baum and T. J. Rieger, Phys. Rev. A, 7, No. 2, Feb. 1973, p. 536
- (45) See, for example, L. Pauling and E. Wilson, Introduction to Quantum Mechanics, McGraw-Hill, New York, 1935, Chap. XI.
- (46) See, for example, F. Nering, Linear Algebra and Matrix Theory, Wiley, New York, 1964, p. 80.
- (47) L. Landau and E. Lifschitz, Classical Theory of Fields, Pergamon, New York, 1960.

Unclassified

Security Classification

DOCUMENT CONTROL DATA - R & D

(Security classification of title, body of abstract and indexing annotation must be entered when the overall report is classified)

1. ORIGINATING ACTIVITY (Corporate author) AERODYNE RESEARCH, INC. 20 South Avenue Burlington, Massachusetts 01803		2a. REPORT SECURITY CLASSIFICATION Unclassified	
		2b. GROUP	
3. REPORT TITLE ROCKET PLUME RADIATION DUE TO INTERACTIONS WITH THE ATMOSPHERE VOLUME 1: FAR FIELD PLUME RADIANCE MODEL			
4. DESCRIPTIVE NOTES (Type of report and inclusive dates) ABMDA Plume Interference Program - Final Technical Report			
5. AUTHOR(S) (First name, middle initial, last name) Thomas J. Rieger, Howard R. Baum, Charles E. Kolb, Kevin S. Tait, and Apostolos E. Germeles			
6. REPORT DATE July 1973		7a. TOTAL NO. OF PAGES 123	7b. NO. OF REFS 47
8a. CONTRACT OR GRANT NO. DAHC60-69-0035 Subcontract No. S-72-14		9a. ORIGINATOR'S REPORT NUMBER(S) ARI-RN-20 Vol. 1	
b. PROJECT NO.			
c.		9b. OTHER REPORT NO(S) (Any other numbers that may be assigned this report)	
d.			
10. DISTRIBUTION STATEMENT			
11. SUPPLEMENTARY NOTES		12. SPONSORING MILITARY ACTIVITY Advanced Ballistic Missile Defense Agency	
13. ABSTRACT <p>Calculations are presented that are elements of a model to predict the IR radiation emitted by high-altitude rocket plumes, because of the interaction of the plume gases with the ambient atmosphere. A model of plume radiance is presented, appropriate to high altitudes where the average time between plume and atmospheric species collisions is greater than the radiative lifetimes of the relevant excited molecular states. The three parts of the calculations - flow field density, molecular collisional excitation, and molecular nonequilibrium radiation - are identified and discussed.</p>			

Unclassified

Security Classification

14 KEY WORDS	LINK A		LINK B		LINK C	
	ROLE	WT	ROLE	WT	ROLE	WT
Plume Radiance Rotational Excitation Rotational Radiation Rarefied Flow						

Unclassified